UNIVERSITY OF ŽILINA

TRANSCOM PROCEEDINGS 2015

**11-th EUROPEAN CONFERENCE
OF YOUNG RESEARCHERS AND SCIENTISTS**

under the auspices of

Tatiana Čorejová
Rector of the University of Žilina

SECTION 4

**ELECTRIC POWER SYSTEMS
ELECTRICAL AND ELECTRONIC ENGINEERING**

ŽILINA June 22 - 24, 2015
SLOVAK REPUBLIC

TRANSCOM 2015
11th European conference of young researchers and scientists

TRANSCOM 2015, the 11th international conference of young European scientists, postgraduate students and their tutors, aims to establish and expand international contacts and co-operation. The main purpose of the conference is to provide young scientists with an encouraging and stimulating environment in which they present results of their research to the scientific community. TRANSCOM has been organised regularly every other year since 1995. Between 160 and 400 young researchers and scientists participate regularly in the event. The conference is organised for postgraduate students and young scientists up to the age of 35 and their tutors. Young workers are expected to present the results they had achieved.

The conference is organised by the University of Žilina. It is the university with about 13 000 graduate and postgraduate students. The university offers Bachelor, Master and PhD programmes in the fields of transport, telecommunications, forensic engineering, management operations, information systems, in mechanical, civil, electrical, special engineering and in social sciences incl. natural sciences.

SECTIONS AND SCIENTIFIC COMMITTEE

1. TRANSPORT AND COMMUNICATIONS TECHNOLOGY.

Scientific committee: Adamko Norbert (SK), Bugaj Martin (SK), Buzna Ľuboš (SK), Drozdziel Paweł (PL), Jánošíková Ľudmila (SK), Madleňák Radovan (SK), Rievaj Vladimír (SK), Teichmann Dušan (CZ)

2. ECONOMICS AND MANAGEMENT.

Scientific committee: Blašková Martina (SK), Hittmár Štefan (SK), Borkowski Stanisław (PL), Gregor Milan (SK), Kucharčíková Alžbeta (SK), Matuszek Józef (PL), Mičieta Branislav (SK), Rostášová Mária (SK), Sroka Włodzimierz (PL), Tomová Anna (SK), Zhivitskaya Helena (BLR)

3. INFORMATION AND COMMUNICATION TECHNOLOGIES.

Scientific committee: Dado Milan (SK), Hudec Róbert (SK), Kharchenko Vyacheslav (UKR), Klimo Martin (SK), Kršák Emil (SK), Matiaško Karol (SK), Pancerz Krzysztof (PL), Spalek Juraj (SK), Švadlenka Libor (CZ), Vaculík Juraj (SK), Vašinek Vladimír (CZ), Vrček Neven (HR)

4. ELECTRIC POWER SYSTEMS. ELECTRICAL AND ELECTRONIC ENGINEERING.

Scientific committee: Altus Juraj (SK), Brandštetter Pavel (CZ), Bury Peter (SK), Cacciato Mario (I), Čápová Klára (SK), Dobrucký Branislav (SK), Chernoyarov Oleg Vyacheslavovich (RU), Janoušek Ladislav (SK), Luft Mirosław (PL), Szychta Elżbieta (PL), Špánik Pavol (SK), Vittek Ján (SK)

5. **MATERIAL ENGINEERING. MECHANICAL ENGINEERING TECHNOLOGIES.**
   Scientific committee: Adamczak Stanisław (PL), Guagliano Mario (I), Konečná Radomila (SK), Kunz Ludvík (CZ), Kuric Ivan (SK), Meško Jozef (SK), Neslušan Miroslav (SK), Takács János (H), Ungureanu Nicolae Stelian (RO)

6. **MACHINES AND EQUIPMENT. TRANSPORT MEANS. APPLIED MECHANICS.**
   Scientific committee: Gerlici Juraj (SK), Chudzikiewicz Andrzej (PL), Malcho Milan (SK), Medvecký Štefan (SK), Zapoměl Jaroslav (CZ), Žmindák Milan (SK)

7. **CIVIL ENGINEERING.**
   Scientific committee: Bujňák Ján (SK), Ižvolt Libor (SK), Segalini Andrea (I)

8. **NATURAL SCIENCES (APPLIED MATHEMATICS). SOCIAL SCIENCES.**
   Scientific committee: Dopita Miroslav (CZ), Dzhalladova Irrada (UKR), Grecmanová Helena (SK), Katuščák Dušan (SK), Marčoková Mariana (SK), Růžičková Miroslava (SK), Šindelářová Jaromíra (CZ)

9. **SECURITY ENGINEERING. FORENSIC ENGINEERING.**
   Scientific committee: Kasanický Gustáv (SK), Kohút Pavol (SK), Navrátil Leoš (CZ), Řehák David (CZ), Sventeková Eva (SK), Šimák Ladislav (SK), Zagorecki Adam (UK), Zamiar Zenon (PL)

ORGANIZING COMMITTEE

CHAIRPERSONS	Čelko Ján, Bokůvka Otakar
EXECUTIVE SECRETARY	Vráblová Helena

MEMBERS   Bašťovanský Ronald, Belan Juraj, Bendík Ján, Brída Peter, Brůna Marek, Bulej Vladimír, Cíba Jakub, Čičmancová Silvia, Dulina Ľuboslav, Ďurovec Martin, Florková Zuzana, Gašová Zuzana, Grajcaríková Petra, Grejták Marek, Herda Miloš, Hőger Marek, Hrbček Jozef, Hruboš Marián, Hudák Martin, Koman Gabriel, Kutaj Milan, Kuzmová Mária, Kvet Michal, Magdolen Marián, Malichová Eva, Maňurová Mária, Masárová Gabriela, Metruk Rastislav, Murgašová Veronika, Nosek Radovan, Odrobiňák Jaroslav, Olešnaníková Veronika, Oriešková Veronika, Palkechová Marcela, Porubiaková Andrea, Pšenáková Zuzana, Račko Ján, Rusinková Jana, Rypáková Martina, Semanová Štefánia, Stankovičová Zuzana, Šarafín Peter, Šimková Ivana, Šušlik Ľuboš, Vaško Alan, Vincúrová Gabriela.

SECTION 4 ELECTRIC POWER SYSTEMS
ELECTRICAL AND ELECTRONIC ENGINEERING

REVIEWERS:

Babušiak Branko
Barabáš Ján
Borik Štefan
Braciník Peter
Čápová Klára
Faktorová Dagmar
Fedotov Evgeny
Gutten Miroslav
Höger Marek
Jamnický Igor
Janoušek Ladislav
Kúdelčík Jozef
Makarovič Juraj
Otčenášová Alena
Radil Roman
Rafajdus Pavol
Roch Marek
Smetana Milan
Špánik Pavol
Šušlik Ľuboš

Note:

Author/s are responsible for language contents of their papers

CONTENTS

Ultra-weak photon emission from amino-acid tyrosine

[*]Martin Bereta, [**]Michal Cifra, [**]Kateřina Červinková, [*]Ladislav Janoušek, [***]Ján Barabáš
[*]University of Žilina, Faculty of Electrical Engineering, Department of Electromagnetic and Biomedical Engineering, Univerzitná 1, 01026 Žilina, Slovakia, martin.bereta@fel.uniza.sk
[**]Institute of Photonics and Electronics, The Czech Academy of Sciences, Chaberská 57, 182 00 Prague, Czech Republic
[***]University Science Park of the University of Žilina, Univerzitná 1, 01026 Žilina, Slovakia

Abstract. This paper deals with ultra-weak photon emission from aqueous tyrosine solution. The principle of this kind of light emission is presented and the proposed mechanism of its origin during oxidation of tyrosine is described. The experimental part of the work is focused on the measurements of intensity of ultra-weak photon emission from different solutions of tyrosine. The results confirm the assumption, that the highest intensity is detected from the solution of tyrosine, hydrogen peroxide and ferrous sulphate heptahydrate, likely due the Fenton reaction originated hydroxyl radical, which causes oxidation of tyrosine, formation of high-energy intermediates and electron excited species.

Keywords: ultra-weak photon emission, reactive oxygen species, tyrosine, hydroxyl radical

1. Introduction

The emission of light, originated from chemical processes in organisms is an externally detectable manifestation of the metabolic activity of living cells. One of the most commonly used term for this kind of light emission is ultra-weak photon emission (UPE). Due to its non-invasive, low-operation-cost and label-free application, it can be used in many fields of biomedicine, such as dermatology, neuroscience or oncology [1].

Ultra-weak photon emission originates during relaxation of electronically excited species, which are generated chemically by oxidative reactions of reactive oxygen species (ROS) with bio-molecules. The formation of ROS is caused by physical, chemical and biological stimuli [2]. ROS can be distinguished in two main groups – radical ROS and non-radical ROS. Molecules of radical ROS have one or more unpaired electrons, and therefore they are highly reactive. Non-radical ROS have no unpaired electron, but they still exhibit rather high reactivity. ROS oxidize bio-molecules and these reactions can further lead to the formation of unstable intermediate chemical species which decay to form electronically excited species. The transition of these species to the ground state is related to the photon emission in near UVA (350 - 400 nm), visible (400 – 750 nm) and near IR (750 – 1300 nm) regions of the electromagnetic spectrum [1].

ROS have an important role in biochemical reactions in living cells. They have a great significance in intracellular signaling [3] and intercellular communication [4]. On the other hand, there is also an extensive evidence for harmful effects of excessive ROS levels in organisms [5]. It is known that reactions of radical species can be affected by magnetic field. There are many scientific works dealing with magnetic field effects on free radical reactions and radical pair mechanism [6 - 11]. Besides these works, numerous experimental works have shown that magnetic field can affect metabolic processes of cells [12-14]. Therefore it could be beneficial to find a connection between the mechanism of magnetic field effects on radical reactions and the evaluation of its influence on cell metabolism by the UPE detection.

UPE can be considered as a product of biochemical processes in living organisms, which involves oxidation of bio-molecules [15].The subject matter of this paper is focused on ultra-weak photon emission derived from oxidation of amino-acid tyrosine mediated by hydroxyl radical.

Tyrosine is aromatic nonessential amino-acid formed in organism from phenylalanine. Tyrosine is a building block for several important neurotransmitters, such as epinephrine or dopamine. It also underlies production of melanin, the pigment responsible for hair and skin color [16]. In this paper, it is shown, that chemically produced hydroxyl radical is responsible for oxidation of tyrosine, and there are presented experimental results of detection of ultra-weak photon emission from tyrosine aqueous solution.

2. Mechanism of ultra-weak photon emission from tyrosine

It is known that the oxidation of amino-acids and proteins is also associated with ultra-weak photon emission [17, 18]. Tyrosine is one of the most oxidatively sensitive residues (*i.e.* it has a low reduction potential) in proteins and its oxidation can be monitored by detection of ultra-weak photon emission. Oxidation of tyrosine mediated by hydroxyl radical involves a one-electron oxidation to form the tyrosyl radicals. It is known that hydroxyl radical originates from hydrogen peroxide by Fenton reaction:

$$Fe^{2+} + H_2O_2 \rightarrow Fe^{3+} + OH^{\bullet} + OH^{-} \qquad (1)$$
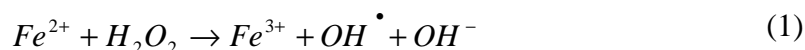
The interaction of hydroxyl radical with tyrosine initiates oxidative reactions. It is proposed, that these reactions lead to the formation of unstable intermediate tetroxide (ROOOOR) or dioxetane (ROOR). Tetroxide could be formed by recombination of two tyrosyl radicals and addition of molecular oxygen. Dioxetane could be a product of recombination of two tyrosyl radicals, without addition of molecular oxygen. The decomposition of tetroxide would be then followed by the formation of excited triplet carbonyl or singlet oxygen and ground state carbonyl. The transition of the excited triplet carbonyl to the ground state is accompanied by ultra-weak photon emission. Besides this, energy of the excited carbonyl can be transferred to the molecular oxygen and it leads to the formation of singlet oxygen that subsequently can also emit a photon. The reaction pathway of the dioxetane decomposition is identical besides the possibility of the direct singlet oxygen formation [2]. The principal proposed mechanism of the origin of UPE during tyrosine oxidation by hydroxyl radical is shown in the Figure 1.
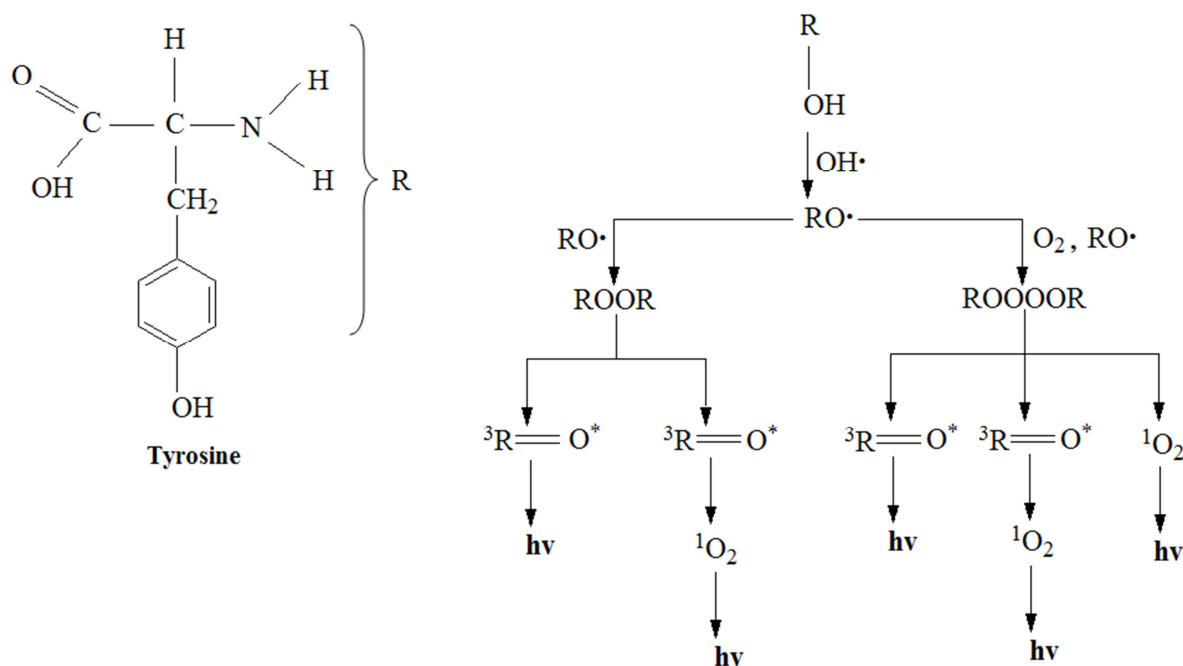
Fig. 1 Proposed mechanism of the origin of photon emission from tyrosine involves radical reactions, formation of intermediates and electron excited species

3. Materials and methods

The experimental part of the paper is focused on the detection of ultra-weak photon emission from different solutions of amino-acid tyrosine. In the experiments these compounds are used: tyrosine (P-Lab, CZ, purity 99 %), 30 % hydrogen peroxide (Penta, CZ, p.a.), ferrous sulphate heptahydrate (Penta, CZ, purity 99 %). Three different solutions of tyrosine are prepared. The first solution is composed of tyrosine with molecular concentration 0.38 mM. The second solution contains tyrosine (0.38 mM) and hydrogen peroxide (166.7 mM). The third solution consists of tyrosine (0.38 mM) with presence of hydrogen peroxide (166.7 mM) and ferrous sulphate heptahydrate ($FeSO_4.7H_2O$), where the concentration of iron is 0.27 mM. All the mentioned concentrations of individual components represent their final concentrations in the measured solution. Purified water is used as a control sample.

Photomultiplier tube H7360b, selected type (Hamamatsu Photonics K. K.) with a spectral sensitivity in the range 300 - 650 nm is used to detect photon emission. Typical dark count (noise) of the photomultiplier (PMT) is 15 counts per second. Measurement of the samples takes place in a light-tight chamber (standard black box, Institute of Photonics and Electronics, CZ) specially designed for the purposes of UPE measurements. The photomultiplier is mounted on the top of the chamber viewing a sample inside the chamber. Measurement equipment can be seen in the Figure 2.
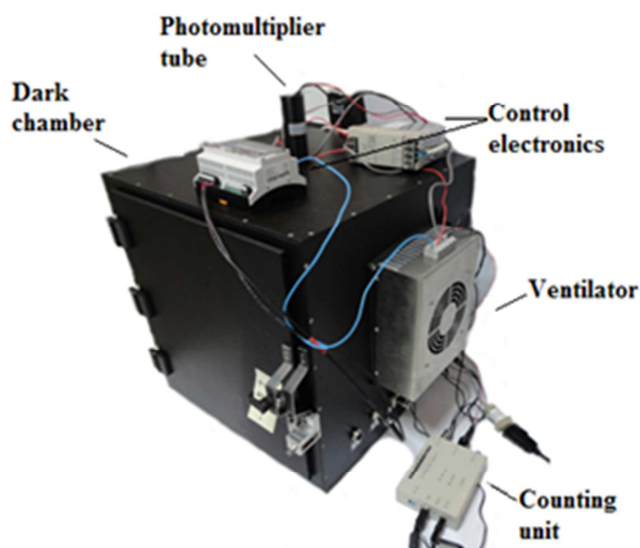
Fig. 2   Measurement equipment is based on the dark

The room temperature is about 21°C in all the measurements. The duration of every measurement is one hour. The volume of measured samples is 9 ml in all cases. Every experiment is performed in triplicate.

4. Results and discussion

The results of ultra-weak photon emission measurement are presented in the following figures. Figure 3 shows results of the intensity of ultra-weak photon emission from water, solution of tyrosine and solution of tyrosine with presence of hydrogen peroxide. The results represent the mean intensity of UPE, calculated from mean values of three repetitions of every experiment. The error bars constitute the standard deviation of the mean values. It can be seen, that the intensity of UPE is very similar for both solutions water and tyrosine and not distinguishable from the PMT dark count. No detectable photon emission arises in these cases. In the case of the solution of tyrosine and hydrogen peroxide (H_2O_2), an increase of the UPE intensity can be seen. Although

hydroxyl radicals are not formed in the solution, some molecules of tyrosine are probably oxidized by molecular oxygen or by products of the autooxidation of hydrogen peroxide. Electronically excited species are then formed from oxidation products of these reactions.
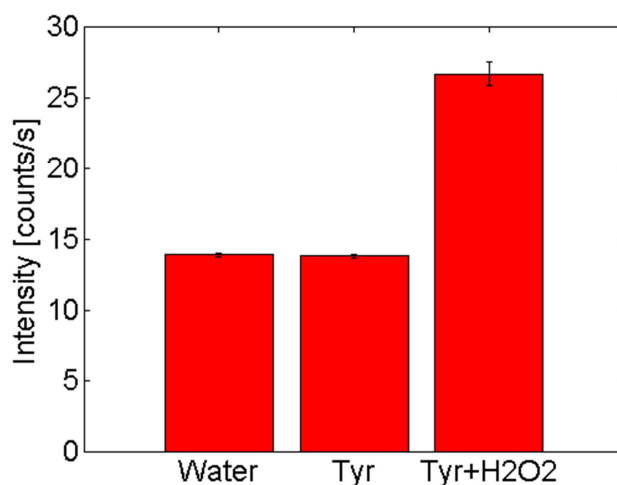
Fig. 3 Ultra-weak photon emission from different solutions of tyrosine and purified water

After the addition of ferrous sulphate to the solution of tyrosine and hydrogen peroxide and following Fenton reaction, the notable increase of photon emission is detected. The results of UPE for three repetitions of the experiment are shown in the Figure 4. The first peak in the UPE kinetics is likely caused by a fast oxidation of tyrosine molecules by hydroxyl radical. Total final shape of UPE intensity is likely due to the multiple reaction pathways as described in Figure 1.
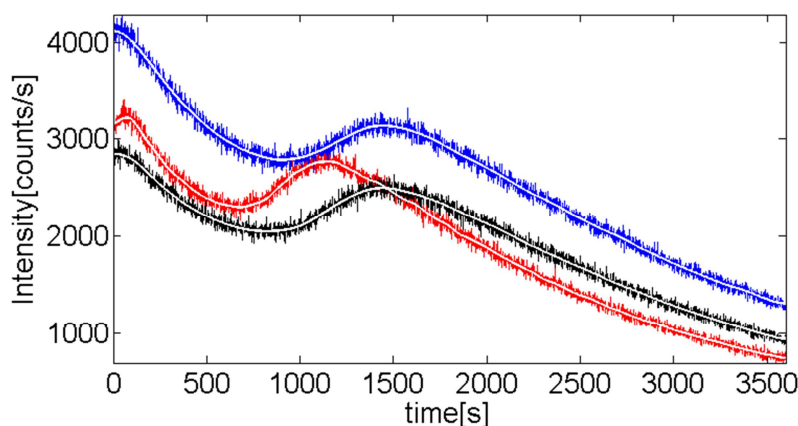
Fig. 4 Ultra-weak photon emission solution of tyrosine, hydrogen peroxide and ferrous sulphate manifests high

intensity compared to control samples.

5. Conclusion

The detection of ultra-weak photon emission from different solutions of tyrosine was presented in this paper. The results confirmed the assumption, that the highest intensity of UPE is detected from solution of tyrosine with the presence of hydrogen peroxide and ferrous sulphate, likely due to the hydroxyl radical mediated oxidation of tyrosine. The kinetics of UPE intensity from tyrosine without presence of hydrogen peroxide and from purified water was not distinguishable from dark count (noise) of photomultiplier. As it was noted above, UPE can be detected also from living cells and can be likely affected by magnetic field. Alternatively differences in kinetics of UPE from cells exposed to magnetic field and from unexposed cells could indicate the changes in biochemical

reactions during cell metabolism. Our next research will be focused on evaluation of magnetic field effects on cells using UPE detection.

Acknowledgement

References

[1] CIFRA, M., POSPÍŠIL, P. *Ultra-weak photon emission from biological samples: Definition, mechanisms, properties, detection and applications.* Journal of Photochemistry and Photobiology B: Biology. Vol. 139, pp. 2 – 10, 2014.

[2] POSPÍŠIL, P., et al. *Role of reactive oxygen species in ultra-weak photon emission in biological systems.* Journal of Photochemistry and Photobiology B: Biology. Vol. 139, pp. 11 – 23, 2014.

[3] LANDER, H. M., *An essential role for free radicals and derived species in signal transduction.* The FASEB Journal. Vol. 11, No. 2, pp. 118 – 124, 1997.

[4] THANNICKAL, V. J., FANBURG, B. L., *Reactive oxygen species in cell signaling.* American Journal of Physiology. Vol. 279, No. 6, pp. 1005-1028, 2000.

[5] WARIS, G, ASHAN, H. *Reactive oxygen species: Role in the development of cancer and various chronic conditions.* Journal of Carcinogenesis, Vol. 5, No. 14, 2006.

[6] ENGSTRÖM, S. *Magnetic field effects on free radical reactions in biology.* Bioengineering and biophysical aspects of electromagnetic fields, 3rd Ed., CRC Press, Boca Raton, Fla, USA, 2007. ISBN: 978-0-8493-9539-0

[7] BARNES, F. S., GREENEBAUM, B. *The effects of weak magnetic fields on radical pairs.* Bioelectromagnetics. Vol. 36, pp. 45 – 54, 2015.

[8] WOODWARD, J.R. *Radical pairs in solution.* Progress in reaction Kinetics and Mechanism. Vol. 27, pp. 165 – 207, 2002.

[9] TIMMEL, C. R., TILL, U., et al. *Effects of weak magnetic fields on free radical recombination reactions.* Molecular Physics. Vol. 95, No. 1, pp. 71 – 89, 1998.

[10] OKANO, H. *Effects of static magnetic fields in biology: role of free radicals.* Frontiers in Bioscience. Vol. 13, pp. 6106 - 6125, 2008.

[11] STEINER, U. E., ULRICH, T. *Magnetic field effects in chemical kinetics and related phenomena.* Chemical Reviews. Vol. 89, pp. 51 – 147, 1989.

[12] BARABÁŠ, J., RADIL, R. *Evidence of S. cerevisiae proliferation rate via exogenous low frequency electromagnetic field.* Information Technologies in Biomedicine. Vol. 7339, pp. 295 – 303, 2012.

[13] AKAN, Z., et al. *Extremely low-frequency electromagnetic fields affect the immune response of monocyte-derived macrophages to pathogens.* Bioelectromagnetics. Vol. 31, pp.603-612, 2010.

[14] AKDAG, M.Z., et al. *Alteration of nitric oxide production in rats exposed to a prolonged, extremely low-frequency magnetic field.* Electromagnetic Biology and Medicine. Vol. 26, pp. 99-106, 2007.

[15] KHABIRI, F., et al. *Non-invasive monitoring of oxidative skin stress by ultraweak photon emission (UPE)-measurement. I: mechanisms of UPE of biological materials.* Skin Research and Technology. Vol. 14, pp. 103-111, 2008.

[16] Tyrosine. [online][cit. 2015-03-10] <http://umm.edu/health/medical/altmed/supplement/tyrosine>

[17] BARNARD, M. L., GURDIAN. S., DIEP, D., LADD, M., TURRENS, J.F., *Protein and amino acid oxidation is associated with increased chemiluminescence.* Archives of Biochemistry and Biophysics. Vol. 300, No. 2, pp. 651 – 656, 1993.

[18] FEDOROVA, G. F., TROFIMOV, A. V., et al. *Peroxy-radical-mediated chemiluminescence: mechanistic diversity and fundamentals for antioxidant assay.* Arkivoc, pp. 163 – 215, 2007.

Stimulation Pulse Detection of Pacemaker

*Ivana Gálová, *Mariana Beňová, *Michal Gála

*University of Žilina, Faculty of Electrical Engineering, Department of Electromagnetic and Biomedical Engineering, Univerzitná 1, 01026 Žilina, Slovakia, {ivana.galova, mariana.benova, michal.gala}@fel.uniza.sk

Abstract. Pacemaker therapy has irreplaceable position in therapy of many cardiac diseases. The lifetime of implantable devices is several years and functionality depends on the battery condition. The verification of pacemaker parameters is possible using portable pacemaker programmers manufactured for specific pacemakers. Main parameters of pacemaker obtain frequency, pulse width, amplitude, sensitivity, etc. This article deals with possibilities and methods of pacemaker stimulation pulse detection, especially pulse width and frequency calculations from ECG signal. All measurements are in accordance with norm EN 45502-2-1:2003. Future plans include the construction of a small and embedded device for verifying functionality of pacemaker.

Keywords: pacemaker, stimulation pulse, signal generator, detection.

1. Introduction

Pacemakers play an important role in the treatment of cardiac diseases. This is especially true in cases where medication is no longer sufficient and patients require a pacemaker while waiting for a heart transplant. The other group of patients includes less severe heart-related problems which can be satisfactorily solved by implanted pacemakers and thus preserving patient vital functions. The lifetime of such devices is several years. Guaranteed operation is currently limited by the battery life of the device. When the battery capacity decreases, the device must be replaced. This end, manufacturer-specific portable pacemaker programmers must be used to verify battery properties (stimulation pulse width and frequency). These are however expensive and usually available only to cardiologists or internal physicians performing invasive cardiology. An alternative approach is to evaluate the state of the pacemaker battery by analyzing the patient electrocardiogram (ECG) recording. This article discusses the possibilities and means to verify the battery status of implantable stimulation devices and it proposes future plans for the construction of a small and embedded device, enabling general physicians and patients to obtain on-demand information about the battery status of the pacemaker [1][2][3][4].

2. Lifetime of pacemaker battery

According to standard EN 45502-2-1:2003, active implantable medical devices must include means to warn in advance of low battery state. The warning interval (during normal use of the device) must be comparable to regular patient checks at the ambulance. The conditions of replacement are model and manufacturer specific.

Fig. 1 shows the device lifetime phases, which are defined based on the residual battery capacity of implantable medical devices.
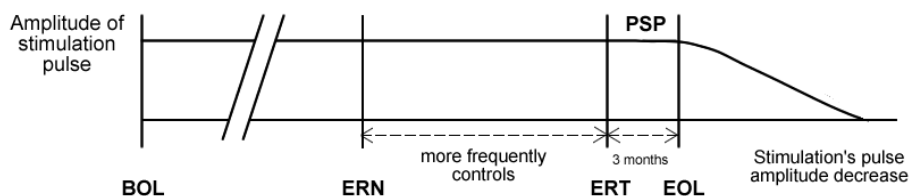
Fig. 1. Lifetime of the pacemaker power source.

Lifetime phases:
- Beginning of life (BOL) - implantable device is first approved by the manufacturer and certified for marketing,
- Elective replacement time (ERT) - the power supply reaches a pre-determined threshold capacity of the manufacturer, in which case the device replacement is recommended. This indicates the beginning stages of prolonged service period,
- Prolonged service period (PSP) - time period for the recommended replacement, during which the device continues to operate as specified by the manufacturer,
- End of life (EOL) - expiration of the extended service life, which is the end of the original manufacturer's specified functionality of the device, power saving mode until complete failure.

More frequent patient monitoring is recommended after crossing the elective replacement near (ERN) threshold. The mentioned norm does not define dependence of the device lifetime phases on frequency or on magnitude, but most of the manufacturers especially indicate the dependence on frequency (see Tab.1). The frequency is measured in asynchronous mode which is activated by permanent magnet with induction of more than 1 mT [1][9].

Manufacturer	BOL [1/min]	ERT [1/min]
Biotronik	90	80
Boston Scientific	100	85
ELA	96	80
Medtronic	85	65
MEDICO	100	70
St. Jude Medical	98.6	86.3
Vitatron	100	86

Tab. 1. The pacing pulse frequencies in asynchronous mode for BOL and ERT stages.

Permanent magnets with induction in range from 40 mT to 90 mT made by Selos company are used for measurements.

2.1. Battery level

Fig. 2 shows that the battery status of a single chamber pacemaker is determined by measuring the frequency and pacing pulse width in asynchronous mode. In general the pacing pulse width can be from 0.05 ms to 2 ms (minimal sampling frequency is 40 kHz by Nyquist–Shannon sampling theorem) [1].
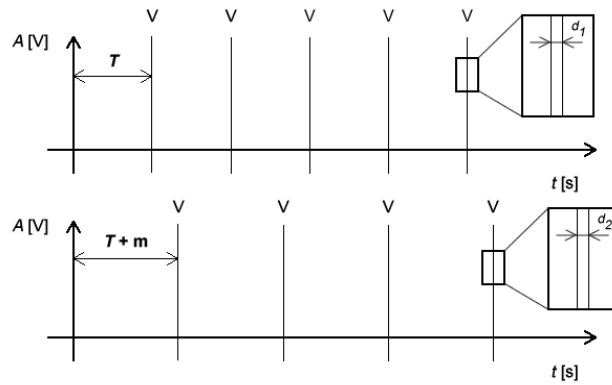
Fig. 2. The frequency of single chamber pacemaker stimulation in asynchronous mode: a) the proper function, b) low battery condition (f = 1/T, f – frequency, T – period, d – pulse width).
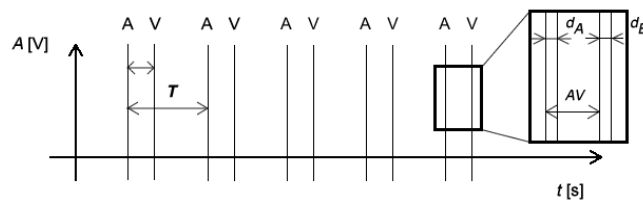
Fig. 3. The stimulation frequency in asynchronous mode during correct functioning of a dual chamber pacemaker.

Fig. 3 shows that dual chamber pacemakers can also determine the distance between the AV impulses that stimulate the atria and ventricles [1].

3. Stimulation Pulse Detection

To evaluate the pacemaker battery, a permanent magnet must be first used to switch the pacemaker into asynchronous mode and then recorded the ECG signal. To capture the signal, the MP36 unit manufactured by Biopac is used. Sampling frequency of 50 kHz and A/D sampling resolution of 24-bit are used. The MP36 unit connects to the patient simulator FLUKE ProSim 2.

Using the simulator, asynchronous mode of single chamber as well as of dual chamber pacemaker is tested. The pacemaker in the mentioned mode generates periodic pacing pulses regardless of the actual heart electrical activity. The recorded signal enables us to obtain information about the frequency and pulse width of the stimulus, or the duration of AV delay in dual chamber pacemaker. Based on the measured parameters, it is possible to evaluate the condition of the battery. Stimulation frequency decreases in time and the pacing pulse widens. The proposed algorithm is designed only for these conditions (frequency, pulse width and AV delay) and it does not give a solution for the dependence of the device lifetime phases on magnitude.

The design and implementation of the algorithm was carried out in MATLAB. The algorithm development was divided into several steps, each addressing possible drawbacks so as to achieve the desired accuracy and speed of the proposed algorithm. By comparing the distance between successive samples and known pacing pulse width (information obtained from the simulator), pacing pulses were detected and the required parameters were calculated.

However, detection was not accurate because the signal contained undesired artifacts. To eliminate these artifacts, different filter types were applied (differential filter, averaging filter, band-stop filter) [5][8].
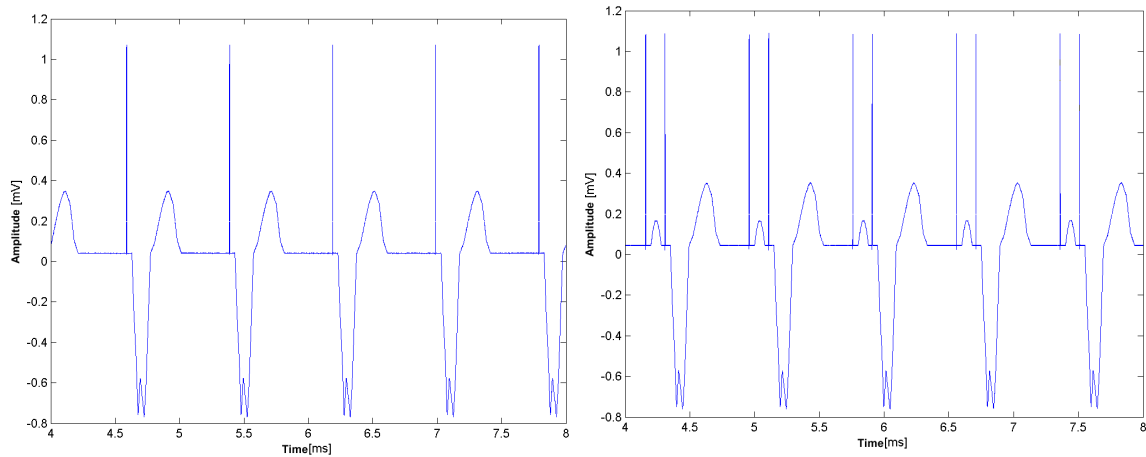
Fig. 4. The simulated ECG signal of a patient with a single chamber pacemaker (left figure) and a dual chamber pacemaker (right figure) in asynchronous mode.

However, after their application, the processed signal lost the information necessary to determine the pulse width (after applying the differential filter) and the evaluation time significantly increased (due to the averaging filter). In the end, simple mathematical operations were used, as one of the main criteria to design a fast and simple algorithm to enable use thereof in a microcontroller.

Each recorded sample was amplified by its square in order to "smooth out" the recording (amplify the stimulation pulses). Boundaries for pacing pulse detection were first determined intuitively (empirically). At later stages the algorithm has then been modified so as to determine these boundaries based on individual recordings. Subsequent analysis of samples exceeding the threshold value enabled the evaluation of the pulse width, frequency and, in case of dual chamber pacemaker, the duration of the AV delay.
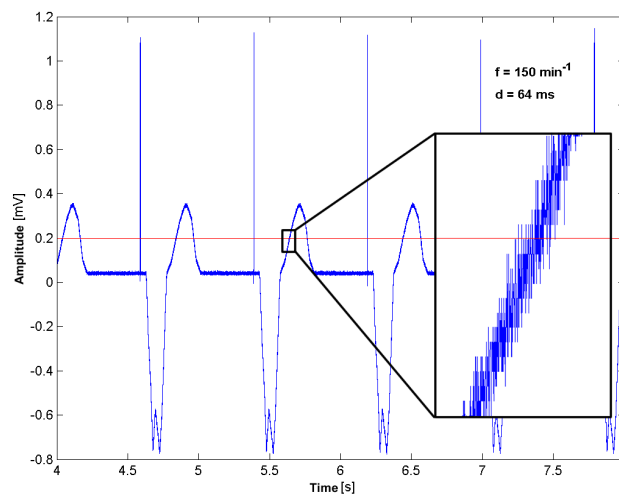
Fig. 5. Noisy simulated ECG of a patient with a single chamber pacemaker in asynchronous mode and detail of noisy signal at the boundary (f - frequency of 75 min^{-1}, d - 2 ms pulse width).

Fig. 5 shows that the search for local maxima was performed in order to confirm the correct identification of stimulation pulses and to discard possible noise-related artifacts [6][7].

3.1. Algorithm testing

The proposed algorithm has been tested on several simulated signals. Individual signals were degraded by different types of artifacts (AC 50 or 60 Hz noise and various breathing motion artifacts). The following section details the individual signals along with the detection and

indication of stimulation pulses. Fig. 6 shows a sample signal heavily degraded by noise from muscle activity.
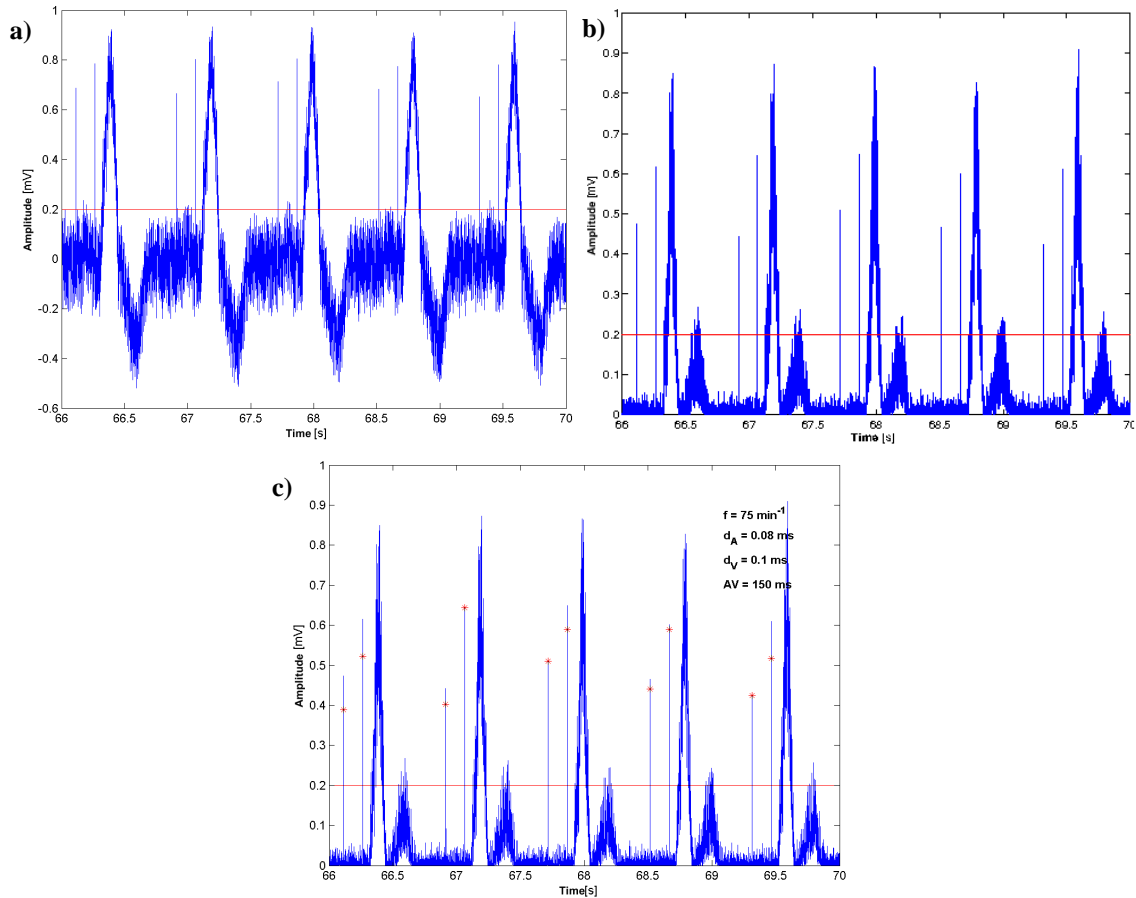
Fig. 6. Signal containing noise from muscle activity: a) the raw signal, b) signal after amplification, c) detection of stimulus pulses (red points).

The developed algorithm was tested with multiple one hour long recordings and the reliability of pacing pulse detection was above 98%. Real-life patient recordings obtained from the Faculty hospital in Žilina were also tested. The recording was measured from the first "standard" bipolar limb lead. The patient pacemakers were manufactured by Medtronic.
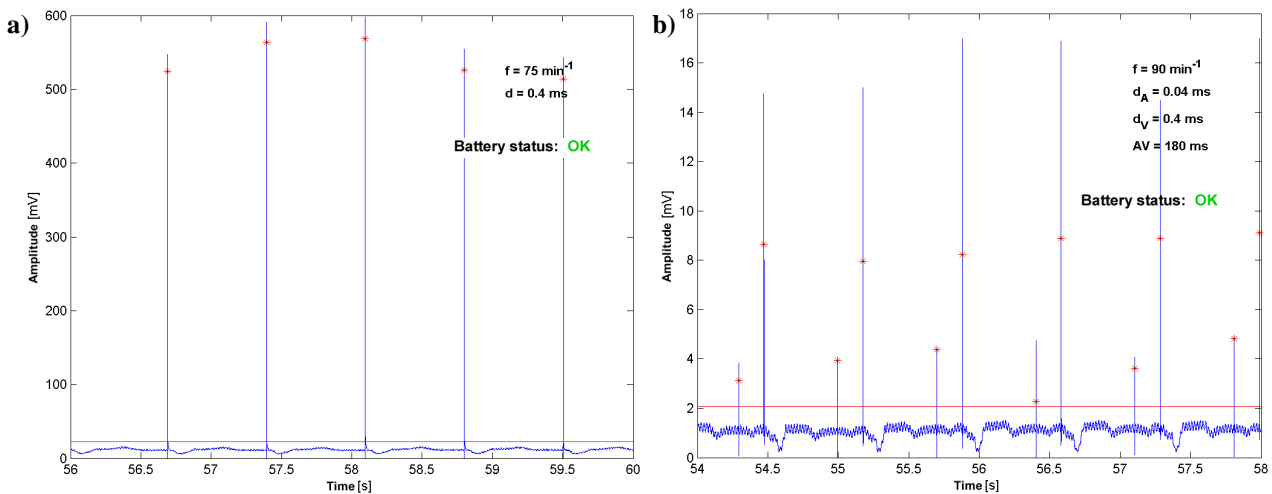
Fig. 7. Data analysis of patient with: a) single chamber pacemaker, b) dual chamber pacemaker.

The algorithm efficiency was once again confirmed and the results were discussed with a cardiologist (Dr. Ján Lehotský) and compared with those obtained from portable pacemaker programmers manufactured by Medtronic. Fig. 7 shows the final evaluations of battery status obtained from real patient data. Fig. 7a represents the single chamber pacemaker and Fig. 7b the dual chamber pacemaker.

4. Conclusion

The algorithm has been tested on real life data from patients with implanted pacemakers (Faculty Hospital Žilina) as well as on simulated recordings containing different types of artifacts (50 Hz, 60 Hz, breathing activity, muscular activity and random noise) and the success rate was above 98%. Current development is focused on hardware design of a small and portable ECG logger for verifying functionality of pacemaker.

The mentioned algorithm is designed only for detection of frequency, pulse width and AV delay and it does not solve the dependence of the device lifetime phases on magnitude.

Acknowledgement

References

[1] D. Korpas, Pacemaker technology, Praha: Mladá fronta, 2011, ISBN 978-80-204-2492-1.

[2] Z. Labza, D. Korpas, and M. Penhaker, "Determination of the Electric Parameters of Dual-Chamber Cardiostimulator," Proc. 9th IFAC Workshop on Programmable Devices and Embedded Systems (PDES 2009), Roznov pod Radhostem, Czech Republic, Feb. 2009, pp. 290-293, ISBN 978-3-902661-41-8, ISSN 1474-6670, doi:10.3182/20090210-3-CZ-4002.xxxx.

[3] J. J. Bax, T. Abraham, S. S. Barold, O. A. Breithardt, J. W. Fung, S. Garrigue, J. Gorcsan, D. L. Hayes, D. A. Kass, J. Knuuti, C. Leclercq, C. Linde, D. B. Mark, M. J. Monaghan, P. Nihoyannopoulos, M. J. Schalij, C. Stellbrink, and C. M. Yu, "Cardiac resynchronization therapy: Part 1--issues before device implantation," J Am Coll Cardiol, Dec. 2005.

[4] D. Korpas, "Psychological Intolerance to Implantable Cardioverter Defibrillator," Biomedical Papers-Olomouc, vol. 152, no. 1, June 2008, pp. 147-149, ISSN 1213-8118.

[5] M. Penhaker, T. Stula, and M. Augustynek, "Long-term heart rate variability assessment" The 5th Kuala Lumpur International Conference on Biomedical Engineering (BIOMED 2011), Held in Conjunction with the 8th Asian Pacific Conference on Medical and Biological Engineering, (APCMBE 2011), Springer-Verlag Berlin Heidelberg, 20 - 23 June 2011, pp. 532-535, ISSN 16800737, ISBN 978-364221728-9, doi:10.1007/978-3-642-21729-6_134.

[6] B. Babusiak and M. Gala, "Detection of Abnormalities in ECG" Information Technologies in Biomedicine (ITIB 2012), Springer-Verlag Berlin Heidelberg, 2012, pp. 161-171, ISBN 978-3-642-31195-6, ISSN 0302-9743.

[7] Š. Borik and I. Čáp, "Investigation of Pulse Wave Velocity in Arteries" The 35th International Conference on Telecommunications and Signal Processing (TSP 2012), Brno: University of Technology, 2012, pp. 562-565, ISBN 978-1-4673-1116-8.

[8] M. Penhaker, R. Hajovsky, and D. Korpas, "Measurement and Analysis EMC Parameters of Implantable Pacemaker," Przegląd Elektrotechniczny (Electrical Review), vol. 87, no. 5, 2011, pp. 265-268, ISSN 0033-2097.

[9] EN 45502-2-1:2003, Active implantable medical devices. Particular requirements for active implantable medical devices intended to treat bradyarrhythmia (cardiac pacemakers).

Effect of Eddy Current Probe Bank Angle on the Response Signal

Vladimir Chudacik, Milan Smetana

University of Zilina, Faculty of Electrical Engineering, Department of Electromagnetic and Biomedical Engineering, Univerzitna 1, 010 26 Zilina, Slovak Republic, vladimir.chudacik@fel.uniza.sk

Abstract. In this article, the effect of bank angle of testing probe on response signal is examined by using eddy current method on inductive solid plate. The given problem is solved using a simulation program OPERA 3D and creating a database with the values of a response signals obtained from simulated scans. The electromagnetic field induced by plate with the local inhomogeneities is examined at several geometric angles of eddy current probe with respect to conductive plate to obtain adequate and accurate data needed for evaluation and localization of inhomogeneities.

Keywords: Eddy current testing, simulations, bank angle, response signals, electromagnetic field.

1. Introduction

Demands on the quality and flawless materials used in various industry sectors, services and research brings the requirements for the development of methods that allow their adequate control. The eddy current testing (ECT) belongs to the electromagnetic non-destructive testing (NDT) and evaluation (NDE) methods. The main purpose of NDT is the detection of various material inhomogeneities, without mechanical damage of a tested object. Non-destructive evaluation extends this purpose. The maintenance in industry requires not only detection but also characterization of a detected defect. In NDE it is ambition to classify and quantify defects that can be detected in various structures. Several industrial applications require complex inspection where the main aim is to prevent a failure of the components, devices and equipment. Non-Destructive methods offer this possibility of periodic and thorough inspection of industry products, which ensures their safe, effective and long-term operation. ECT method can be applied to conductive materials. The advantages include high sensitivity, rapid scanning and contactless inspection [1],[2].

The basic principle of eddy current method is the phenomenon of electromagnetic induction. Electromagnetic (EM) field coil is supplied with time-varying electric current. The coil creates in its surrounding induced EM field. If the conductive material is located close enough to the coil, it comes to the induction of eddy currents. The induced eddy currents in the material flowing in a closed loops in a direction perpendicular to the primary EM field. The induced eddy currents subsequently generate secondary EM field that counteracts the cause of its formation and interacts with the primary EM field, shown in Fig. 1. Any change in the electromagnetic parameters of conductive material (presence of inhomogeneity) causes a change in the flow of eddy currents, which affects the resulting EM field. Result of this change in the electromagnetic field is changed coil impedance, which is measurable [3], [4].

The eddy current method is very sensitive to several factors, which can affect the response signal by measurement [5]. One of them is the stable position if the coil during material testing. This article is focused on the possibilities of using changes of the bank angle of the testing probe to achieve the additional information value. In the first step verifies if and how the changes in the angle and position influence response signals and in the next step verifies the usability of acquired response information.
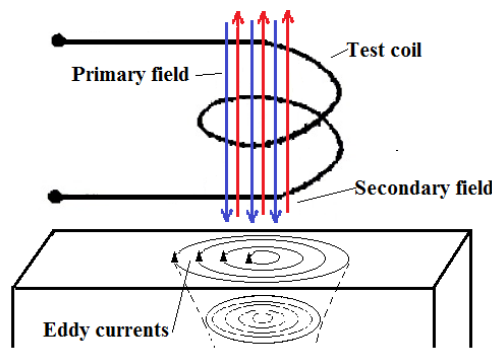
Fig. 1 Principle of the ECT method

2. Simulation model parameters

The simulation model is investigated by numerical way. For numerical analyses of electromagnetic fields is used software OPERA 3D, based on the finite element method.

Response signal by using the ECT method depends on several parameters. The basic factors include the type of coil and its properties, the distance between the coil and the investigated material or conductivity and geometric properties of material and present inhomogeneities. Very important is the selected frequency of the supply current. The frequency affects the depth of penetration and capability of the identification of inhomogeneities.

In simulations is used circular standard self-inductance probe defined as circular coil, shown in Fig. 2. In the first configuration, the probe is positioned parallel to the plate surface with 1mm lift-off and bank angle $\varphi = 0°$. In the next four configurations the bank angle $\varphi_1 = 45°$ and $\varphi_2 = -45°$ once in x-axis and once in y-axis with respect to the parallel plate with minimal 1mm lift-off, shown in Fig. 3. The coil is driven by the harmonic current with a frequency of $f = 10$ kHz and current density $\mathbf{J} = 2$ A/mm^2.
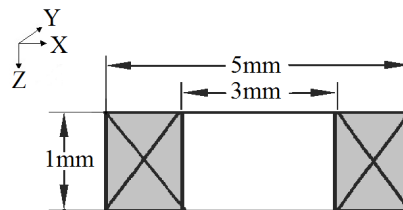
Fig. 2 Geometric parameters of ECT probe
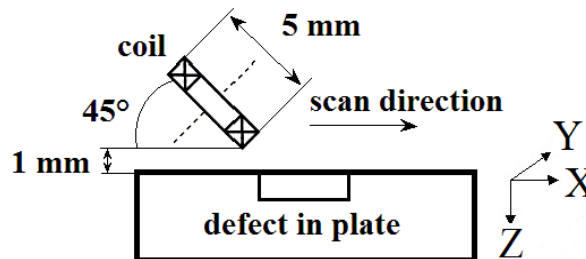
Fig. 3 The probe configuration after tilting

Thickness of conductive plate is $h = 10$mm and it has the electromagnetic parameters of the stainless steel SUS316L. Conductivity of this material is $\sigma = 1.35$ MS/m and its relative permeability is $\mu_r = 1$. The shape of nonconductive defects is rectangular and they are placed in the

middle of the conductive plate. The defects have a width of $w_c = 0.2$ mm, a length of $l_c = 10$ mm and their depth is varied and takes values d_c= [1, 3, 6 or 9] mm. Conductive plate and relevant defects are shown in Fig. 4.
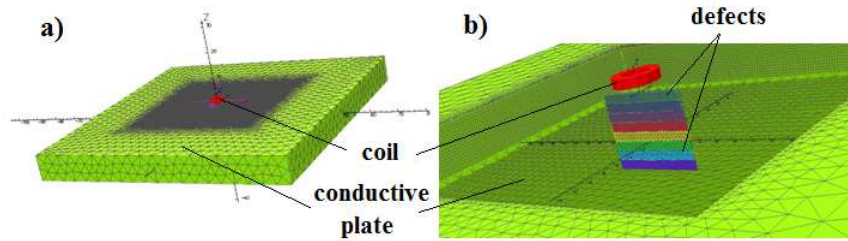
Fig. 4 Configuration of conductive plate and defects

The inspection of the material is realized as a 1D scan. ECT probe scans response signal from plate at five different configurations for each defect separately. The module of magnetic flux density B_{mod} is considered as response signals and it is expressed by equation (1). The resulting signal ΔB, displayed in the graphs, is obtained by subtracting the value of B_{mod} of a plate without defect from the value of B_{mod} of plate with defect.

$$B_{mod} = \sqrt{\operatorname{Re}\{B_Z\}^2 + \operatorname{Im}\{B_Z\}^2} \qquad (1)$$

3. Numerical simulations results

The aim of the implementation of simulations is to evaluate the effect of modification of the probe bank angle on a response signal and to find characteristic response signals for these configurations, which would increase the information value of measurements and provide more precise determination of defect position in the investigated material.

Scanning probe passes over the surface of the plate with the defect. In designated positions is performed the collection of data. The data from the entire plate surface and the overall distribution of magnetic flux density B is recorded for every scan position. All information is processed and how response signal is evaluated maximum value obtained at the scan position. In Fig. 5 is showed the change of the magnetic flux density when passing with the probe over the defect. Probe is parallel to the plate surface, $\varphi=0°$. Simulated defect in the x-axis has the edge at position x_1=-5 and x_2=5. Measurement using this configuration indicates peaks - predicts the edge - of the defect at position x_1=-6 and x_2=6. This method gives very high possibility of defect detection and can roughly estimate the position of the edge.

As the position of a detected and simulated defect doesn't completely agree, there's ambition to find new ways of detecting. The change of bank angle directly affects the response signal. The placement of the probe at the angle $\varphi= 45°$ in the x-axis (coincident with the direction of the scan) generates only one maximum peak and one minimum peak. These peaks don't coincide with peaks obtaining using parallel probe. Maximum peak is at the same position but with lower amplitude, shown in Fig. 6. The similar result is achieved by using reverse angle of $\varphi= -45°$ in the same axis. The resulting waveforms by this bank angle are symmetrical inverted about the y-axis at point x=0mm in comparison with a positive bank angle.
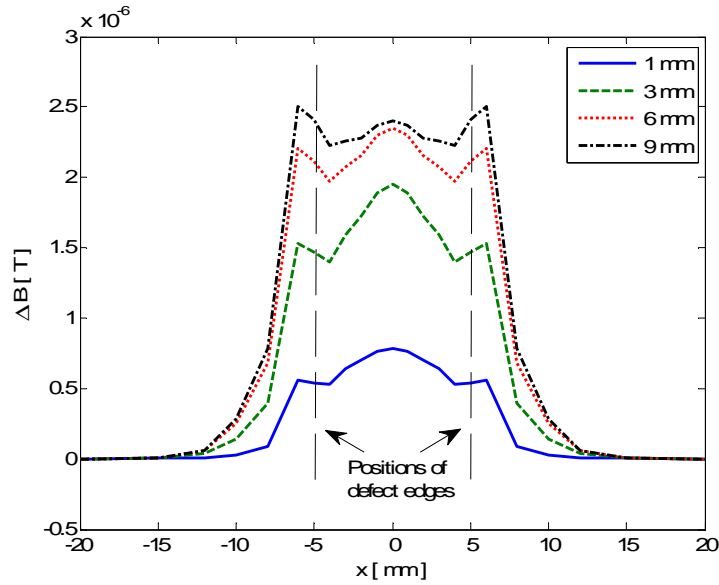
Fig. 5 Scan with parallel oriented probe
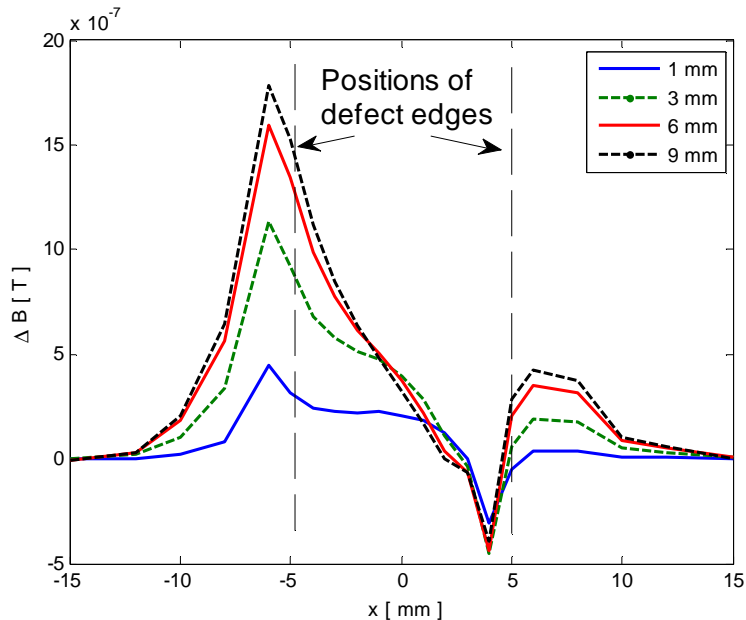
Fig. 6 Scan at 45° bank angle in x-axis

Interesting is the position of the minimum peak, that is located within the defect. Its distance from the edge seems to be equal to the distance of maximum peak from the estimated edge on opposite site of the defect. As shown in Fig. 7, using both response signals and their maximum and minimum peaks, it is possible to determine the position of the edge. The difference between the maximum and minimum value of the positions of the two measurements at reverse angles gives us the value a, which half $a/2$ specifies the distance of the real defect edge from one or the other peak value. Thus, the edge is identified at $x= -5$ mm, by position of maximum peak $x_{max}= -6$ mm and position of minimum peak $x_{min}= -4$ mm, using equation (2).

$$x = x_{max} \pm a / 2 \qquad (2)$$

The same way is detected the second edge by the value of b, shown in Fig. 7. Simulations are performed for four different depths of the defect. In all are found identical results and there are found edges corresponding to the simulated defect.
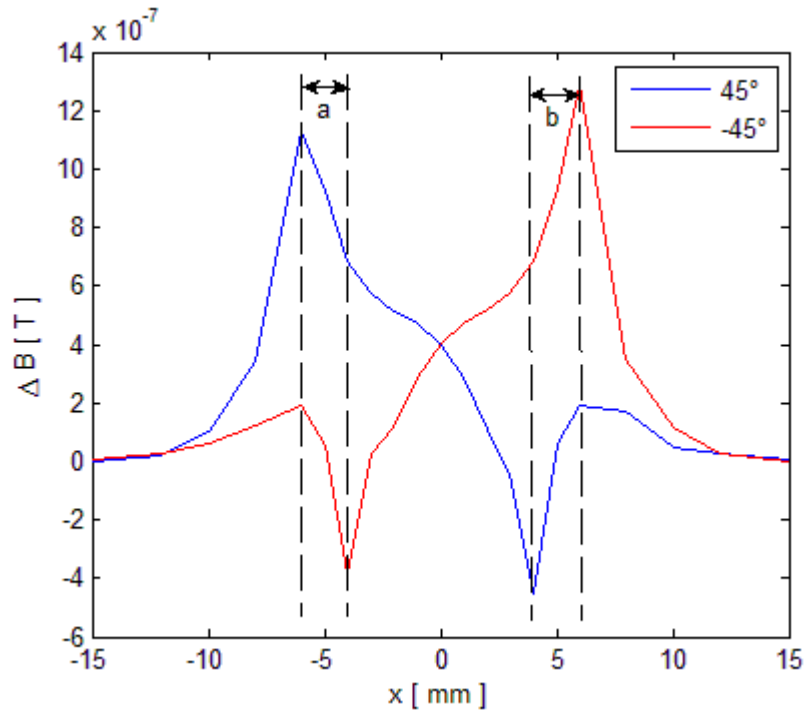
Fig. 7 Identification of the defect edges

The placement of the probe at the angle $\varphi_1 = 45°$ and $\varphi_2 = -45°$ in the y-axis (perpendicular to the scan direction) generates again two maximum peaks similar as parallel oriented probe. In this case are both maximum peaks with lower amplitude but directly determine a position of the defect edges. Their positions are same as positions of the edges in simulated defect and higher values of the amplitudes are located along the entire defect, shown in Fig 8. The defect is so very precisely and directly determined by both bank angle orientations. This approach is greatly influenced by the value of the frequency. Edges of the deeper defects are good visible, but less deep defects are hard to recognize. For accurate detection is therefore necessary to adjust the parameters of detection probe.
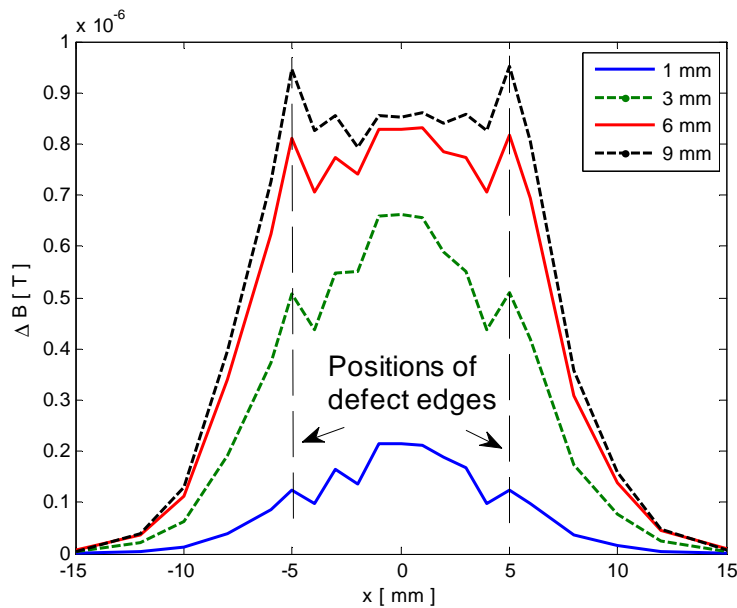
Fig. 8 Scans at 45° bank angle in y-axis

In appropriately selected frequency for a given defect is it possible to determine the value of c, equal to the distance of the position of boundary peaks. It's same for both angles and determines the length of the defect, shown in Fig. 9.
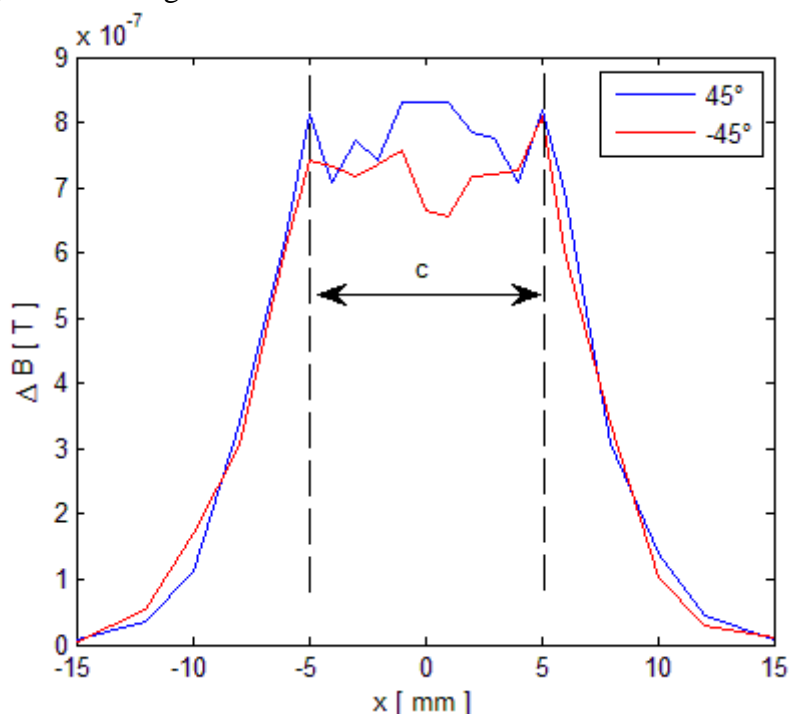
Fig. 9 Identification of defect edges

4. Conclusion

Use of ECT probe at different bank angles brings compared to the classical use additional information and more precise localization of inhomogeneities in the material. From the simulations suggests that it is possible at a certain bank angle of probe to accurately determine edges of defect and the length of this defect. Information value of response signal for detecting the defect depth is comparable to that in standard use of eddy current method and ECT probe. This paper shows the usefulness of this approach in the identification of inhomogeneities. With mutual combination of information from response signals values at various bank angles is possible more accurate determination of the defect edges and so the possibility of reconstruction of their shape.

Next step of this research will be to verify the simulated data on real defects and the pursuit of recognition and classification of the defects with different shape.

References

[1] CHUDÁČIK, V, JANOUŠEK, L., SMETANA, M, STRAPÁČOVÁ, T. *Impact of selected defect parameters on 3D eddy current testing response signals*. In *ELEKTRO 2014: proceedings*. [CD-ROM]. Žilina: IEEE, 2014, p. 558-561. ISBN 978-1-4799-3720-2.

[2] UHLIG R.P., ZEC M, BRAUER H.: *Lorentz Force Eddy Current Testing-model experiments and Numerical Calculations for Deep Lying Defects*, Electromagnetic Nondestructive Evaluation (XVI), Studies in Applied Electromagnetics and Mechanics, Vol. 38, IOS Press 2014, ISSN 1879-8322, pp. 66-73.

[3] JANOUŠEK, L., SMETANA, M., STRAPÁČOVÁ, T., REBICAN, M., DUCA, A. *Advanced procedure for non-destructive diagnosis of real cracks from eddy current testing signals*. In *ELEKTRO 2014: proceedings*. [CD-ROM]. Žilina: IEEE, 2014, p. 567-570. ISBN 978-1-4799-3720-2.

[4] ŠTUBENDEKOVÁ, A. – SMETANA, M. – JANOUŠEK, L. *Non-destructive testing of artificial knee joint by eddy current method*. In Proceedings 10th International Conference 2014 ELEKTRO: proceeding. [CD/ROM]. IEEE. Žilina: University of Zilina, 2014, p. 630-633. IEEE Catalog Number: CFP1448S-CDR, ISBN 978-1-4799-3720-2.

[5] RAO, B. P. C., *Practical eddy current testing*. Alpha Science International. Limited, 2007, ISBN 978-1-84265-299-2

FEM-assisted Analysis of Spatial Harmonics of Synchronous Generator's Air Gap Magnetic Field

[*]Jarosław Kurkiewicz
[*]Kielce University of Technology, Faculty of Electrical Engineering, Automatic Control and Computer Science, Department of Power Electronics, Electrical Machines and Drives, al. Tysiąclecia P.P. 7, 25-314 Kielce, Poland, jkurkiewicz@tu.kielce.pl

Abstract. The paper presents concepts related to analysis of higher harmonic content of magnetic flux density in the air gap of a cylindrical synchronous generator. It describes a successful simulation process using FEMM software package and identifies sources of spatial harmonics in an aforementioned machine. The influence of stator and rotor construction details on spatial harmonic content is also presented

Keywords: air gap, magnetic flux density, spatial harmonics, finite element method, FEMM.

1. Introduction

Constant evolution of numerical methods, computer hardware and Finite Element Method algorithms makes it possible to achieve highly accurate results in a potentially shorter time than traditionally used analytical or experimental methods. FEM analysis using dedicated computer software requires relatively simple geometrical model and basic material data to calculate magnetic fields in even most complex magnetic circuits.

The nature of FEM software makes it particularly well suited for pre-prototyping analysis of chosen generator geometry in relation to the presence of higher spatial harmonics in its air gap. Excessive content of higher spatial harmonics in generator's air gap is highly undesirable as those harmonics directly influence the shape of induced voltages. Voltage and current distortions may cause additional losses and temperature increase, electromagnetic interference and torque ripple. Discontinuous placement of winding in an electrical machine coupled with permeance inconsistency along machine's air gap are the main reasons behind higher spatial harmonics generation [1].

The paper presents an approach to identify spatial harmonics related to the geometry of an 8.5kVA synchronous generator equipped with a skew-less rotor developed in-house. Analysis is conducted with a freely available "FEMM" software package by David Meeker, which, while limited in its capabilities compared to commercial offerings, is more than adequate for this task. Proper identification of spatial harmonic sources allows further fine tuning of selected generator geometry before proceeding to prototyping stage.

2. Air Gap Spatial Harmonics' Relation to Induced Voltages

In most general terms the magnitude of internally generated voltage induced in a given stator is equal to:

$$E = K * \phi * \omega \qquad (1)$$

where:

K - construction constant of the machine,

ϕ- flux in the machine, ω - rotational speed

Magnetic flux going through a surface can be defined as the surface integral of the normal component of the magnetic field B.

$$\phi = \iint_S B \, dS \qquad (2)$$

where dS is an infinitesimal area element of surface S.

Since B=$\nabla \times$A an alternative way to compute flux would be to take the line integral over the boundary of the surface S.

$$\phi = \oint_{\delta S} A \, dl \qquad (3)$$

Equation (1) can be rewritten to represent the sum of all harmonics in the following manner [1]:

$$E_n = \omega * \sum_{n=1}^{\infty} K_{Wn} * N * \phi_n \qquad (4)$$

where:
K_{Wn} - winding factor for the n-th harmonic
N - turn count per phase
ϕ_n - flux for the n-th harmonic

Air gap flux related to the n-th harmonic is represented by the following equation:

$$\phi_n = \frac{2}{\pi} * \frac{\tau}{n} * B_{gn} * l_i \qquad (5)$$

where:
τ - pole pitch
n - harmonic order
B_{gn} - magnetic flux density of the n-th harmonic
l_i – ideal stator stack length

3. FEM Analysis of the Air Gap

To illustrate the concept of FEM-assisted air gap analysis a synchronous generator characterized by following parameters is modeled:

Rated power P_N = 8.5 kVA
Rated voltage U_N = 400 V
Rated current I_N = 15.25 A
Rated speed n_N = 3000 rpm
Rated power factor $\cos\varphi_N$ = 0.85

Described generator is a cylindrical machine with basic stator winding located in 36 evenly distributed semi-closed slots and skew-less rotor winding located in 2 groups of 6 semi-closed slots each. Also, removable aluminum damper cage bars are placed behind rotor's slot openings.

For simulation purposes several models of open-circuit, linear conditions were created. In every case a constant, rated excitation current of 2.82A was simulated. In order to identify sources of spatial harmonics of the air gap's magnetic field several different simplified model geometries were used.

In order to obtain magnetic flux densities a line integral was taken over a contour spanning full 360 degrees inside an air gap.

3.1. Full Model

The most complex model geometry is used to obtain a clear overview of simulated air gap's magnetic flux density. Fig. 1 shows a cross-section of the machine and Fig. 2 presents its magnetic flux density distribution along the air gap.
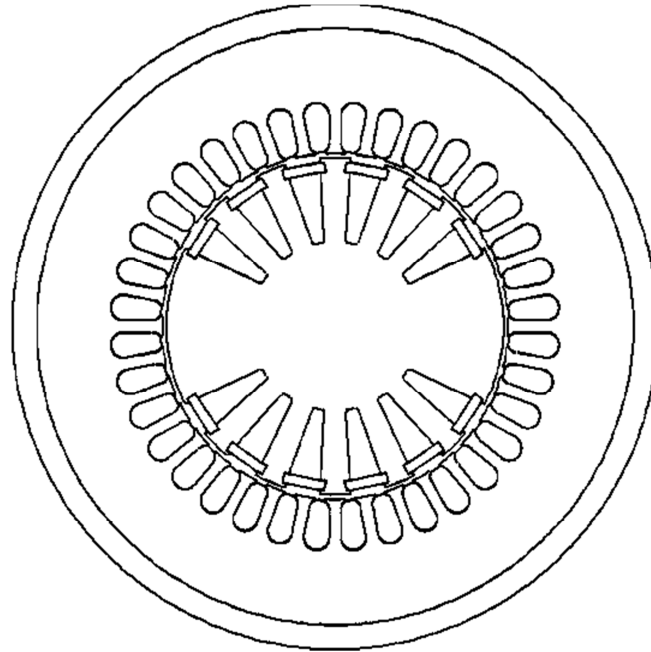
Fig. 1. Geometry of the simulated synchronous generator.
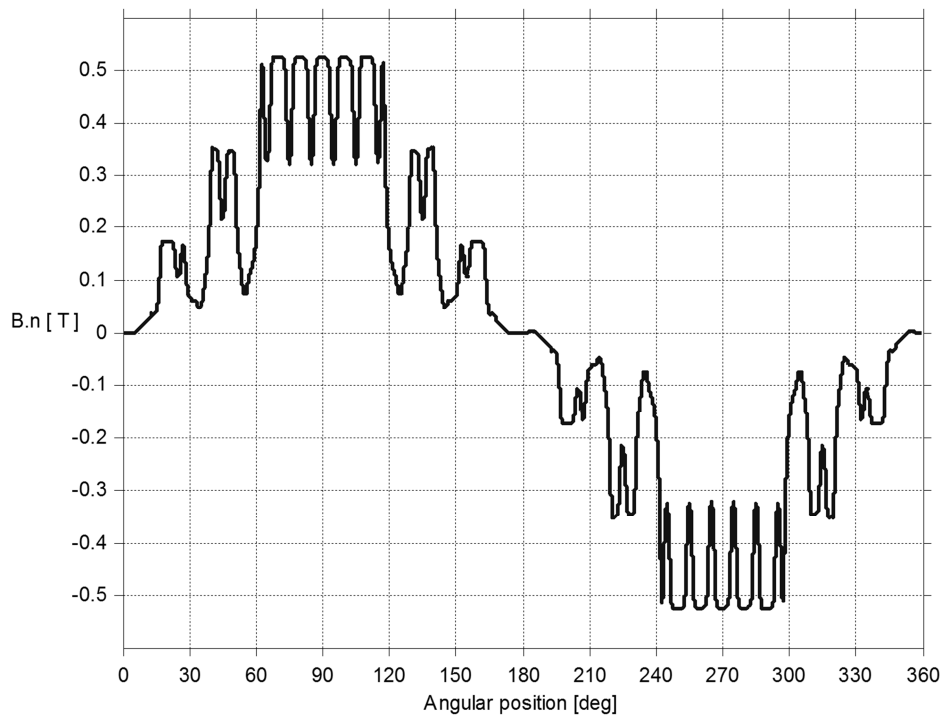
Fig. 2. Magnetic flux density distribution along the air gap.

As can be seen in Fig. 2. the magnetic field is heavily distorted and far from theoretical ideal sinusoidal distribution.

3.2. Harmonics Caused by Stator Slotting

Reducing the stator to a smooth surface removes harmonics caused by stator slotting from the model.
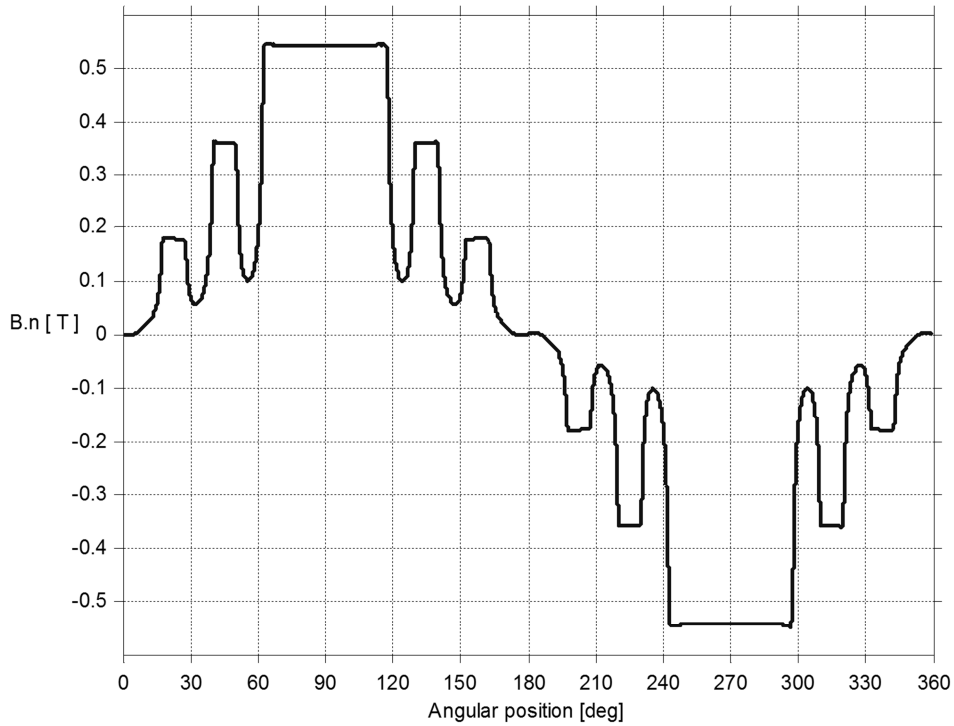
Fig. 3. Magnetic flux density distribution along the air gap. Stator slotting removed.
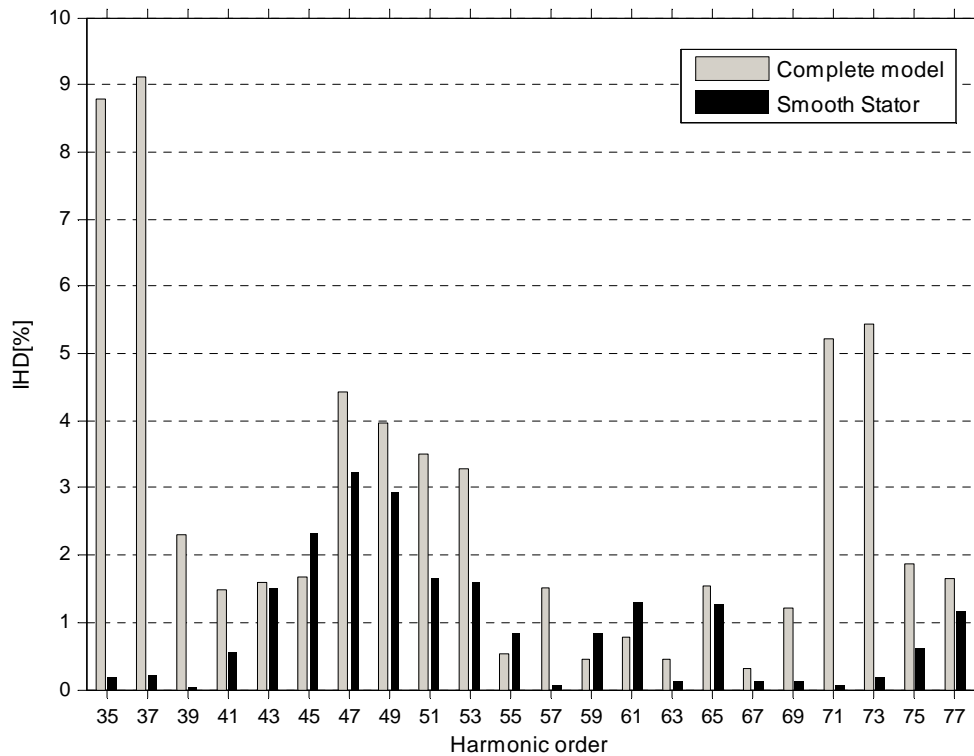
Fig. 4. Individual Harmonic Distortion for selected harmonics influenced by stator slotting.

Fig. 4. demonstrates a few chosen harmonics influenced by stator slotting. Amplitudes and subsequently IHDs were calculated by subtracting scaled FFT result of the simplified model's flux density from values based on the complete model. Apart from easily predicted 35th, 37th and 71st, 73rd slotting harmonics there are more harmonics of stator origin causing significant distortion.

3.3. Harmonics Caused by Rotor Slotting

Neglecting saturation effects allows further simplification of the model by means of closing the rotor slots. Obtained distribution shown in Fig. 5. is comparable to analytically-obtained distribution as presented in [2] and other works and differs mostly in regard to discrete winding arrangement.
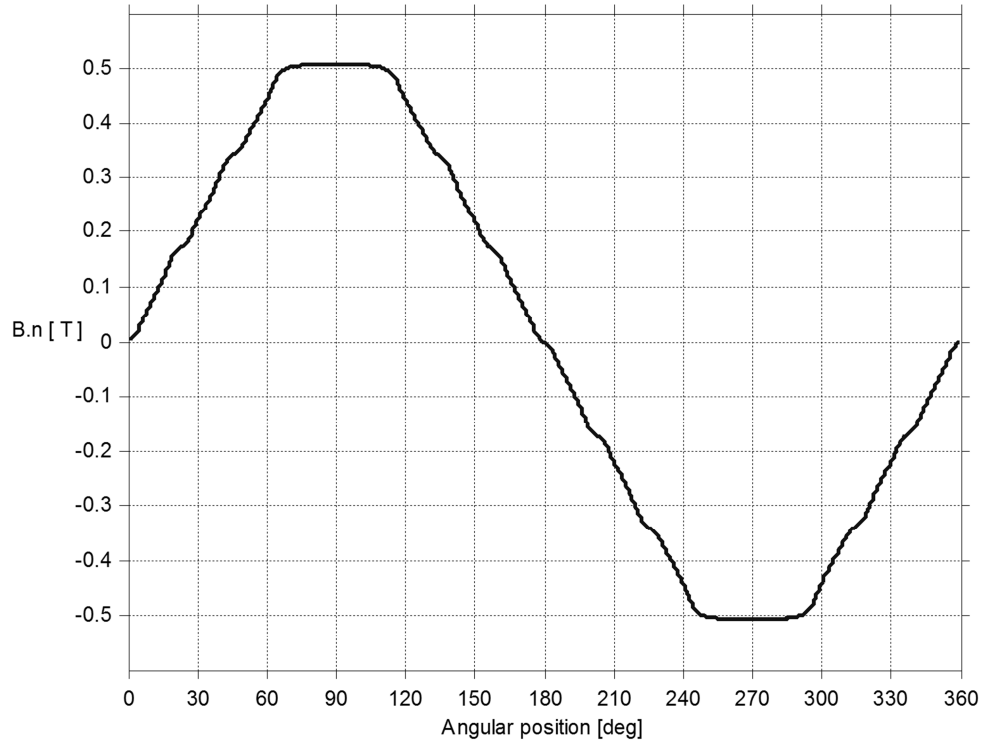
Fig. 5. Magnetic flux density distribution along uniform air gap.

When compared to previous results one can identify rotor slotting as a source of mainly 11th, 13th, 15th, 17th, 19th and other harmonics of higher orders. Chosen harmonics are shown in Fig. 6.
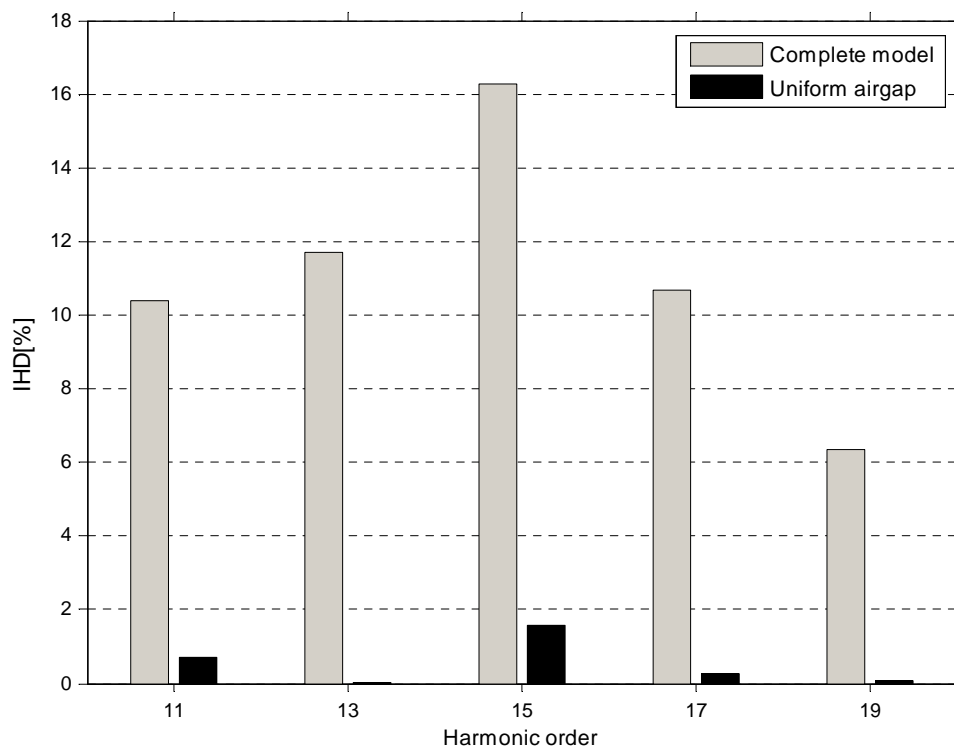
Fig. 6. Individual Harmonic Distortion for selected harmonics influenced by rotor slotting.

4. Methods of Reducing Spatial Harmonics Content

As can be deduced from (4) and (5) any change in the air gap magnetic field influences the harmonic content of the induced voltages. It is therefore important to reduce harmonic content of the magnetic field, which can be accomplished at design stage through several ways which were mentioned in numerous works such as [1] and [3]. Some of the most important methods include:

- Careful design of the air gap's length.
- Adjustment of the central tooth per pole pitch ratio in non-salient pole rotors.
- Skewing the rotor.

It is also worth mentioning that through the use of fractional winding in the stator it is possible to avoid magnetomotive force harmonics produced due to the stator slotting and coil placement. Those harmonics do not influence the induced voltages but still cause additional rotor losses [1].

5. Conclusion

The paper presents a simple procedure that can be used to identify sources of magnetic field's spatial harmonics using freely available software. Presented method requires only one computation of a single position in order to obtain a full 360 degree distribution of magnetic field along the air gap. Moreover, described process allows selective analysis of machine's geometry influence on magnetic flux density inside the air gap. Simulation results compare satisfactorily with experimental ones. Problems introduced by excessive harmonic distortion of the magnetic field are being actively investigated and presented simulations were part of an ongoing research.

References

[1] BOLDEA, I. *Synchronous Generators. The Electric Generators Handbook*. Boca Raton: CRC Press, 2006.

[2] PLAMITZER, A. *Maszyny Elektryczne*. Warszawa: WNT, 1986.

[3] LUDWINEK, K. *Przegląd najważniejszych metod ograniczania zawartości wyższych harmonicznych*. Elektro.Info, No 7/8, 2014.

[4] PYRHONEN, J., JOKINEN T., HRABOVCOVA, V. *Design of Rotating Electrical Machines.* Blackwell: Wiley, 2013

Some applications of fractional calculus to the analysis of dynamic properties of selected measuring transducer

[*]Mirosław Luft, [*]Elżbieta Szychta and [*]Daniel Pietruszczak
[*]Kazimierz Pułaski University of Technology and Humanities in Radom,
Faculty of Transport and Electrical Engineering, Malczewskiego 29, 26-600 Radom, Poland,
E-mail: m.luft@uthrad.pl; e.szychta@uthrad.pl; d.pietruszczak@uthrad.pl

Abstract. The paper outlines the use of fractional calculus for dynamic measurements while developing a method of improved description of dynamic properties of measuring transducers and measurement systems, which the authors considers to be the original and unique achievement of their work. The work's main objective is an implementation of a fractional calculus-based method allows for a description of dynamic properties of signal processing of measuring transducers with arbitrary orders.

Keywords: fractional calculus, measuring transducer

1. Introduction

The problem of notating dynamic properties of objects by means of fractional calculus although well known since the times of Gottfried Wilhelm Leibniz [4], yet due to restrictions resulting from lack of appropriate calculation methods and possibilities of their verification (among others connected with the lack of the calculating potential of earlier computers) has always been ignored.

At present technical and calculation possibilities cause that the problems related to these limitations have, to a large extent, been solved. There are more and more publications dealing with the topic of fractional order differential equations.

Majority of them, however, deal with theoretical aspects of the problem. There are no publications which put strong emphasis on the practical application of fractional calculus and combining theory with real applications.

The aim of this paper is to investigate how models of accelerometers based on the fractional calculus notation convey their dynamic behaviour in comparison to models represented by differential equations of integer orders and in comparison to processing characteristics of their real counterparts [2], [3], [5] and [6].

2. Model of the 2nd order measuring transducer

Simulation and laboratory testing of a second-order measuring transducer - accelerometer has been tested in this paper, treated as a representative group of measuring transducers (Fig. 1.).
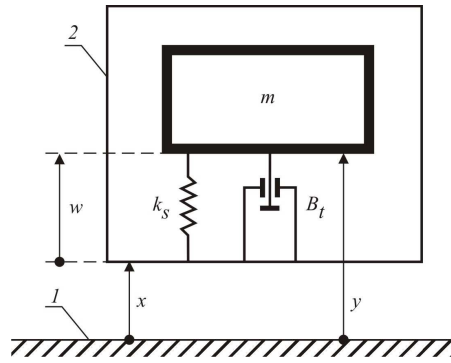
Fig.1. Kinetic diagram of an accelerometer: m – seismic mass, k_s – spring constant, B_t – damping coefficient, x – object motion relative to a fixed system of coordinates, y – motion of a vibrating mass relative to a fixed system of coordinates, w – motion of a vibrating mass relative to a vibrating object

A differential equation describing the absolute motion of a second-order measuring transducer's seismic mass can be expressed as:

$$\frac{d^2}{dt^2}y(t) + 2\zeta\omega_0\frac{d}{dt}y(t) + \omega_0^2 y(t) = \omega_0^2 x(t) + 2\zeta\omega_0\frac{d}{dt}x(t) \qquad (1)$$

where: $\omega_0 = \sqrt{\dfrac{k_s}{m}}$, $\zeta = \dfrac{B_t}{2\sqrt{k_s m}}$ and $k = \dfrac{1}{k_s}$.

Considering the motion of the vibrating mass relative to the vibrating object (Fig. 1):

$$\frac{d^2}{dt^2}w(t) + 2\zeta\omega_0\frac{d}{dt}w(t) + \omega_0^2 w(t) = -\frac{d^2}{dt^2}x(t) \qquad (2)$$

Depending on selection of k_s, m and B_t, a transducer can serve to measure acceleration as an accelerometer assuming a high k_s, low m and B_t. In practical vibration measurements, acceleration-measuring transducers, the so-called accelerometers, are employed. For purposes of simulation testing, a measuring transducer was assumed of a frequency $f = 350 Hz$, that is, circular frequency of free vibrations $\omega_0 = 2200\dfrac{rad}{s}$ and degree of damping $\zeta = 0.2$. Dynamics of such a transducer, characterised by means of a 2nd-order differential equation (2), are described by operator transmittance:

$$G(s) = \frac{W(s)}{\ddot{X}(s)} = \frac{1}{s^2 + 880s + 4.84\cdot10^6} \qquad (3)$$

Figure 2 illustrates amplitude and phase frequency characteristics of a measuring transducer with operator transmittance (3).

3. Quasi-fractional model of the measuring transducer

Equation (1), describing the measuring transducer, can be expressed as a difference equation:

$$a_2 w_k + a_1 w_{k-1} + a_0 w_{k-2} = b_2 x_k + b_1 x_{k-1} + a_0 x_{k-2} \qquad (4)$$

or a matrix equation:

$$\begin{bmatrix} a_2 & a_1 & a_0 \end{bmatrix} \begin{bmatrix} w_k \\ w_{k-1} \\ w_{k-2} \end{bmatrix} = \begin{bmatrix} b_2 & b_1 & b_0 \end{bmatrix} \begin{bmatrix} x_k \\ x_{k-1} \\ x_{k-2} \end{bmatrix} \tag{5}$$

Equation (5) can have the following derivative-integral expression:

$$A_2 \Delta_k^{(2)} w_k + A_1 \Delta_{k-1}^{(1)} + A_0 w_{k-2} = B_2 \Delta_k^{(2)} w_k + B_1 \Delta_k^{(1)} x_{k-1} + B_0 w_{k-2} \tag{6}$$

where $\Delta_k^{(n)}$ is the discrete function's reverse difference [4], defined as:

$$\Delta_k^{(n)} f(k) = \sum_{j=0}^{k} a_j^{(n)} f(k-j) \tag{7}$$

When (7) is taken into account, (6) has the matrix expression below:

$$\begin{bmatrix} a_2 & -a_1 - 2a_0 & a_2 + a_1 + a_0 \end{bmatrix} \begin{bmatrix} \Delta_k^{(2)} w_k \\ \Delta_k^{(1)} w_k \\ \Delta_k^{(0)} w_k \end{bmatrix} = \begin{bmatrix} b_0 & -b_1 - 2b_0 & b_2 + b_1 + b_0 \end{bmatrix} \begin{bmatrix} \Delta_k^{(2)} x_k \\ \Delta_k^{(1)} x_k \\ \Delta_k^{(0)} x_k \end{bmatrix} \tag{8}$$

where: $A_2 = a_2, A_1 = -a_1 - 2a_0, A_0 = a_2 + a_1 + a_0$ and $B_2 = b_0 + b_1 + b_2, B_1 = -b_1 - 2b_0, B_0 = b_0$.

On comparing responses of the measuring transducer to the input sinusoid signal, it was described by means of three models using the above method:

1.) *Classic model* described with operator transmittance (9) – the same as formula (3). Operation of a transducer described with the equation was simulated for appropriately selected parameters: natural angular frequency and degree of damping:

$$G(s) = \frac{1}{s^2 + 880s + 4.84 \cdot 10^6} \tag{9}$$

2.) *Classic discrete mode*, derived from the operator transmittance model (9), described by means of discrete transmittance (10):

$$G(z) = \frac{1.667 \cdot 10^{-15} z^2 + 6.666 \cdot 10^{-15} z + 1.667 \cdot 10^{-15}}{z^2 - 2z + 0.999} \tag{10}$$

Response of a continuous object to a discrete input depends not only on values of this signal at a discrete moments of time but also on sampling time and the extrapolator used.

3.) *The quasi-fractional discrete model* is expressed with derivative integrals and described by discrete transmittance (11):

$$G(z) = \frac{z^2}{1 \cdot 10^{14} z^2 - 2 \cdot 10^{14} z + 1 \cdot 10^{14}} \tag{11}$$

Discrete transmittance (11) is produced by implementation of the method of determining quasi-fractional expression of the measuring transducer in MATLAB&Simulink. Reverse differences of the discrete function $\Delta_k^{(n)} f(k)$ were determined according to (6), which produced:

$$A_2 = a_2 = 1, A_1 = -a_1 - 2a_0 = 0, A_0 = a_2 + a_1 + a_0 = 0 \tag{12}$$

and:

$$B_2 = b_0 + b_1 + b_2 = 10^{14}, B_1 = -b_1 - 2b_0 = -2 \cdot 10^{14}, B_0 = b_0 = 10^{14}. \tag{13}$$

It can be noted that the model described by means of the discrete transmittance (11) correctly reproduces values of the input signal amplitude, like the model of transmittance (10). It can be noted in Bode frequency diagrams (Fig. 2) that the measuring transducer model determined by the derivative-integral method presents the dynamics of the classically determined model (the diagrams of the models coincide). This confirms that integral-order differential-integral calculus is a special case of differential-integral calculus of non-integral orders.

Measuring transducer models (10) and (11) have only been subject to simulation testing and do not fully represent real models but the simulations indicate that the quasi-fractional model (12) exhibits the same dynamics as the classic model. The 'apparent' time of stabilization of time diagrams – the time after which a model's description is independent from time – for the quasi-fractional model is the same as for the classic model.
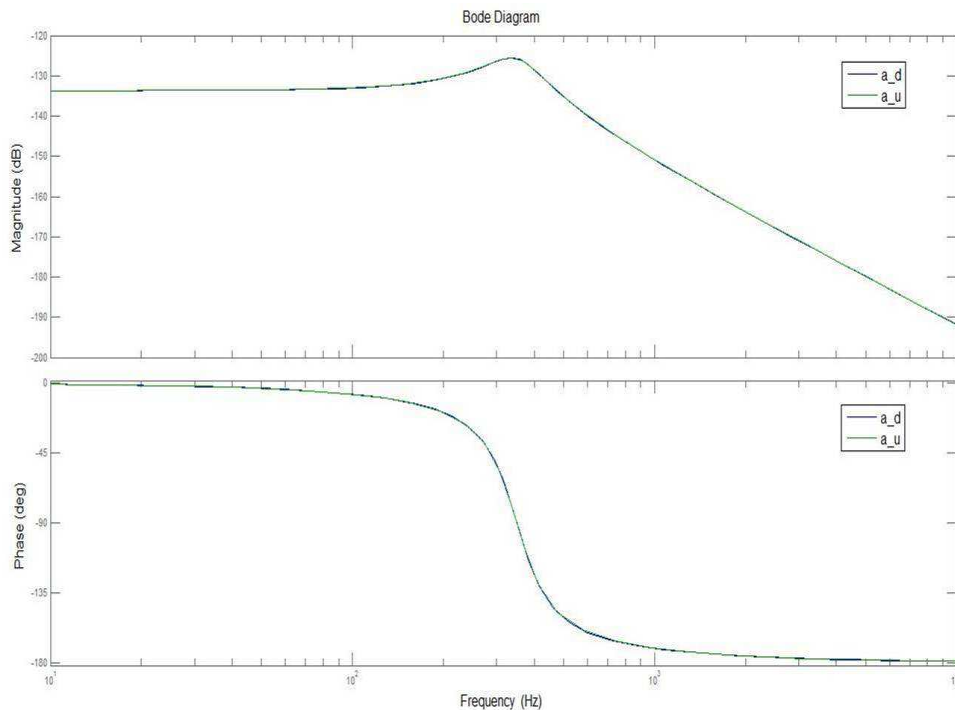
Fig.2. Comparison of Bode diagrams of measuring transducer models (10) and (11) (diagrams of the models overlap)

4. Model of a laboratory system of acceleration measuring transducer

An overview of the measurement system is shown in figure 3. In order to determine measuring transducer's operator transmittance, a system comprising two accelerometers *A1* and *A2*, conditioner and μDAQ USB-26A16 measurement card was modelled. Accelerometer DeltaTron by Bruel&Kjaer type 4507, sensitivity 10.18mV/ms^{-2} and the range of frequency measurements from 0.4Hz to 6kHz was tested. The conditioner's operating range was between 1Hz and 20kHz. The transducer was mounted on an electrodynamic inductor (5). A model accelerometer by VEB Metra, type KB12, sensitivity 317mV/ms^{-2} was aligned with the tested transducer.

The operator transmittance (14) describing dynamics of the measurement system was determined by identification with an external ARX (AutoRegressive with EXternal input). The voltage signal from the end of the tested measurement track is the identified signal, signal from the model accelerometer in response to the generator's sinusoid function of 100Hz is the comparative signal.
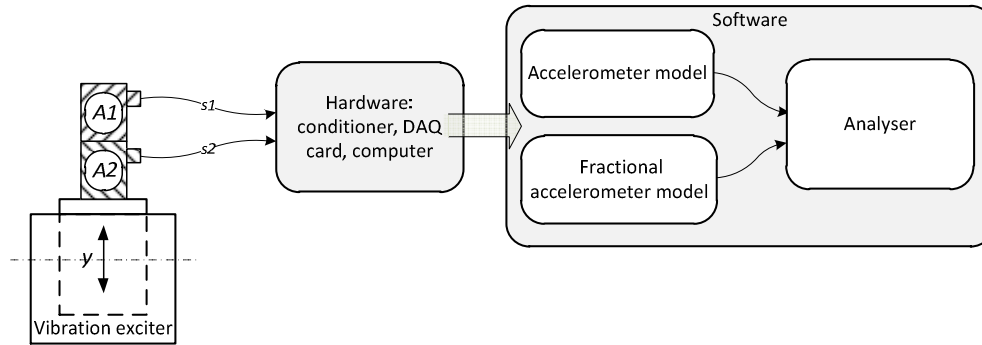
Fig.3. Laboratory measurement system for testing of mechanical vibration transducers: *A1*, *A2* – model and tested measuring transducers

The ARX identification method produced the operator transmittance $G(s)$ describing the system's dynamics:

1.) *Classic model*:

$$G(s) = \frac{0.03215s^2 + 1319.6s + 1.338 \cdot 10^6}{s^2 + 4.678 \cdot 10^4 s + 2.309 \cdot 10^7} \qquad (14)$$

2.) *Discrete transfer function* of the model was determined on the basis of the operator transmittance (14):

$$G(z) = \frac{0.03215z^2 - 0.05368z + 0,02163}{z^2 + 1.625z + 0.6264} \qquad (15)$$

The classic discrete model (15) was produced by discretising the classic model (14) by means of the 'Zero-Order-Hold' method with the sampling time $T_p = 10^{-4}$ s, for which Nyquist theorem of sampling frequency selection obtains.

3.) *Discrete transfer function of fractional models* was determined with a method implemented in MATLAB&Simulink. For varying increment of h, quasi-fractional transducer models become discrete transmittances which is presenting in table 1:

Increment variation h	Discrete transmittance $G(z)$
10^{-7}	$G_{f_1}(z) = \dfrac{3.228z^2 - 6.443z + 3.215}{100.5z^2 - 200.5z + 100}$
10^{-6}	$G_{f_2}(z) = \dfrac{3.347z^2 - 6.562z + 3.215}{104.7z^2 - 204.7z + 100}$
10^{-5}	$G_{f_3}(z) = \dfrac{4.548z^2 - 7.75z + 3.215}{104.7z^2 - 246.8z + 100}$
10^{-4}	$G_{f_4}(z) = \dfrac{1.775z^2 - 1.963z + 0.322}{59.09z^2 - 66.78z + 10}$
10^{-3}	$G_{f_5}(z) = \dfrac{2.69z^2 - 1.384z + 0.032}{70.87z^2 - 48.78z + 1}$

Tab. 1. Discrete transmittances of measuring transducer models for varying increment h.

The model of the real measurement system in the form of discrete transmittance and models expressed by means of a differential-integral equation were then compared. Both types of the models were based on the classic model derived by ARX identification method.

The simulations were carried out by ode3 integration method for a 100Hz sinusoid input signal.

Figure 4 shows logarithm frequency amplitude and phase diagrams of the measurement system models. It can be observed that, for the adopted increment of h, measure of differentiation accuracy, the diagrams clearly diverge. This means that other h increments, far lower than the sampling frequency, must be adopted.
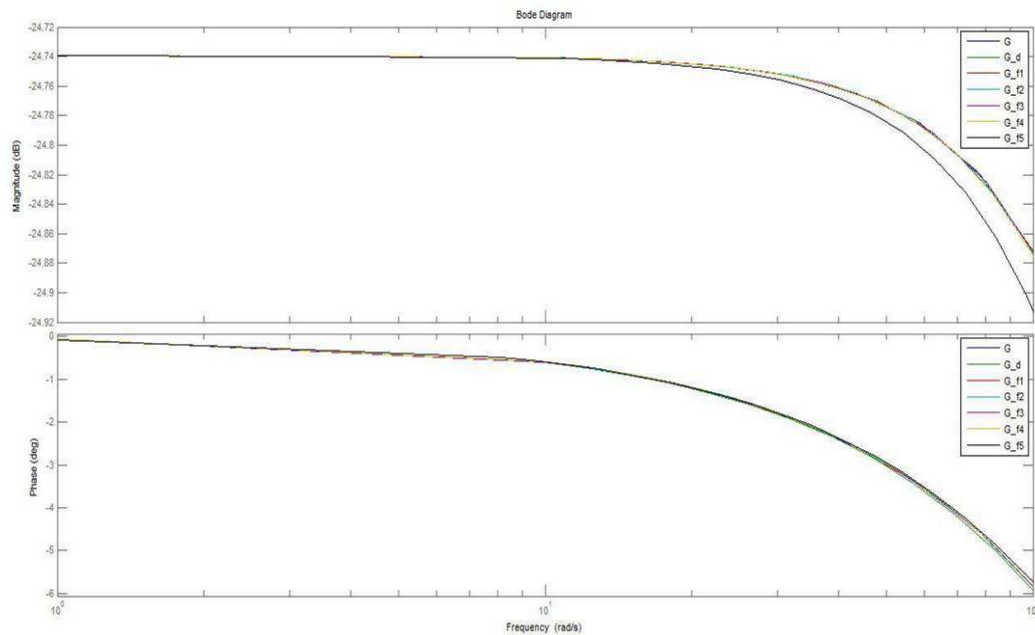
Fig.4. Bode frequency diagrams of measuring transducer models of transmittance (models from Table 1)

5. Conclusion

Dynamic development of recent research into the use of fractional calculus for the dynamic system analysis encouraged authors of this paper to attempt the use of it for the analysis and modelling of measuring transducers and measurement systems.

The work's main objective is an implementation of a fractional calculus-based method allows for a description of dynamic properties of signal processing of measuring transducers with integer-order and quasi-fractional-order. Fractional calculus is a generalisation of integral-order differential calculus – this is confirmed by laboratory testing of dynamic systems.

Effect of h on fractional measuring transducer's amplitude and phase diagrams has also been shown in this paper. In this cases h increments, far lower than the sampling frequency, must be adopted.

Application of the quasi-fractional method of describing dynamic properties of measuring transducers discussed in this paper, based on non-integral-order differential-integral calculus, will help to undertake analyses of simulated dynamics of various objects and processes which, due to their complexity, must be described by means of differential equations of any orders.

References

[1] KACZOREK, T. *Selected Problems of Fractional Systems Theory*. Springer-Verlag GmbH, 344 pages, ISBN 978-3-642-20501-9, Berlin, Germany 2011

[2] LUFT, M., CIOC, R., PIETRUSZCZAK. D. *Fractional Calculus in Modelling of Measuring Transducers*. *Electronics and Electrical Engineering*, No. 4(110), ISSN 1392-1215 (print), Kaunas, 2011.

[3] LUFT, M., SZYCHTA, E., CIOC, R., PIETRUSZCZAK, D. *Application of Fractional Calculus in Identification of the Measuring System*. Transport Systems and Processes, CRC Press Balkema, Taylor & Francis Group, pp. 63-68, ISBN 978-0-415-69120-8, London, UK, 2011.

[4] OSTALCZYK, P. *Epitome of the fractional calculus. Theory and its applications in automatics*. (Published in Polish), Wydawnictwo Politechniki Lodzkiej, p. 430, ISBN 978-83-7283-245-0, Lodz, 2008.

[5] PIETRUSZCZAK, D. *Application of fractional calculus to the analysis of dynamic properties of the measurement systems*. (Published in Polish), Doctoral dissertation, The Main Library of Kazimierz Pulaski University of Technology and Humanities, Radom, 2012.

[6] PIETRUSZCZAK, D., SZYCHTA, E. *Analysis of selected dynamic properties of fractional order accelerometers for application in telematics equipment*. Communications in Computer and Information Science, Springer-Verlag Berlin Heidelberg, 2013

Creating the User Interface and Algorithm in Interactive Environment Matlab

*Eva Luptáková, *Dagmar Faktorová,

*University of Žilina, Faculty of Eletrical Engineering, Department of Measurement and applied Electrical Engineering, Univerzitna 1, 01026 Žilina, Slovakia, eva.luptakova@fel.uniza.sk, dagmar.faktorova@fel.uniza.sk

Abstract. To determine the exact diagnosis the proper evaluation of electroencephalographic recordings recorded during polysomnographic examination is needed. These recordings have a length of 6 – 8 hours, so the analysis is time-consuming. Therefore, various techniques are being developed constantly, which are designed for automatic analysis of sleep EEG recording, what would shorten the time needed for analysis itself. In the article, we focus on the creation of a program, which consists of user interface and algorithm design for detection of sleep state NREM 1 and NREM3/4. User interface allows us to retrieve recording (it shows the first six channels in 30 seconds intervals), filtrate them, display basic information about the recording and detection of sleep states. We worked with interactive environment Matlab using graphical user interface design environment GUIDE. Detection is carried out using algorithm, which consists of several steps (adaptive segmentation, cluster analysis, detection itself using neural networks). At the end there was a hypnogram created, which was compared to a hypnogram created by the doctor and we evaluated the results achieved.

Keywords: Interface design, algorithm, adaptive segmentation, cluster analysis, hypnogram.

1. Introduction

The constant development of computer technology affects almost all the regions of human life. Health service is not an exception, either in ordinary or complex examinations, such as polysomnography, electroencephalography, electrocardiography and some other. Even at the end of the last century, the recordings of polysomnographic examinations were not stored in a digital form, but they were printed on the paper. Nowadays the recordings are stored digitally allowing further work and analysis of these recordings, their processing, sending, archiving and so on. The problem of these days is their visual evaluation, which is often time-consuming, at an average it takes 90 – 120 minutes. Today, there is still no software, which would facilitate the analysis of a given recording without doctor`s presence. The software solutions for working with digital data, that would automatically evaluate obtained recordings, are constantly developing and improving [1], [2], [3], [4].

2. User Interface Design

We designed the user interface in interactive environment Matlab using Graphical User Interface Design Environment (GUIDE).

We worked with EEG recordings data from file *.dat. The data format allows displaying of basic information using relevant addresses. The basic information includes patient`s name, surname, social security number, date of examination, sampling frequency, sensitivity, channels` names. The recordings are all-night records of adult patients. According to medical ethics, we will not state patient`s full name, or social security number.

The basis of user interface is two displaying windows. The first six channels are displayed in the first window and the hypnogram is shown in the second window. In addition to these windows, there is a slider and menu, which enables us to work with the records, contains items: *File, Filter, Information, Detection* and *Hypnogram.*

Slider is placed under the first displaying window and allows scrolling across the whole record and displaying individual channels in 30 second intervals. This makes it possible to browse the entire recording. For proper function of the slider it is needed to find out how many 30 second intervals there are in the recording and then according to this indication set the object slider and its properties *Max*, *Min* and *SliderStep.*
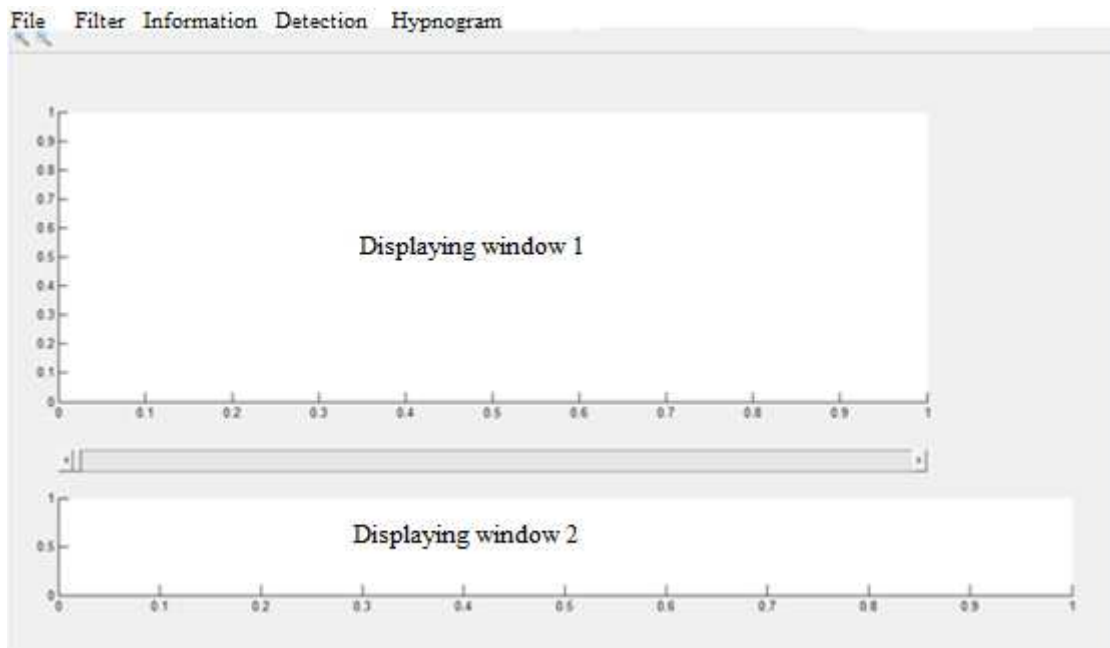
Fig. 1. User interface design.

Item *File* is a pull-down menu allowing opening and closing of PSG recording (*Open - Close*). Click *Open*, to display the selection dialog box with the possibility of choice of data.
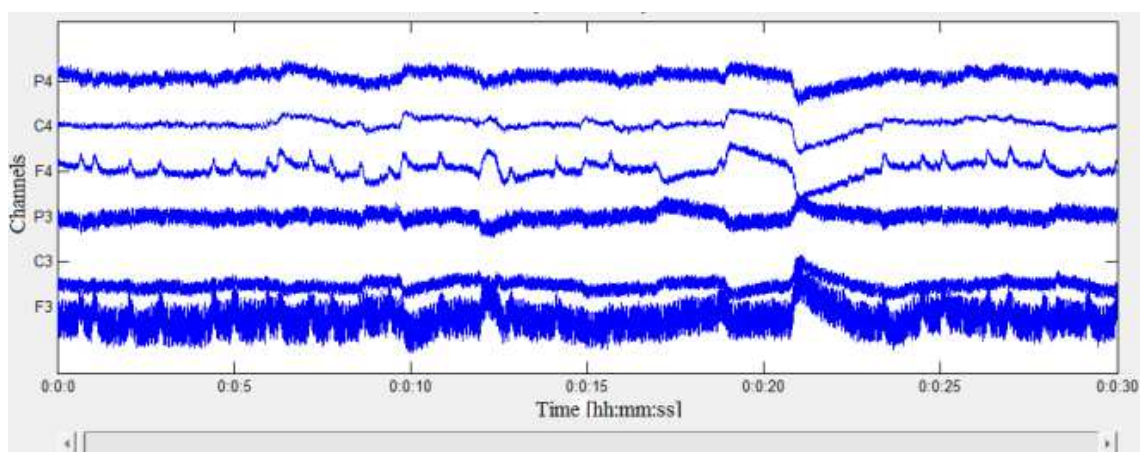
Fig. 2. The window with channels.

After opening, the first six channels of a given EEG recording load, the particular 30 seconds is drawn, what represents one epoch. Data are loaded from a file with *dat to a matrix. The number of rows of the matrix is equal to the number of channels shown and the number of channels is equal to sampling frequency times thirty. The displaying itself ensures the cycle and individual channels are

mutually shifted by 600 pixels. The record is displayed from the position in the file, where the position is converted to time data. This data is shown on x-axis in the form HH:MM:SS. On y-axis there is a labelling of individual channels (F3, C3, P3, F4, C4, P4). The record contains other channels (EOG, EMG, ...), but these are not important so we will not display them. Scrolling across the entire record is provided by the slider, which was already mentioned. The option *Close* closes the whole graphical user interface.

The next item is *Filter*. Since the recording contains not only useful signal but also AC noise, which is manifested by highlighting of harmonics of 50 Hz, it is needed to be filtered. Band-stop filter IIR (infinite impulse response) with cut off frequencies *fpass1* = 48 Hz, *fstop1* = 49 Hz, *fstop2* = 51Hz, *fpass2* = 52Hz is used, where fpass is band-pass frequency and fstop is band-stop frequency.
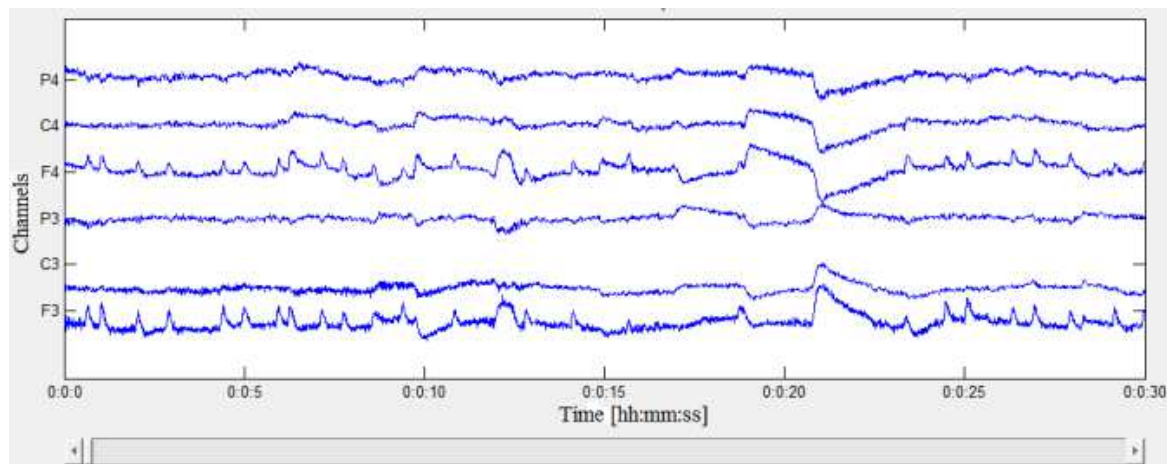
Fig. 3. Window with filtered channels.

The item *Information* potentiates to activate module with basic information about loaded recording. There is patient`s name, surname, date of examination, the number of channels, sample rate and recording length.

The next item is *Detection*, it is a drop-down list and it includes items *Adaptive Segmentation*, *Cluster Analysis* and *Sleep States*. These items are used to detect sleep states itself.

The last item is Hypnogram. It causes displaying of hypnogram from states detected.

3. The Algorithm for Detection of Two Sleep States

The detection itself consists of 4 steps:

1. Creation of quasi-stationary intervals (segments) of different epochs,
2. The division of individual segments into classes,
3. Detection of sleep states,
4. Creation of hypnogram from detected sleep states

3.1. Adaptive segmentation

The first step is to create segments from individual epochs. It is implemented through adaptive segmentation, especially using the standard deviation method. The standard deviation method is based on moving of the window of signal. The window has a length 128 samples. The standard deviation is calculated the window is moved one sample forwards and standard deviation is again calculated. These two values are deducted. Because limits of segments in EEG signal are not definite, it must be determined moving limit. The limit is determined by finding of local extremes of

the difference of standard deviation curve, where local extremes are local maxima and minima of the function [3], [5], [6].

The obtained segments need to be further described (using symptoms), so that they can be classified into individual classes using cluster analysis. We used Hjorth parameters and the amplitude value (the difference between maximal and minimal value) [3], [5].
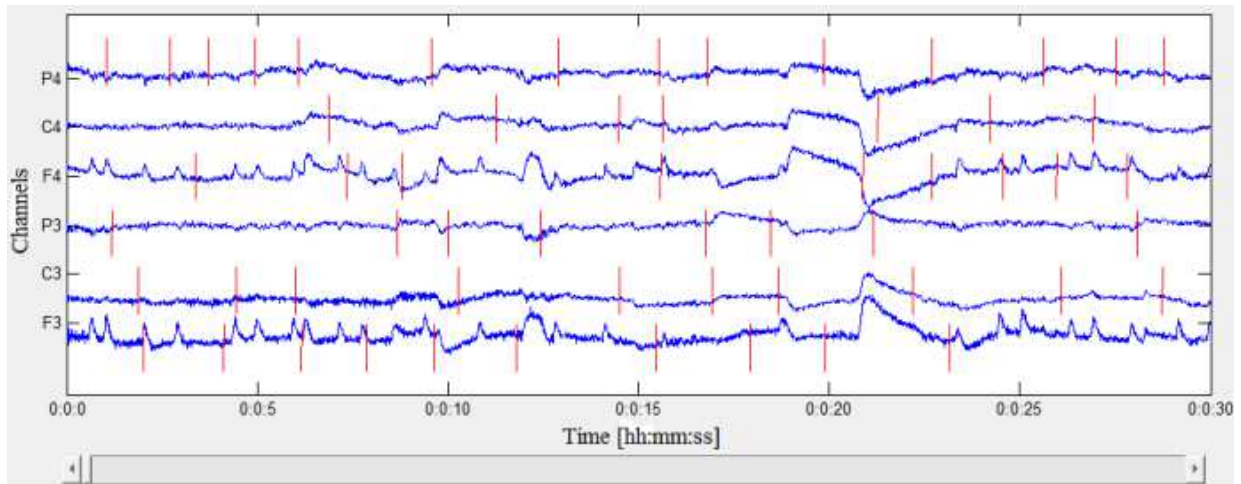
Fig. 4. Method of adaptive segmentation of standard deviation on a multi-channel EEG.

3.2. Cluster analysis

The second step is the alignment of individual segments into classes. It is implemented using cluster analysis. Cluster analysis is used for object recognition. Objects are used to identify similarities or differences between data. We divided objects into homogeneous classes using method of cluster analysis. Objects are described by symptoms (Hjorth parameters, maximal frequency, amplitude...). We used the method k-means. This method divides a segment into a predetermined number of classes, in this case into 3 classes [3], [5], [6].
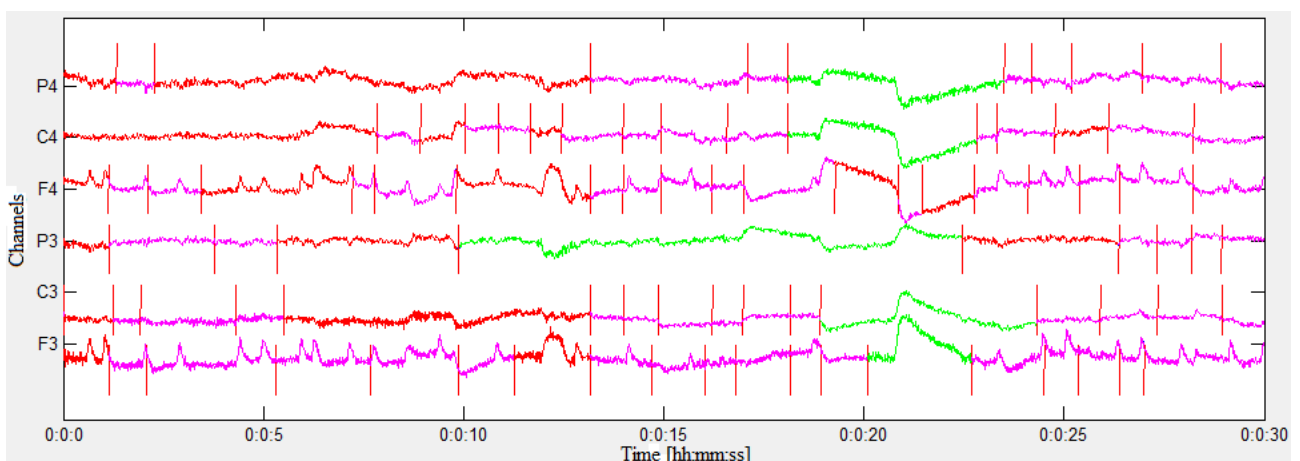
Fig. 5. Cluster analysis on multi-channel EEG.

3.3. Detection of sleep states

The next step is the determination of sleep states. Firstly we determined the priority class and then we applied neuronal networks on it. We trained two neuronal networks the first one distinguishes sleep states NREM3/4 and NREM2. The second one distinguishes NREM1 and wakefulness/REM. As we focused on detection of sleep states NREM3/4 and NREM1, the remaining sleep states were considered as one state [1], [3], [5].

3.4. Hypnogram

The last step is the creation of hypnogram from the states detected and its comparison with hypnogram created by the doctor. Individual detected sleep states were stored in a matrix using assigned number:

- Number 1 – corresponds to the states that were not priority for us (wakefulness NREM2, REM),
- Number 2 – sleep state NREM1,
- Number 3 – sleep state NREM3/4.
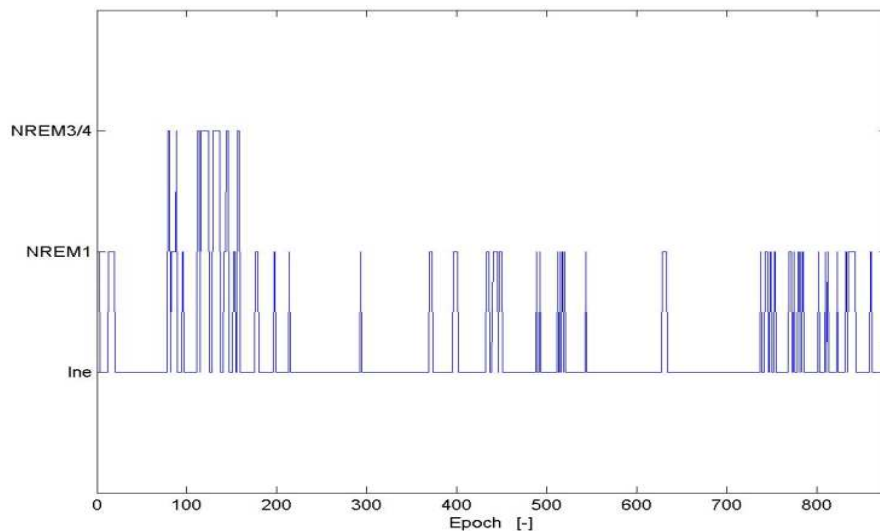
Fig. 6. Hypnogram created by program.
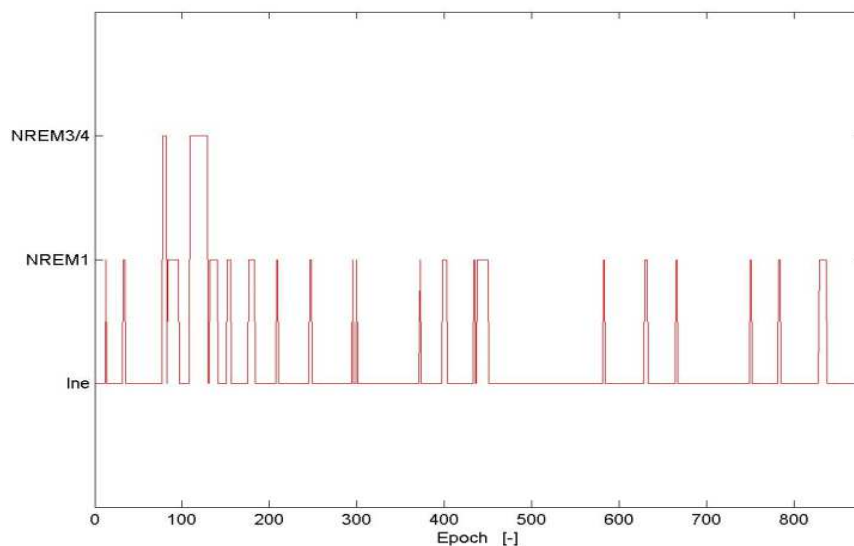
Fig. 7. Hypnogram created by the doctor.

4. Conclusion

In the article, we focus on the creation of a program, which consists of user interface and algorithm design for detection of sleep state NREM 1 and NREM3/4. . We worked with interactive environment Matlab using graphical user interface design environment GUIDE. The rate of success of this algorithm is 53,5 %. For the sleep state NREM1 the accordance 51,1 % and for the sleep

state NREM3/4   61,5 %. The algorithm could lead to shortening the time needed to analyze the recording and help the doctor in analysis of the recordings. The rate of success could be increased using more parameters to describe segments (maximum frequency, standard deviation and others), or using more channels e.g. EOG (Electrooculography).

References

[1] GALA, M.; BABUSIAK, B.; NOVÁK V. *Automatic creation of hypnogram.* Biomedical technology-2011 and Beyond, 47.

[2] GALA, M.; BABUSIAK, B. Sleep EEG automatic analysis. In: *Programmable Devices and Embedded Systems.* 2009. p. 242-247.

[3] GALA, M**.** Automatická detekcia a kvantifikácia spánkových stavov detí. *Doktorandská dizertačná práca.* Ostrava: VŠB - Technická univerzita Ostrava, 2009.

[4] NOVÁK, R. Hodnocení EEG signálu v reálnom čase. Praha : České vysoké učení technické v Praze, Fakulta elektrotechniky, 2011.

[5] GOMBÁRSKA, D.; BABUŠIAK, B.; GÁLA, M. *Spracovanie signálov v lekárstve.* Žilina: EDIS vydavateľstvo Žilinskej univerzity v Žiline, 2013. ISBN 978-80-554-0669-5.

[6] MOHYLOVÁ, J.; KREJČA, V**.** *Zpracování biologických signálů.* Ostrava : Editačné stredisko VŠB - TOU, 2006**.** 987-80-248-1491-9.

Comparison of inhibited growth caused by low frequency electromagnetic field on two different microorganisms

[*]Ivona Malíková, [*]Ladislav Janoušek,

[*] Department of Electromagnetic and Biomedical Engineering, Faculty of Electrical Engineering, University of Žilina, Univerzitná 2, 01026 Žilina, Slovakia
ivona.malikova@fel.uniza.sk
ladislav.janousek@fel.uniza.sk

Abstract. The article discusses comparison of inhibited growth of two microorganism exposed to low frequency electromagnetic field and the non-thermal effect of the field. Mechanisms by which the low-frequency electromagnetic field affects cells of biological systems vary a lot. In this paper the attention is focused on the ion parametric resonance and there is the basic explanation of this concept. According to this theory, the electromagnetic field impact evaluation is done. This topic became more and more relevant in present days and also there is an increasing amount of researches working in this area. Electromagnetic field and its radiation acquire increasing attention with growing use of electric machines and devices.

Keywords: low frequency electromagnetic field, Saccharomyces cerevisiae, Candida albicans, ion parametric resonance

1. Introduction

Contemporary era is characterised by plenty of new technologies that might not have positive impact on our bodies. Cell phones, Wi-Fi nets, artificial lighting, medical devices, etc. are few demonstrative examples. More and more discussions about influence of electromagnetic field on living organisms appear. Studies which proclaimed no effect or other researches stating impact of electromagnetic field began few decades ago. Many current studies concerns on possibility that the low frequency (LF) electromagnetic field (EMF) causes development of cancer. As reaction to this stimulus, laboratory experiments are accomplished. They admitted the connection between LF EMF and some types of tumorous conditions; however, these fields have to be with high intensity.

This paper is dealt with effect of low frequency electromagnetic field on two different types of microorganisms and the comparison of its effect. First microorganism is *Candida albicans*. It is a diploid fungus that grows as yeast and also as filamentous cells. It is the most common human fungal pathogen causing mucosal and systematic infections. [1] The second microorganism is *Saccharomyces cerevisiae* also known as baker's yeast. It is a convenient experimental organism for studying the influence of EMF on its growth. It serves as a valuable model for multicellular eukaryotes because of similarity in subcellular structures, and because of good knowledge about the biochemistry and molecular biology of yeast lipids. [2]

The effects of electromagnetic field studied in this article are non-thermal. The thermal effect is evident, but theories about the non-thermal effects diverge. This paper is focused on theory considering ions that are influenced by low-frequency electromagnetic field.

2. Non-thermal effects of electromagnetic field

Weak EMF can cause biological effects without generating consequential heat. EMF reduces the stability of living cells membranes. [3] Metallic ions, as calcium, potassium, magnesium are

contained in biological tissue. These ions are essential in cell structure, where according to researches potassium monovalent ions has lower impact on binding than divalent calcium ions. [4] It was proved that EMF can remove calcium ions from membranes, which leads to reduced stability of cells. Experiments reveal that this effect occurs only in very weak EMF and in 'amplitudes windows' only. Below and above these 'windows', there is no effect. [4-7]

Tseĭslier et al., monitor adenosine triphosphatase (ATPase) activity. Short time exposure of protein solution by extremely low EMF leaded to decrease of ATPase activity comparing to control samples, that weren't exposed to an artificial EMF. This effect can be explained by EMF influence on dynamic properties of actomyosin solutions based on spontaneous dynamic formation of structure. In this reaction the calcium has very important role. [4, 8]

Erdal et al. [5] research cytogenetic effects in bone marrow cells from Wistar rats exposed to a 50 Hz, 1.0 mT magnetic field for 45 days with exposition of 4hours per day. Also experiments by Yang et al. [6] investigated the possible interaction between mutated genes for DNA repair enzymes and extremely low frequencies (ELF) EMF exposure in acute children leukaemia.

The paper concentrates on non-thermal effects of low frequency electromagnetic field and focuses on comparison in growth inhibition between *S. cervisiae* and *C. albicans* cultures. The cultures are exposed under conditions given by the ion parametric resonance theory. Specific frequency is applied on both samples. The growth rate of the cultures is evaluated by comparing to reference samples and consequently the difference between growth rates of both organisms is discussed. Impact of EMF on the culture is then assessed. [9]

2.1. Ion parametric resonance

The ion parametric resonance (IPR) model is considered for the background of this study. IPR predicts that biological responses occur at particular magnetic field combinations which establish ion resonances. In Tab.1 there are shown the parameters for resonance of various ions. These parameters are calculated for flux density of Earth magnetic field. The model was later improved by Blackman and Blanchard. They predicted different MF interactions with biological systems based on selective relation among four factors: flux density of static MF, frequency and flux density of parallel alternating current MF, and charge-to-mass ratio of ions in biological relevance. The model of IPR, mentioned in this article, covers invoke precession of ions and it is one of the most important subjects in many experimental investigations. [10-12]

Tab. 1. Resonance parameters

Ions	Q/m [μC/kg]	f_c/B_{ac} [Hz/μT]
H^+	95.76	15.24
Mg^{2+}	7.93	1.26
Ca^{2+}	4.81	0.77
K^+	2.47	0.39

3. Experimental part

The exposure system presents an exposure coil connected to generator to create EMF. The apparatus is designed to assure identical exposure conditions for both sample pairs – exposed and reference samples. The purity of used microorganism is secured by Czech collection of microorganisms (CCM), Masaryk University in Brno. *C. albicans* CCM strand 8186 and *S. cerevisiae* CCM strand 8191 are chosen for our experiments. [1]

Because of characteristics of microorganisms, *S. cerevisiae* is processed in broth solution whereas *C. albicans* in glucose solution. The solutions with microorganisms are placed to microtitration plates after that. One plate is placed to the coil, another one to the electromagnetic shielding box with the same ambient temperature as the exposed sample. After four hours of exposure the whole volume of exposed and reference samples are pipetted to specific agars. *C.*

albicans is placed to the blood agar and *S. cerevisiae* to the Sabouraud Dextrose Agar. Finally all Petri dishes are placed to an isothermal chamber with stable temperature 37°C for 24 hours. After that time, the samples are taken out from the isothermal chamber and the numbers of colonies in each plate are evaluated. This procedure is repeated four times for each microorganism what is shown in Tab.2, where column (1-4) represents new experiment.

Frequency 940 Hz and magnetic flux density of alternating current of EMF 1,22 mT are chosen according to the IPR theory. These parameters may be considered for resonance frequency of Ca^{2+} ions from Tab.1. Response of biological system, which is observed, corresponds to importance of calcium channels that influence cell cycle.

Tab. 2. Results and counts of measurements.

C. albicans	1	2	3	4
Reference	923	923	984	1024
Exposed	337	304	488	466
Exp/ref	0,37	0,33	0,50	0,45
Average ratio of exposed and reference sample:				0,41

S. cerevisiae	1	2	3	4
Reference	3147	2389	2459	2918
Exposed	1968	1842	1514	2437
Exp/ref	0,63	0,77	0,62	0,84
Average ratio of exposed and reference sample:				0,72
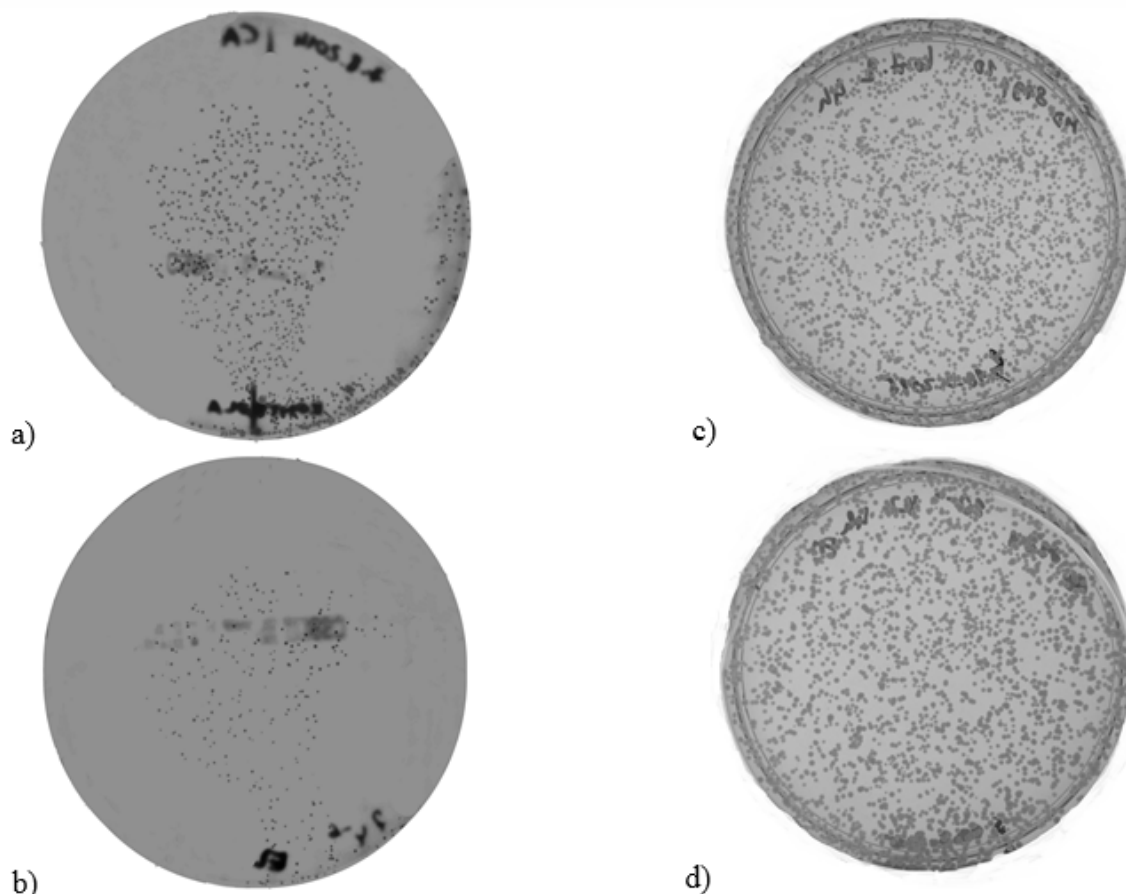
Fig. 1. Selected samples from experiment: a) first reference sample of *C. albicans* (923), b) first exposed sample of *C. albicans* (337), c) first reference sample of *S. cerevisiae* (3147), d) first exposed sample of *S. cerevisiae* (1968)

It can be seen from Tab.2 and Fig.1, that growth inhibition is higher for *C. albicans* than for *S. cerevisiae*. However, it is obvious that in both cases EMF inhibits the growth of microorganisms. For *C. albicans* exp/ref ratio varies from 0,33 to 0,5 with average value 0,41. For *S. cerevisiae* is this variety from 0,62 to 0,84 with average value 0,72. The reason for this difference may be caused by lower resistance of *C. albicans* to exposition and different structure of cells. *C. albicans* cell wall consists of carbohydrate (approximately 80 to 90%), proteins and lipids, while the cell wall of *S. cerevisiae* is more complex and similar to eukaryotic cell. [13]

Number evaluation of colonies is performed by software OpenCFU and selected samples are also counted manually. OpenCFU is shown to be very accurate and does not generate more errors than average human error. [14]

4. Conclusion

Presented article dealt with non-thermal effects and with impact of extremely low frequencies electromagnetic field on biological structures. It was especially focused on various growth inhibitions in two different samples of microorganisms - *Saccharomyces cerevisiae* and *Candida albicans.*

The paper focused on experiments to prove the veracity of ion parametric resonance theory. Conditions for all experiments were adjusted according to the IPR theory with frequency of 940 Hz and magnetic flux density of alternating current 1.22 mT. Microorganisms were exposed for 4 hours and evaluation of samples was performed after 24 hours. Assessment was performed by comparison of colonies amount in reference and exposed sample with software OpenCFU. Exp/ref ratio varied in each samples, but inhibit effect was visible in all cases. As the measurements were made with one specific strand, it would be appropriate to verify the same experiments with different to see whether the response is also strand-dependent.

Effect of ELF EMF was proven by experiments and as the amount of the sources of artificial ELF EMF is increasing and no generally accepted theory of EMF effect on biological systems was accepted yet, this topic begins to be more relevant nowadays.

Acknowledgement

References

[1] SMEEKENS, S. P. et al. *Functional genomics identifies type I interferon pathway as central for host defense against Candida albicans*. Nature communications, 2013, 4: 1342.

[2] DAUM, G., LEES, N. D., BARD, M., DICKSON, R. *Biochemistry, cell biology and molecular biology of lipids of Saccharomyces cerevisiae.* Yeast, 1998, 14: 1471–1510.

[3] GOLDSWORTHY, A. *The biological effects of weak electromagnetic fields.* 2012 http://www.hese-project.org/hese-uk/en/niemr/resonance1.php

[4] TSEĬSLIER, I. *Effect of electromagnetic field of extremely low frequency on ATPase activity of actomyosin.* Ukrainskiĭ biokhimicheskiĭ zhurnal, vol. 84, p.62-7, Sept-Oct 2012

[5] ERDAL, N. - GÜRGÜL, S. - ÇELIK, A.: Cytogenetic effects of extremely low frequency magnetic field on Wistar rat bone marrow. Mutation Research/Genetic Toxicology and Environmental Mutagenesis, 2007, 630.1: 69-77.

[6] YANG, Y., et al. Case-only study of interactions between DNA repair genes (hMLH1, APEX1, MGMT, XRCC1 and XPD) and low-frequency electromagnetic fields in childhood acute leukemia. Leukemia & lymphoma, 2008, 49.12: 2344-2350.

[7] KATO, M., SHIGEMITSU, T., MIYAKOSHI, J. *Electromagnetics in biology*. Tokyo: Springer, 2006.

[8] DANCKER, P. *The binding of calcium and magnesium to actomyosin and its modification by natural troposmyosin.* Pflügers Archiv, 1970, 315.3: 198-211.

[9] CHVOJKA, J. *Magnetoterapie v teorii a praxi.* Professional Publishing, Praha, 2000. 99s. ISBN 80-86419-01-0

[10] BLACKMAN C. F., BLANCHARD J. P. *Experimental determination of hydrogen bandwidth for the ion parametric resonance model.* Bioelectromagnetics, vol. 20, p.5-12, 1999

[11] BARABAS, J., RADIL, R. *Evidence of s. cerevisiae proliferation rate control via exogenous low frequency electromagnetic fields.* Information Technologies in Biomedicine. Springer Berlin Heidelberg, 2012, 295-303.

[12] RADIL, R., JANOUSEK, L. *Yeast growth influenced by parallel combination of time-varying and static LF EMF.* In Communications: scientific letters of the University of Žilina. ISSN 1335-4205, 2013, vol. 15, no. 2A, p. 28-32.

[13] CHAFFIN, W. L., et al. *Cell wall and secreted proteins of Candida albicans: identification, function, and expression.* Microbiology and Molecular Biology Reviews, 1998, 62.1: 130-180.

[14] GEISSMANN, Q. OpenCFU, a new free and open-source software to count cell colonies and other circular objects. *PloS one*, 2013, 8.2: e54072.

Measuring and Modeling Dielectric Properties of Poly Methyl Methacrylate

*Maria Papezova, *Dagmar Faktrova

*University of Zilina, Faculty of Electrical Engineering, Department of Measurement and Applied Electrical, Univerzitna 1, 010 26 Zilina, Slovakia, maria.papezova@fel.uniza.sk, dagmar.faktorova@fel.uniza.sk

Abstract. The structural integrity of any replacement has to be tested to prevent premature failure and thus maintaining the reliability of the implant. This article deals with possibility of dielectric properties measurement method (Hippel method) of biomaterial poly methyl methacrylate (PMMA) and microwave non-destructive testing (MNDT) of PMMA used by microstrip patch antenna. MNDT use principle of electromagnetism. The electromagnetic field in microwave frequency range (3-300 GHz) can penetrate through biological structures of human body and any biocompatible material. We used experimental procedure and subsequently we started realize the schemes and optimization of measurement methods in software simulation tool COMSOL Multiphysics.

Keywords: Antenna, biocompatibility, microwave non-destructive testing, miniaturization of material.

1. Introduction

Dental materials are made from a variety of synthetic products. The products are typically used to restore the patient's oral health, function and aesthetic appearance. The variety of dental material is limited properties as precisely specified mechanical and physical characteristics. The main role has biological tolerance of the material - biocompatibility. The used of polymers has revolutionized the biomedical industry ever since their discovery. The most used polymer is PMMA. PMMA used in denture dentistry.

Miniaturization of materials leads to increasing expansion of MNDT. The development of MNDT included the development of sensors, methods of calibration techniques to detection cracks, defects, cavities, various heterogeneities of materials etc. Monitoring dielectric properties of biomaterials, changes in material e.g. defects, especially in the microwave frequency range, exploring new possibilities of application new materials elements is very important to improve quality of biomaterials and level of treatment.

MNDT has two basic types of measures:
1) resonant,
2) non–resonant [1].

Resonant methods provide more accurate knowledge of the dielectric properties over a limited frequency range or only one of predetermined transmission frequency [2].

The general review of electromagnetic (EM) properties of material (impedance, speed of waves in materials, permittivity and permeability) are taken by non–resonance methods (with a limited frequency range). EM properties of the material can be derived from the partial reflection impact of the incident wave from the interface between two materials. In such a method a transmission line is needed to direct the wave to the material under test and then collect the reflected and/or the transmitted energy. This line can be coaxial, metallic waveguide, dielectric waveguide, planar transmission line and free space [2, 3].

EM waves can be propagated in two ways:
1) free–space methods operating in the fa –field using the antennas,
2) waveguide methods operating in the near –microstrip lines and waveguide [2, 4].

2. Experimental results

We chose non-resonant reflection waveguide method for measuring. This method determines accurately the dielectric constant of thin and moderate thick samples.
It eliminates the problems arising from any position offset of the dielectric slab in transmission/reflection methods.

2.1. Sample preparation

The basic parameters for measurement of EM field are the relative permittivity, loss factor and conductivity. We chose biomaterial PMMA to measure this basic EM parameter. PMMA is used in restorative dental medicine. The aim of this measurement was to show dielectric properties of PMMA.

Fig. 1: The used sample – PMMA

For measurement method was used Hippel method, which is considered as the most accurate waveguide method. This sample was adapted to the dimensions of waveguide WR-90 (dimensions 2.286 cm x 1.016 cm). This method is conducted in the X-band recommended operating range for the TE_{10} mode is 8.2 to 12.4 GHz [5].
Schematic diagram of Hippel method is on Fig. 2a).
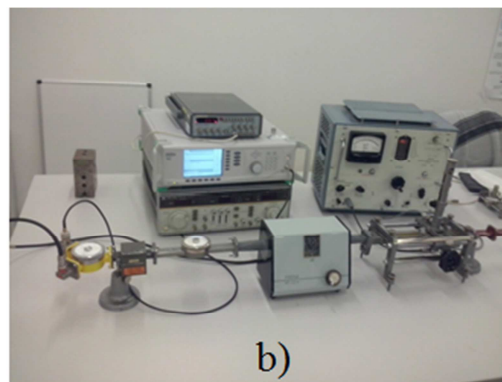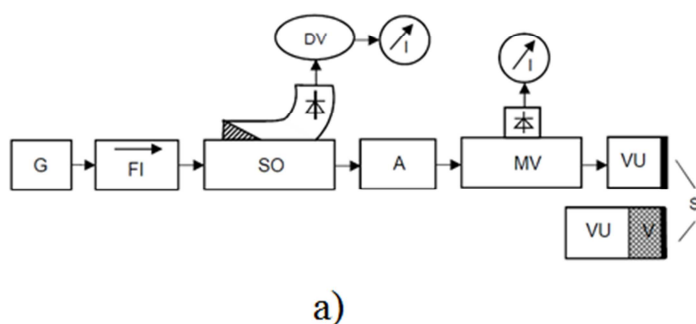
Fig. 2: a) Schematic diagram of the experimental set up, b) Our used workplace ordering of experimental measurements

G – high – frequency generator, FI – ferrite isolator, SO – directional coupler, A – attenuator, MV – measuring line, VU – waveguide section, V – measured sample, DV – cavity wavemeter, I –zero indicator, S – short circuit [5].

According to the relevant mathematical expression:

$$\varepsilon_r = \frac{\left(\frac{2\pi}{\lambda_c}\right)^2 + \beta^2 - \alpha^2}{\left(\frac{2\pi}{\lambda}\right)^2} \tag{1}$$

$$tg\delta_e = \frac{2\alpha\beta}{\left(\frac{2\pi}{\lambda_c}\right)^2 + \beta^2 - \alpha^2} \tag{2}$$

We can calculate relative permittivity $\varepsilon_r = 9.5$ and also loss factor $\mathrm{tg}\delta_e = 0.012$ of PMMA based on the measured values and mentioned mathematical expression (1) and (2). The calculated dielectric parameters are used in next simulation. These values are very indispensable for our next research, in which we want to create phantoms with the same dielectric properties as has PMMA.

3. Numerical results

It is important to know dielectric properties, changes in material, but also to classify the occurrence of inhomogeneities as on the surface so inside the structure. This part of work is considered on the first important simulation dependence of frequency and scattering parameter S_{11} in simulation tool COMSOL Multiphysics.

3.1. Microstrip Patch Antenna

One type of antennas is the microstrip patch antenna. In the last decades printed antennas have been mainly studied due to their advantages as easy to handle and low-cost, low power-handling capability of printed circuits. On the other hand, microstrip patch antennas have some disadvantages as narrow bandwidth, low gain, etc. We chose this type of antenna with regard to the size of studied object [6].

Basic structure of rectangular microstrip patch antenna consists of a radiating patch on one side of a dielectric substrate which has a ground plane on the other side as shown in Fig. 3.
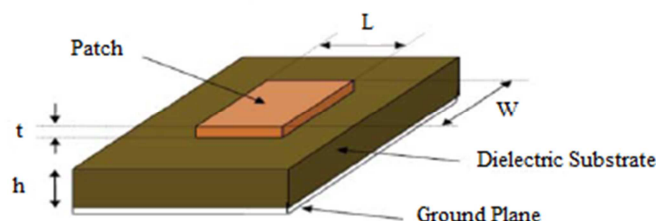
Fig. 3: Basic structure of rectangular microstrip patch antenna [7]

In simulation, we created microstrip patch antenna model with parameters, which are shown Tab. 1, whereas 'mil' is the unit mill inches, that is 1 mil=0.0254x10^{-3}m.

Name	Expression	Description
D	2[mil]	Substrate thickness
*W*_line	0.113[mil]	50 ohm line width
*W*_patch	5[mm]	Patch width
*L*_patch	5[mm]	Patch length
*W*_stub	0.5[mm]	Tuning stub width
*L*_stub	1.6[mm]	Tuning stub length
*W*_sub	9[mm]	Substrate width
*L*_sub	9[mm]	Substrate length

Tab. 1: Parameters of microstrip patch antenna [8]

Feeding a patch antenna from the edge leads to a very high input impedance, causing an undesirable impedance mismatch if a conventional 50 Ω line is directly connected. One solution to this problem is to use a matching network of two quarter-wave transformers between the feed point of the 50 Ω line and the patch. An optimum feed point exists between the center and the edge. The length of the microstrip line, *L*, is chosen to minimize the reflected power, S_{11} [8].

We decided to use this type of antenna (with parameters shown in Tab. 1) to model and to analyze the properties of biocompatibility material PPMA in detail, Fig. 4.
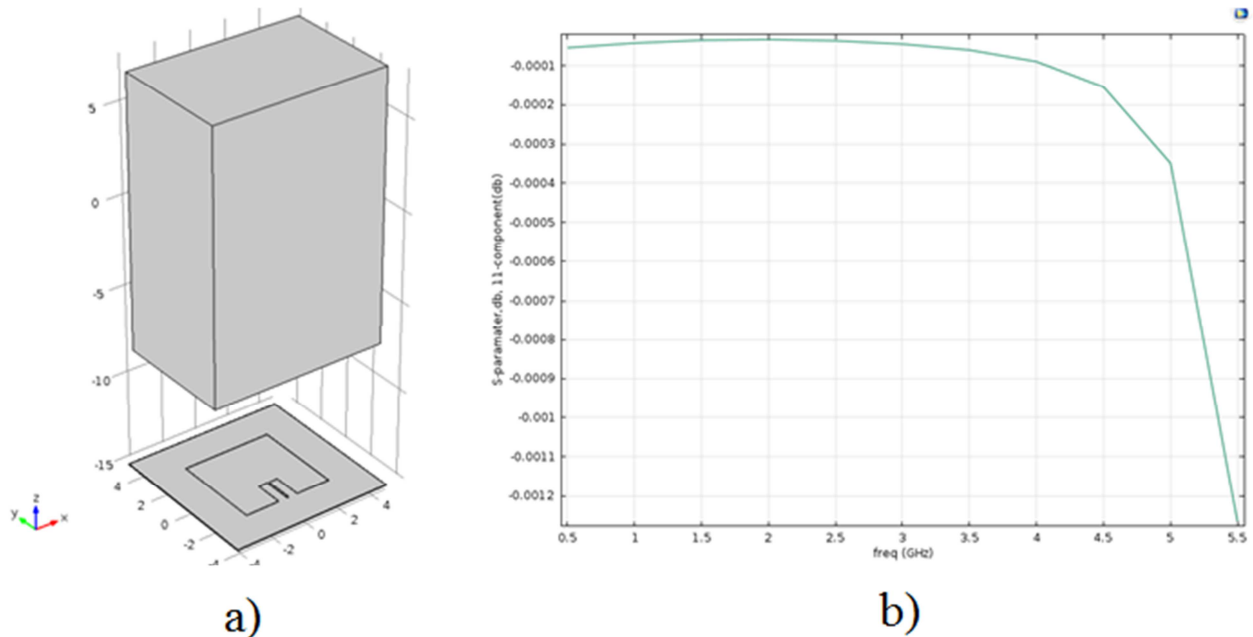
Fig. 4: a) created 3D geometry of patch antenna and PMMA in free space, b) S_{11}-parameter of PMMA dependent on antenna's frequency range 0.5-5.0GHz

In first step, we analyzed the homogeneities of sample and S_{11}-parameter.The parameter is the reflection coefficient of EM wave. This type of analysis can show that the GHz frequencies can be used to detect the presence and the composition material. The primary analyze (shown on Fig. 4), which gives us information about interaction between material and antenna. S_{11}-parameter (of antenna and PMMA inserted in free space) decreases. This decrement is caused by frequency range of used antenna and parameters of microstrip patch antenna. These results are going to be used as calibration for measurement. In the next step, we are going to add inhomogeneities to the sample, i.e. defects.

4. Conclusion

Our aim was to measure, to model and to analyze the properties of selected dental material PMMA. In experimental work, we focused on investigation of dental material as relative permittivity also loss factor. We calculated relative permittivity $\varepsilon_r = 9.5$ and also loss factor $\mathrm{tg}\delta_e = 0.012$ of PMMA. These measured dielectric parameters are important for MNDT of material.

In second part of this articel was concentrated on investigation of scattering parameters S_{11}, which gives us the information about EM wave reflection form structure of biomaterial. To compare change S-parameter can be deduce that the sample is homogenous or inhomogeneities. The changes of scattering parameter-S_{11} amplitude are very important in the MNDT examination of investigated dielectric sample homogeneity.

Acknowledgement

References

[1] POZAR, DAVID M. *Microwave engineering.* s.l. : John Wiley & Sons, 2012. ISBN 978-0-470-63155-3.

[2] *http://www.ndt-ed.org/AboutNDT/aboutndt.htm.* [Online] 2001-2014. [Date: 24. March 2014.].

[3] BANSAL, RAJEEV (ed.). *Handbook of engineering electromagnetics.* New York : CRC Press, 2005. ISBN 0-203-02602-0.

[4] OMAR, MOHAMMAD**.** *Nondestructive Testing Methods and New Applications.* Croatia : Intechweb.org, 2012. ISBN 978-953-51-0108-6.

[5] FAKTOROVÁ, D. *Základy mikrovlnných meraní,* EDIS – vydavateľstvo Žilinskej univerzity, 2014. Žilina

[6] *http://www.antenna-theory.com/antennas/patches/antenna.php.* [Online] 2011-2015. [Date: 20. January 2015.].

[7] RAJYAGURU, VYOMA; TOGADIYA, VIJAY. *A Design of Rectangular Linear Polarized Microstrip Patch Antenna at 1 GHZ.* May 2014. pp 494-496 ISSN (Online): 2319-7064

[8] http://www.comsol.com/model/download/198073/models.rf.microstrip_patch_antenna_inset.pdf. [Online] 2015. [Date: 20. January 2015.].

Oscillations and quality parameters of electricity in power systems caused by dispersed sources of energy

[*]Michał SALWA

[*]Kielce University of Technology, Faculty of Electrical Engineering, Automatic Control and Computer Science, Department of Industrial Electrical Engineering and Automatic Control, Division of Power Engineering Fundamentals**,** al. Tysiąclecia Państwa Polskiego 7, 25-314 Kielce, Poland, msalwa@tu.kielce.pl

Abstract. Fallowing article try to describe influence of dispersed sources and power oscillations caused by them. Analysis was based on simulation created in Simulink of Matlab program. Implemented data in this simulation was gathered and based on actual layout of power system consisted of 110 and 15kV power line where dispersed power sources was connected. In the article focus on oscillation caused by working source and mutual relationship of them.

Keywords: Dispersed power sources, power lines, interference, simulations.

1. Introduction

Dispersed sources in its concept includes an extremely wide range of objects that generate both electricity and heat. In Poland, the source of power from 1W to 150MW is classified as a dispersed power source. Development of renewable energy has become, in recent years, a large and ever-increasing development of production capacity. The largest objects are now able to produce approx. 120MW of power, however, despite the significant parameters of these systems are still in the concept of distributed power generation. As a result the vast majority of the objects of renewable energy sources is classified as an object of distributed energy. [2]

As follows from official statistics, the main component of which is based on renewable energy is wind. According to the data for the year 2014 the share of energy produced by wind farms compared to the energy produced by the distributed energy systems ranks at approx. 60% in Poland and 40% in Europe. The next in the order of Facilities are biomass and hydroelectric power plants (approx. 20% in Poland and 25% in Europe) and solar systems (about 1% in Poland and 15% in Europe). Currently, a large role is given to systems aimed at protecting the environment, through which were introduced directive mandating an increase in the proportion of energy generated from renewable energy facilities in relation to the energy obtained by conventional methods. Current share of "clean energy" in the system is estimated at 12% in Poland and 20% in Europe compared to other forms of energy, such as nuclear power, conventional ect. [3]

Dispersed sources like all generating units are characterized by energy dependence relative to the raw material which are based on his work. For these reasons, the performance characteristics of distributed sources based on renewable sources can be irregular and unstable. An additional element may also be unpredictable work and generation of these sources due to the inability to accurately forecast the strength and direction of wind or sun exposure of a given area during a time interval. Connection to the distribution or transmission lines may thus lead to disruptions caused by the work of these sources and affect the quality of electricity transmitted through them.

2. Oscillations and interferences

2.1. Theoretical assumption of impose interferences caused by dispersed sources

Based on previous research, we can conclude that the work of dispersed power sources is associated with dampened harmonic oscillations, related with the effect of pushing power between the network and the source that lead to establishment of new power levels in local power system [1]. Examining the nature of the oscillations can be assumed sinusoidal oscillations of decreasing amplitude. For a system with multiple distributed sources so we can assume that the objects and their interference may impose one another according to the definition of interference:

$$U(x,t) = A\sin(\omega t + \varphi_1) + A\sin(\omega t + \varphi_2)$$

$$\varphi_1 = \frac{d_1}{\lambda}; \varphi_2 = \frac{d_2}{\lambda} \qquad . \qquad (1)$$

According to the definition (1), interference with the same wavelength λ and spaced length d, subject to the application. Assuming that the oscillations caused by the work of dispersed sources are subject to interference, we can presume to say that depending on the distance between the two objects, we can obtain:

1. no interference when the oscillations are consistent with values will be the opposite and soundproofing.

$$\varphi_1 - \varphi_2 = (2k+1)\pi :$$
$$U(x,t) = 0 \qquad . \qquad (2)$$

2. Interference impose, reaching the value of the amplitude of the sum of their values:

$$\varphi_1 - \varphi_2 = 2k\pi :$$
$$U(x,t) = 2A\sin(\omega t) \qquad . \qquad (3)$$

3. Interferences will be a complex function of functions of the interference of various sources.

Then analyzing the oscillations in the system of distribution lines, a significant is the point of measurement and distance of objects relative to the generator, whereby it is possible to assume that the measurements on the effect of the distributed generation upon power system can be drastically different from each other and dependent on the operating conditions at the time of measurement. Moreover distance from the source of interference is the only significant difference, because in power grin oscillations generated by generator have the same wave length and frequency.

2.2. Computer simulations based on real power grid

In order to examine the interference resulting from the distributed source operation, performed simulation of power grid consisting of a 110kV line with a length of 50km stretched between two substation to which a second 110 kV line is drawn parallel with the attached dispersed source in the form of a wind farm of power of 80MW (Fig. 1 .). The system also simulates the additional 15kV lines radiating from two connected distribution substations 110 / 15kV, the core of which is joined to 4 additional wind farms with a capacity of 2 MW and one wind farm with a capacity of 900kW.
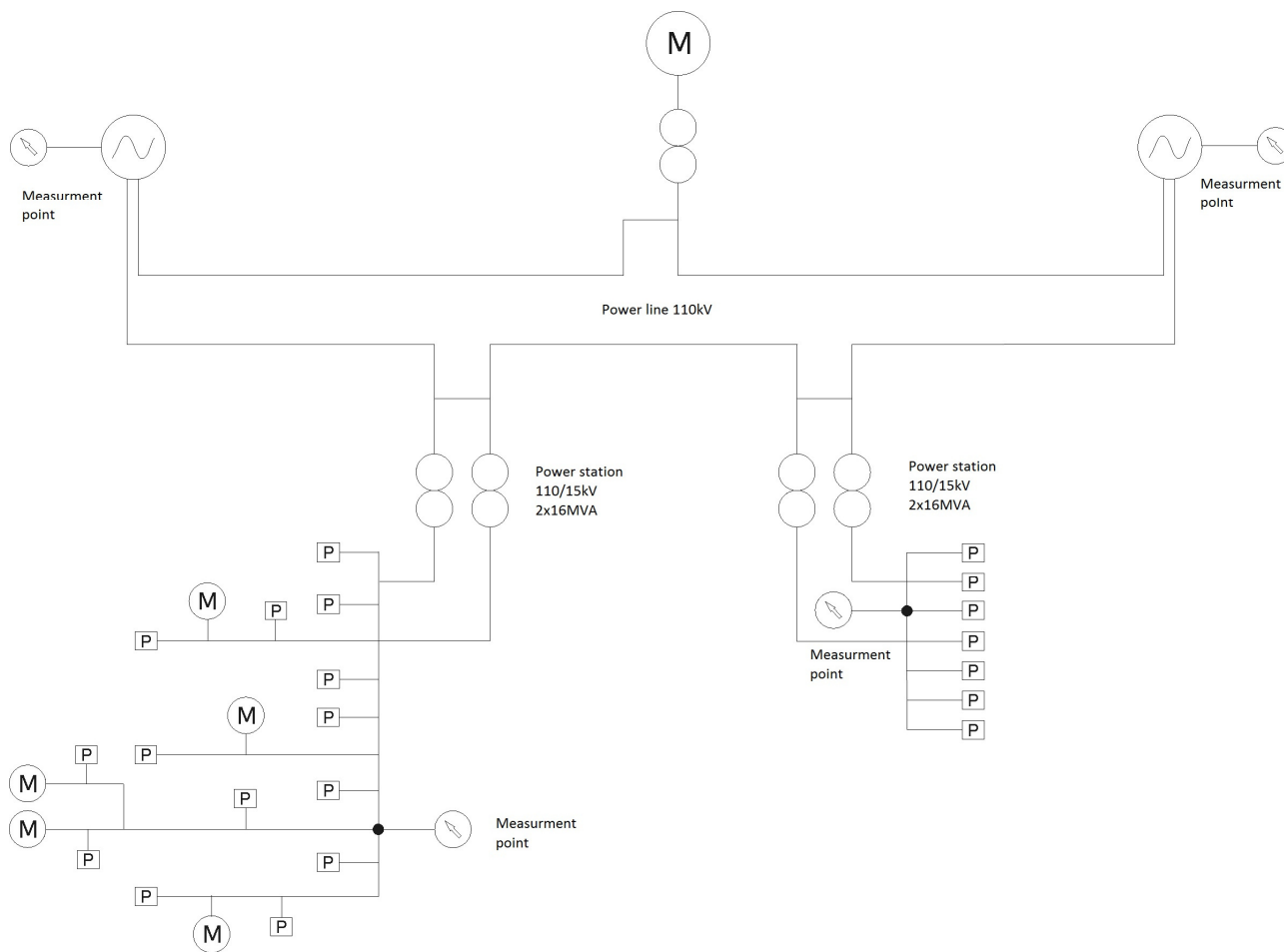
Fig. 1. Schematics of simulated power grid. M - power generator of distributed source. P - Power input

Technical data entered into the system is based on the actual technical parameters of the power line acquired from the energy region for the possible most faithful simulation of phenomena of interference resulting from the operation of dispersed power source.

The first was carried out simulations of individual sources and their individual influence on the current and voltage levels of electricity transmitted through distribution lines. In order to facilitate comparison of the impact of interference measurement systems established at one point, that was set at the point of exit switchgear 15 kV line for reasons of metering and protection systems of this line installed at this point. Waveform (Fig. 2) voltage oscillations were observed with comparable values and amplitude of approx. 60V and current oscillations with amplitudes approx. 20A in the case of a power source for 900kW and 30A for 2MW source.

Interference waveforms show the expected damping characteristics, providing for the seeking to establish new voltage levels, but the damping factor appears to be small, which may be indicative of a long period of time required to determine the levels and loss of oscillation in the simulated system

Next, simulations were carried out when attached are two sources to the grid and results were compared. The simulation consisted of switching on sources in time of another (switching the second source 1s time from the start of simulation, when the first started at time point of 0,5s), allowing for a more accurate analysis of the effect caused by the overlapping of interferences caused by work of dispersed sources. The resulting waveforms show the effect of the imposition of the oscillation as defined sinusoidal interference signals (Fig. 3) and generate a interference in a form of a complex function.
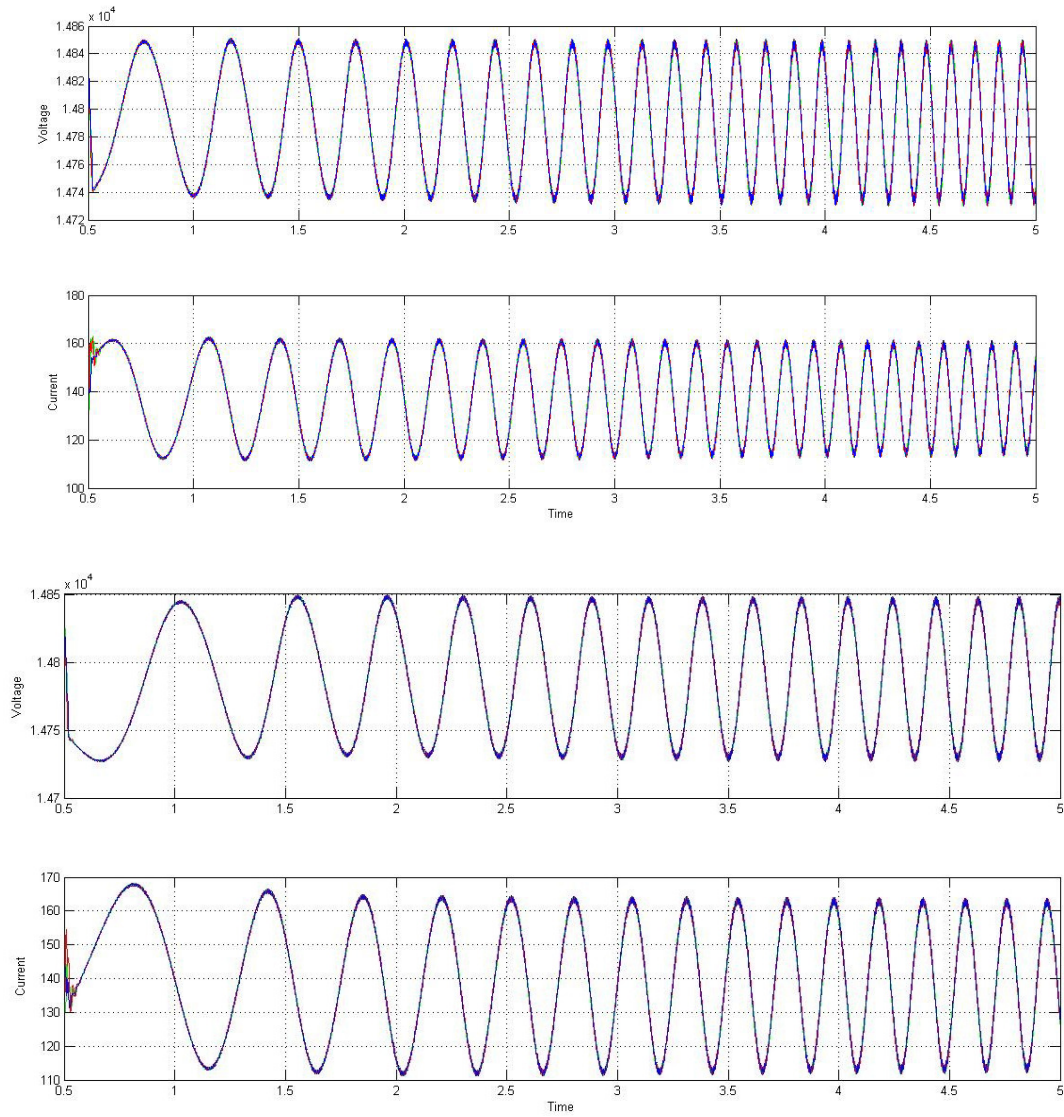
Fig. 2. Oscilation caused by addition of distributed generation into power grid. On top source of power 900kW, below of power 2MW.
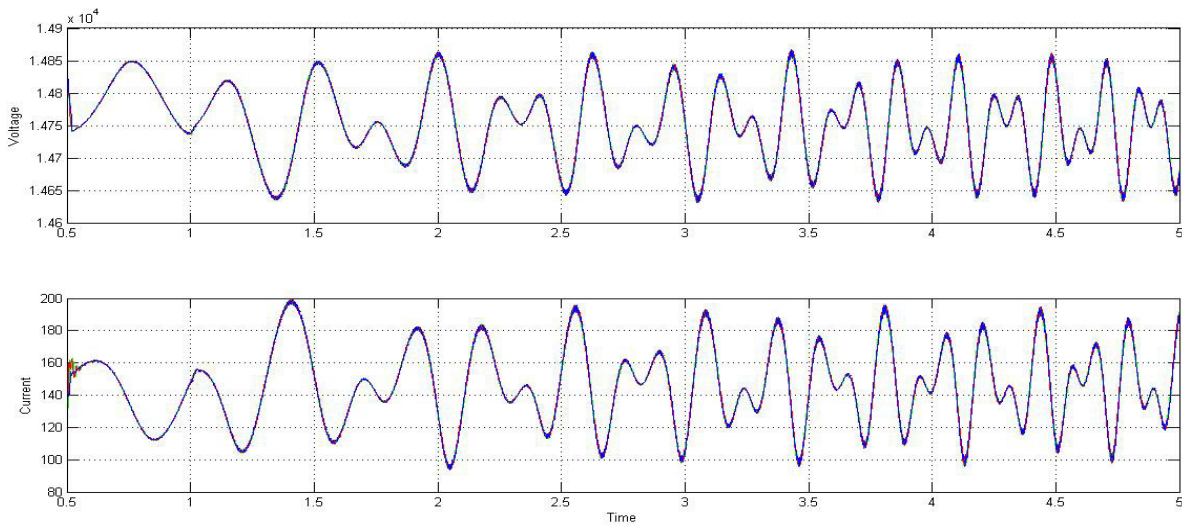
Fig. 3. Interference of distortion in power grid caused by two working dispersed power source of power 900kW and 2MW simultaneously.

According to the definition of interference distortions were summed up, not only changing the characteristics of the waveforms, but as well increasing the potency of interference. The amplitude of oscillations as observed reached voltage values of 100V and 50A of current at presented waveform.

In addition, interference was observed in the other measuring points of the simulation system despite of energy transformations to different voltage levels. Interference in point of main distribution station reached amplitude of 30V at voltage waveform and 4A at current waveforms, and on and point of the second distribution station, where there are no source plugged in, the amplitude of the voltage reached 5V and 0.1A on current waveform.

3. Conclusion

Analysis of interference indicates multiple adverse factors affecting the operation of the power system, resulting from the connection of distributed sources of unstable work, that are also categorized as objects of renewable energy source. Interference may indicate major disruptions extremely hard to compensate arising from the imposition made from of all the oscillations of individual sources.

Another problem is the low damping ratio and a long time to establish the new power levels, which can show independence of interferences from the governing system regulating the source connection to the network, for reasons that noise after a predetermined time should be comparable to direct and sudden application of the source to the network due to interference of this source in the line.

The last can be propagation of distortions in the power system and their mapping in remote locations in substantially distant points from the point of attachment of power source. Oscillations appear in the system despite two voltage transformations from 15kV to 110kV and 15kV again. Amplitude showed no great value, but it should be noted that interferences came from only two power sources with a total power of 3 MW, which currently may be taken as a single power connection of wind tower.

The first results show the possible risks and require further studies to determine the extent of the difficulties arising from the exploitation of objects of distributed sources and possible measures to optimize and eliminate the adverse impacts on the power network and users connected to it. In addition, it is planned to complete the simulation and analysis of systems by inverter systems used in distributed power generation facilities and its impact on THD parameter at a predetermined power network.

References

[1] M. Salwa, S. Filipiak: ″Analiza wpływu lokalnego źródła energii na planowanie pracy elektroenergetycznej sieci rozdzielczej na wybranym przykładzie″, Logistyka 4/2014 (lipiec-sierpień).

[2] The collectiv work: Poradnik Inżyniera Elektryka tom 3, Wydawnictwo Naukowo-Techniczne,Warszawa 2005

[3] Raports of Urząd Regulacji Energetyki, "Odnawialne źródła energii", www.ure.gov.pl

Types of non-destructive testing by eddy current method

[*]Andrea Stubendekova

[*]University of Zilina, Faculty of Electrical Engineering, Department of Electromagnetic and Biomedical Engineering, Univerzitna 1, 01026 Zilina, Slovakia, {andrea.stubendekova}@fel.uniza.sk

Abstract. This article deals with two types of non-destructive testing by eddy current. Basis of standard eddy current method is a movement of the probe over an investigated material. Technique of swept frequency is a further possibility of using this method. Its principle is based on the change of frequencies in a wide range while the probe is in a fixed position. An inspected object is a plate made of austenitic steel with three different notches. The both experiments are performed by eddy current air probe. Lock in amplifier is the measured equipment used in these experiments. This study compares the results and advantages of both methods.

Keywords: eddy current testing, swept frequency, air probe, experiments

1. Introduction

It is well known that Eddy Current Testing (ECT) is frequently and successfully used method for assessment of the status of various conductive objects. The conclusion about a present or an absence of the defect can be determined from the result signal obtained during the movement of the probe over the inspected material. Currently, in modern technique, there is a requirement of the continuous and long-term monitoring of estimated product. Technique swept frequency is ones of possibilities which meets this requirement. It uses the fixated positioning of the investigative probe and the generating of frequencies from a wide range.

This article provides the results of experiments whereby it compares the two mentioned methods. The each has its advantages and a choice ones of them depends on the various factors.

2. Non-destructive testing by eddy current

The term – non-destructive testing means the evaluation of object without changing and damaging it. The principle of the eddy current method concerns the discovery of electromagnetic induction and it is displayed in Fig. 1, [1], [2].

In brief, alternating current passing through the coil causes the electromagnetic field around it. The orientation of magnetic fields is changed with the each cycle of said current. If an electrically conductive object is situated close in this field, it causes an induction of electromagnetic field in it. Ultimately, if a material of the object has certain definite electrical resistance it creates flow of the current. These currents are in closed paths like whirlpools. This is reason why they are known as the eddy currents. This flow in an estimated material is influenced by material properties, in the concrete magnetic permeability μ, electrical conductivity γ, but also the excitation frequency, the presence of notches in the object and its dimensions. Very low conductivity of the material results the absence of induced electromagnetic field and thus the eddy currents. The present of a defect in material causes the change in coil impedance or induced voltage during the ECT, [2], [3], [4], [5].

In the case of technique swept frequency is necessary to gather the response of eddy currents. The probe is situated in a fixed position and a frequency is changed in a wide range. This technique

provides the results demonstrated of success in detection and it is suitable to use in areas where scanning over a surface of material is not possible, [6].
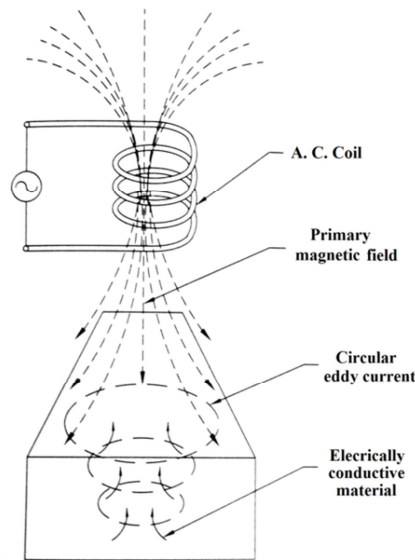
Fig. 1 Principle of eddy current testing, [2]

3. Creation of experiments

The both experiments are performed by LOCK-in amplifier and the same input parameters are used – amplitude is 2 Vpp, sensitivity is 500mV and time constant is 50ms. The same estimated object is used in both methods. Namely, it is plate made of austenitic steel SUS316L, which contains three defects. They have the different depth d_d = 1, 5 and 9 mm, but their length and width are the same in all cases. The dimensions of investigated plate are displayed in Fig. 2. The measurements are realized by air ECT probe, which contains from exciting Tx and receiving Rx coil. The outside diameter of the coil is the same $dTxout = dRxout$ = 2.8 mm and the height of coils is v = 2 mm. The inside diameter of the exciting coil is $dTxin$ = 1.8 mm and the receiving coil is $dRxin$ = 1.4 mm.
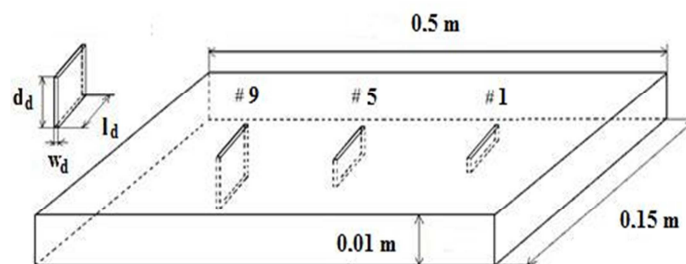
Fig. 2 Dimensions of investigated object

The experiments by swept frequency eddy current technique are carried out at first. The investigative probe is located over the material perpendicular to the individual defects of the inspected material and the frequency is changed in a range $f \in$ <640 kHz, 760 kHz>. The same frequency range is used in three said measurements. Real and imaginary element of the magnetic flux density B is obtained in all cases. B_{mod} is module of magnetic flux density and the following expression can be used:

$$B_{\mathrm{mod}} = \sqrt{\mathrm{Re}\{B_z\}^2 + \mathrm{Im}\{B_z\}^2} \ . \tag{1}$$

The result graph is created by three signals – detection 1, 5, 9 mm deep defect, severally.

After the experiments based on the standard ECT are performed. The process is same to the previous case. The values of elements of magnetic flux density are obtained from the three mentioned options and the three signals are acquired. Now, only one frequency $f = 1$MHz is used in contrast to the previous measurement. In this case the probe is not fixed in one position but it moves over the material in range <-10mm, 10mm>. The position "0" represents the centre of defect.

4. Results

The results obtained of standard eddy current method and ECT based on swept frequency are compared. The deepest defect $d_d = 9$ mm provides the biggest deflection in these cases. It can be stated that the both methods are able to detect of all investigated defects.

The signals of eddy current method based on swept frequency are shown in Fig. 3. The graph displays the dependence of the voltage output of magnetic sensor and frequency in the range $f \in$ <640 kHz, 760 kHz>.
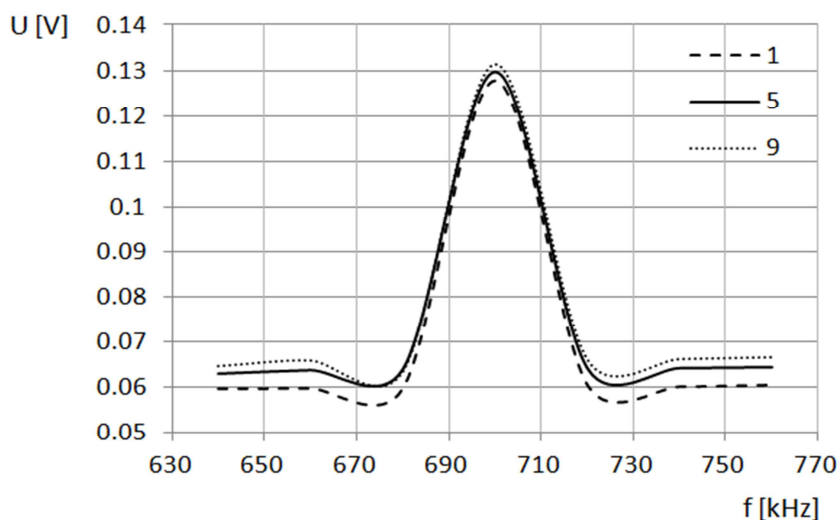
Fig. 3 Results of ECT based on swept frequency

Standard eddy current method provides the results shown in Fig. 4. The graph displays the dependence of the voltage output of magnetic sensor and probe position at a frequency $f = 1$ MHz.
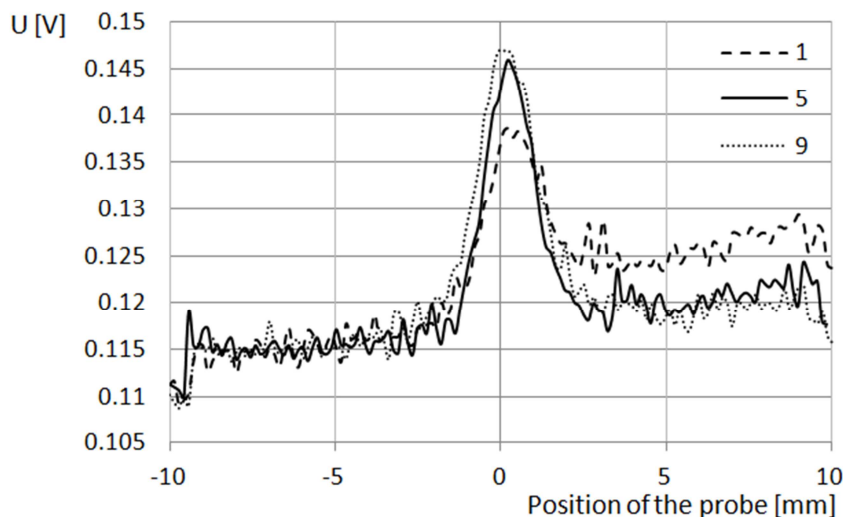
Fig. 4 Results of standard ECT

The differences between individual signals are bigger as the previous case. The distortions of signals are caused by surrounding noise.

Dependence between magnetic flux density B and induced voltage u_i is expressed by the following equation:

$$u_i = -\frac{\partial \Phi}{\partial t} = -\frac{\partial(\vec{B} * \vec{S})}{\partial t}.$$

(2)

5. Conclusion

Eddy current method is often used because it provides very good results in field of non-destructive testing. Two types of eddy current method were compared in this article according to experiments and theoretical knowledges. Results of these methods showed the success of both methods. They were able to detect of defects with various depths and displayed the differences between them.

The each of them has advantages. The standard ECT is better to use if it is necessary to obtain of information about the presence or absence defect. The eddy current method based on swept frequency is more advantageous if a long-term and continuous monitoring is required and in the case where a scanning over a surface of investigated object is not possible.

Therefore, the both methods can be used to detection and a choice depends on reason of the detection.

References

[1] *NDT Method Summary.* [online], [2015/04/13], http://www.ndt-ed.org/GeneralResources/MethodSummary/MethodSummary.htm

[2] Rao B. P. C. *Practical eddy current testing.* Alpha Science International Limited, 2007. ISBN: 978-1-84265-299-2

[3] Kreidl M., Smid R. *Technical diagnostics (in Czech)*, BEN, Prague, 2006. IBSN 80-7300-158-6

[4] Janousek L., et al. *Progress in eddy-current non-destructive evaluation of conductive materials.* Acta technica ČSAV 55.1 (2010): p. 13-28.

[5] Chudacik V., Janousek L., Smetana M., Strapacova T. *Impact of selected defect parameters on 3D eddy current testing response signals.* In ELEKTRO 2014: proceedings. [CD-ROM]. Žilina: IEEE, 2014, p. 558-561. ISBN 978-1-4799-3720-2

[6] Strapacova T., Capova K., Janousek L., Smetana M., *Defect Identification using Eddy Current Sweep Frequency Technique,* Studies in Applied Electromagnetics and Mechanics, Vol. 36, Electromagnetic Nondestructive Evaluation (XV), 2012, ISBN 978-1-60750-967-7, p. 264-269.

Petersen coil for a model of a 22 kV distribution line.

[*]Filip Suško, [*]Martina Látková
[*]University of Žilina, Faculty of Electrical Engineering, Department of Power Electrical Systems,
Univerzitná 1, 01026 Žilina, Slovakia, {Filip.Susko, Martina.Latkova}@fel.uniza.sk

Abstract. This paper deals with the layout of the Petersen coil for a model of 22 kV power line. It contains a dimension's layout of the coil, a verification of the coil parameters by simulations in two different simulation platforms as well as a design of a circuit and an explanation of algorithm used to tune the coil. There are also presented various tuning algorithms that are used in real operation in the paper, as well.

Keywords: Petersen coil, distribution line, simulation, algorithm, compensation, logic.

1. Introduction

Nowadays, it is very important to operate distribution lines without unnecessary cut offs and therefore it is necessary to ensure that they can operate during fault if there is no possibility of a destruction of technological devices, or there is no threat to the health and life. Neutral grounding through a Petersen coil recommended by standards leads to capacitive current compensation at fault locations in medium voltage networks that provides conditions for self-quenching of arc and, in some cases, for overvoltage limitation. However, the danger of high overvoltages is not eliminated as in case of arcing ground faults under open-phase conditions which happen at nonsimultaneous operation or high voltage circuit breaker pole failures. The possibility of continuous overcompensation more than 5-10% often exists in practice [1]. To avoid this, high-value resistors are recommended to be connected to a neutral in parallel with a Petersen coil. Many organizations operating 6-35 kV networks have chosen this method of neutral grounding. Connecting a neutral to the ground through a Petersen coil in parallel with a resistor results in reducing of free oscillations, a suppression of beats and voltage reduction on the faulted phase. Overvoltage limitation at arcing ground faults leads to reducing of the number of insulation flashovers and the total number of faults. Almost full reduction of transitions of arcing ground faults to double-phase faults (i.e. short circuits) is observed [2].

One of the tools, which allow operation at 22 kV power line during an earth fault, is the Petersen coil. It is a device that owing to the possibility of inductance changes can compensate a fault current and thus enables the operation of the power lines also during the contact of the phase conductor to the ground. The operating principle is based on a compensation of the capacitive fault current using the coil, which allows us to operate distribution network even during the fault. The fault can be caused by many reasons. Some of them can be eliminated be a preventive maintenance, e.g. by cutting off trees around power lines. However, there are still factors that are difficult to predict.

The tuning system used in analog tuning automatics (type AL-2) was adversely affected by various external factors. Moreover, the coil voltage varies even when a network capacitive current remains constant, because of slight changes in network's asymmetry, e.g. by movement of the conductors in the wind [3]. A substantial progress has been made in tuning algorithms of Petersen coil due to computer technology development. Recently developed tuning algorithms are able to cope with problems that used to negatively influence the process of coil's optimal tuning.

2. The coil layout

To design a Petersen coil model for 22 kV power line model, it was necessary to define a required value of the coil's inductance, which is given by the largeness of the simulated network (the sum of the lengths of the individual model modules). Knowing this, it was easy to define a minimum and maximum value of coil inductance. The layout itself consisted of defining the dimensions of the coil taking into account the required inductance value. After determination of these values, it was necessary to choose the appropriate size of the varnished copper wire. In the next step, it was essential to calculate the required number of turns, from which we also identified other values, e.g. a number of turns per layer, a number of layers and a height of the entire winding. Then an inductance of the coil without core was determined. In our case, the minimum inductance was satisfying. To determine the maximum inductance of the coil with a core, it was necessary to create a mathematical model, which was then used in a finite element method calculations.
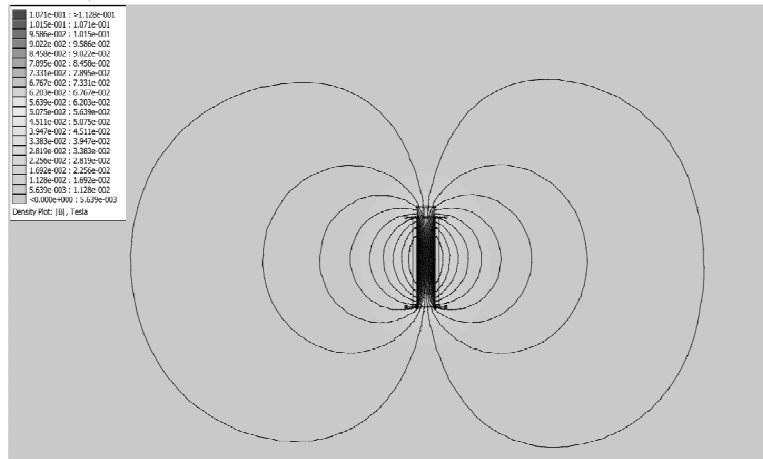
Fig. 1. The flux density in and around the coil with inserted core.

We found out from the calculated value that the maximum inductance is not sufficient, and therefore it was necessary to change the dimensions of the coil. We increased the height of the coil and recalculated inductance of the coil without core. As the inductance of the coil without core was satisfactory, we proceed to designing the model with new adjusted values. In this case, coil inductance with the core determined by the finite element method appeared satisfactory. Consequently, it was necessary to verify how ejecting of the core changes the value of inductance, because it was essential to achieve the lift of the core in centimeters in order to get simple coil's structure. If the inductance dependence on air gap changes was too strong, the required positioning accuracy of the core would place the extreme drive mechanism claims and its implementation would be technically and economically unrealistic. The height of the coil could theoretically be significantly reduced, but in such a case the required air gap would have dimensions of millimeters (using EI sheets micrometers), which is impractical.
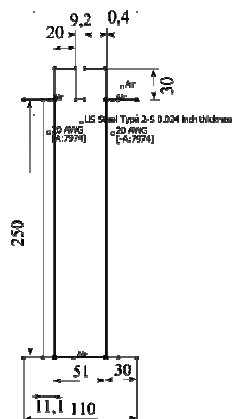
Fig. 2. The coil dimensions.

It has been verified, by a finite element method, that the inductance curve dependence on the extension of the core is satisfying and thus it was possible to proceed to the design of an automatic tuning of the coil.

Since the inductance value determined by finite element method in the program FEMM 4.2 had to be verified, we proceed to design of the model in Opera. 2D and 3D analysis can be done in this program, unlike FEMM 4.2, where only 2D analysis is possible. Due to the validation of the coil model in Opera we found out that the minimum value, i.e. the value of the coil without the core, was slightly different. The maximum value was higher, which in this case did not present any problem, because it satisfied the condition of maximum inductance being required to compensate the earth fault at the smallest largeness of modeled network. Only the step for shifting the core was changed to lower value.
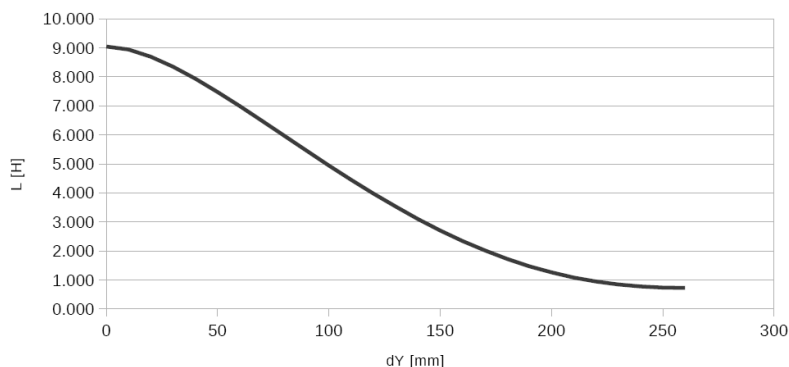
Fig. 3. The inductance changes due to the extension of the core.

3. Selection of tuning algorithm for the coil

There are several algorithms for tuning Petersen coil. The first is the tuning to the maximum voltage U_{NE}. Another currently used method is the tuning with voltage phasor measurement principle and the third is the tuning on the principle of equation for U_{NE} [3].

Fig. 4. Tuning based on a maximum voltage U_{NE} [3].

Fig. 5. Tuning based on a principle of the voltage phasor measurement [3].

In our case, we used the first method of tuning, because it was simple for an implementation in our model and the reasons, which stopped its use in a real operation are not applicable in our model of 22 kV power line. Its main disadvantages was that the voltage U_{NE} varied even in a state when the network capacitive current remains constant, due to slight changes of asymmetry in the network, e.g. by movement of conductors in wind. But this factor does not occur in our model of power line, which spoke in favor of using this tuning.

3.1 Circuit design for tuning algorithm

While designing the control circuit, we put the emphasis on the possibility of changes in the logic of the tuning and therefore an ATMEGA microcontroller was used as a main circuit component. With this feature it is possible to make some changes in the source code in order to optimize the tuning process.

The terminals 3 and 4 of SV1 connector are grounded (Fig. 6) and without voltage during normal operation (without fault), which ensures that the connected motor's drive is standing. In the case of failure, a voltage appears at the terminal 2 of the connector SV1 and the logic circuit instructs to handle the core. The core is being shifted for 100 ms and after it a new value of the node voltage of the transformer is recorded. So the value of the voltage before and after the shift of the core is obtained. These two values are compared by the logic and provided that the new value over an originally one was increased, this means the logic was right and there is a further shift of the core. In this way, the control algorithm continues to the state, when the maximum voltage in the node is reached. During this a situation may appear, when the value before and after the shift of the core could be the same. In this case, the logic takes this situation as increasing and core is shifted again. The value after the shift, which was the same as before, will be marked as T1, core is again shifted, but if there was then a case of decreasing voltage, this value labeled as T2 causes a shift of the core back in two steps. Doing this it is possible to shift the core in and out on the top area and thus maintain a good tuning. The advantage is provision of a state, in which, if the core is partially retracted, but it will be in the area of decreasing voltage, logic of the circuit shifts the core, compares and then makes a shift in the opposite direction but two steps back. Shift time can be increased, but at too great times there is less accuracy of finding the top of the curve presented in Fig. 4.

Fig. 6. Control circuit scheme.

Depending on whether there is ejecting or inserting of the core, either one or the other relay is switched. When the relay K1 will be switched on, there is +U at the terminal 3 of the connector SV1 and -U at the terminal 4. If logic requires the opposite direction of core shifting, relay K2 will be switched on and thus + U appears at the terminal 4 and –U at the terminal 3. Through this reversing of voltage polarity at the motor terminals a change of its rotation is achieved. The circuit permanently carries out the conversion of measured voltage to a digital value, which connected to terminal 2. It can operate with a voltage value of about 5 V with an accuracy of 0.004 V.

4. Conclusion

Designed Petersen coil is primarily intended to compensate for the single-phase earth fault in the model of 22 kV power line, but it can be also used in many other applications, such as for education or to illustrate the operation of the device. Since the control circuit is composed of a microcontroller, algorithm can be modified and adjusted at any time or it is possible to used other specially defined algorithm. Since it is possible to make changes to the algorithm, this circuit offers the possibilities to improve tuning using newer methods and thus increase the efficiency of the device itself.

Acknowledgement

References

[1] F. A. Likhachev, "Ground faults in ungrounded and resonant grounded networks". Moscow: Energiya, 1971.

[2] L. I. Sarin, A. I. Shirkovets, M. V. Ilinykh, "Field experience of resistance neutral grounding in 6-35 kV networks", Energetik, vol. 4, pp. 13-14, 2009.

[3] HORÁK M., Systémy chránenia a automatizácie distribučných elektrických sietí 22 kV, PRO s.r.o. Banská Bystrica, ISBN 978-80-89057-37-5.

[4] McDonald J.D., Electric Power Substations Engineering, CRC Press, ISBN 0-8493-7383-2.

[5] Harlow J.H., Electric Power Transformer Engineering, CRC Press, ISBN 0-8493-9186-5.

[6] Brenna, M. ; De Berardinis, E. ; Delli Carpini, L. ; Paulon, P. ; Petroni, P. ; Sapienza, G. ; Scrosati, G. ; Zaninelli, D., Petersen Coil Regulators Analysis Using a Real-Time Digital Simulator, Power Delivery, IEEE Transactions on, Volume: 26 , Issue: 3, DOI: 10.1109/TPWRD.2010.2097611, Publication Year: 2011 , Page(s): 1479 – 1488, ISSN 0885-8977.

Design and Testing of an Injection Transformer for a Dynamic Voltage Restorer (DVR)

*Dominik Szabó, *Juraj Altus
*University of Žilina, Faculty of Electrical Engineering, Department of Power Electrical Systems, Univerzitná 2, 01026 Žilina, Slovakia, {Dominik.Szabo, Juraj.Altus}@fel.uniza.sk

Abstract. The paper deals with a scaled model of a dynamic voltage restorer implemented in laboratory environment and it is focused on a series-connected injection transformer. A simplified design of the transformer and transformer tests are presented. The obtained results are further compared with simulation calculation.

Keywords: injection transformer, DVR, voltage sag, compensation, FACTS, power quality.

1. Introduction

The most severe power quality problems are voltage sags, swells, interruptions, harmonics and flickers. Failures due to such disturbances cause a huge impact on production cost. Especially, modern industrial equipment is more susceptible to power quality problems. They are, for example, computers or other electronics damage, lights dim and flickers, loss of synchronization of processing equipment, motors or other process equipment malfunctions, transformers and cables overheating, problems with power factor correction equipment, noise interference to telecommunication lines and many more [1].

A voltage sag means that the required energy is not being delivered to the load and this can have serious consequences depending on the type of load involved.

One of the possibilities for power quality and system stability improvement is to introduce FACTS devices. FACTS controllers are able to control and regulate one or more key parameters, such as current, voltage, active, reactive power, frequency or phase angle. According to [2], FACTS can be divided into four basic types – series connected, shunt connected, combined series-series and combined series-shunt controllers. The main disadvantage of implementing FACTS is a very high price of these devices and economic requirements.

1.1. Dynamic Voltage Restorer

Dynamic Voltage Restorer (DVR) belongs to series connected FACTS controllers. The primary function of a DVR is to compensate voltage sags and swells, but it can also perform tasks such as harmonics elimination, reduction of voltage transients and fault current limitation [3]. DVR is usually installed between a source and a critical load that should be protected. Even the shortest voltage sag can cause serious equipment damage, interruption of production cycles and financial losses. In general, a DVR consists of three parts (Fig. 1.):
- measuring unit,
- control unit,
- power circuit.

The measuring unit provides voltage and current measurements. The outputs are voltage and current analog signals (u, i), which enter the control unit. The control unit converts these signals to their digital representation using A/D converter so that they can be processed by a microcontroller or a DSP – digital signal processor. The next part is a voltage sags detection algorithm followed by a calculation of the compensating voltage U_{com}, which is the voltage needed to be injected into the

system in order to maintain the load side voltage in rated values. The power section consists of a voltage source converter (VSC) equipped with a LC filter to smooth the output voltage, a DC energy storage and an injection transformer (TR) – booster.

The basic principle of DVR function is to inject or draw the compensating voltage U_{inj} to or from the supply voltage U_s in order to mitigate voltage sags or swells on the load side U_{load}. At every moment the control algorithm compares desired voltage and actual measured voltage. The difference between these two signals is considered as a compensating voltage U_{com} (control) and U_{inj} (power circuit). U_{com} is a digital input for a pulse width modulation (PWM) to control the voltage source converter. The VSC converts DC energy stored in an energy storage device (such as power supply, batteries or supercapacitors) to inject AC voltage that is to be superimposed to the source voltage using a transformer. DVR power output depends on the amount of energy that can be stored in the energy storage unit.
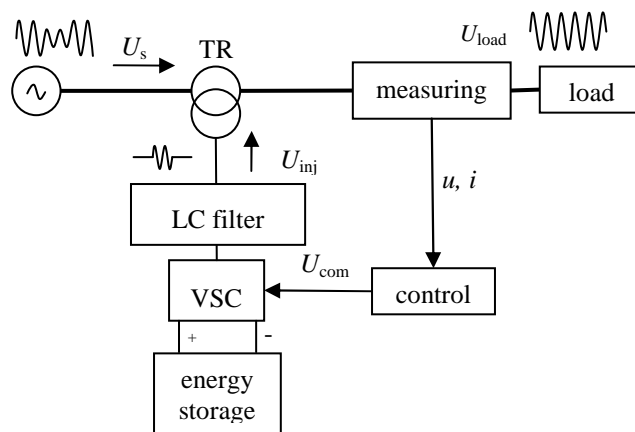

Fig. 1. Simplified scheme of a DVR

DVRs are usually installed to protect large consumers with the sensitive technologies and devices (2 MVA or more) connected at distribution level [4]. This paper describes a DVR scaled model designed and implemented in laboratory environment. The DVR is a single-phase model, it is designed for 22 kV (medium voltage) power line model and its parameters are: rated load voltage 127 V, current 1 A, power 127 VA and frequency 50 Hz. The DC voltage of the energy storage is 48 V. The DVR model is able to compensate sags with the maximum depth 77 % of rated voltage.

2. Injection Transformer

The injection transformer is connected in series with the line. When a sag occurs the injected voltage is added to the source voltage through the transformer. The operation of DVR has an impact on the phase shift and voltage drop, which depend on the transformer parameters [5]. A detailed procedure of the injection transformer design is presented in [6].

2.1. Transformer Design and Parameters

At the start of compensation, the magnetic flux and current in the coil start at zero and gradually increase. It means that the transformer flux is approximately twice the maximum value of the normal flux [4], [7]. This causes an inrush current in transformer and that requires the transformer to be rated two times larger than DVR. Thus, the transformer is large and expensive. The required parameters of an injection transformer for DVR laboratory model are:
- single phase, shell-type core,
- frequency - 50 Hz,
- rated power - 240 VA,
- primary winding - rated 240 V, 1 A (operating 120 V, 1 A),
- secondary winding - rated 60 V, 4 A (operating 30 V, 4 A).

The designed transformer is depicted at Fig. 2. DVR is in standby state, while the inverter side of series transformer is in short-circuit operation. That is when both of the switching devices on upper arms (or lower arms) of the inverter conduct simultaneously, and no voltage vector is injected into system. In this case, only transformer leakage reactance exists in circuit, since injected voltage is zero. During injection state, VSC generates compensating voltage. Injection transformer contributes to the elimination of the harmonics generated by the inverter. But there must be an LC filter applied, so that the transformer would not get overloaded.
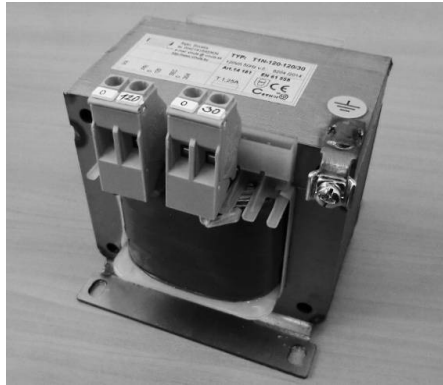
Fig. 2. Single-phase injection transformer - booster for DVR model

2.2. Transformer Tests

Various measurements and tests have been made on the real transformer in order to determine the exact parameters.

Transformer ratio
Transformer ratio is defined as a ration between primary and secondary voltage. The average value obtained by measurements is 3.64.

Winding resistance
The resistance of primary winding is 5 Ω and secondary 0.46 Ω (referred to the primary side is 6.1 Ω). The final resistance is 11.1 Ω.

Open-circuit test
Open-circuit test gives the values of a magnetizing current, a reactance, a no-load current and core losses. They are: I_{0N} = 154 mA, R_{FeN} = 5021 Ω, $X_{\mu N}$ = 1640 Ω, $L_{\mu N}$ = 5.22 H, P_{0N} = 11.5 W.

Short-circuit test
Short-circuit test is used to determine the winding impedances. U_{scN} = 11.35 V, z_{sc} = 4.7 %, P_{scN} = 11.25 W, X_{sc} = 2.37 Ω, $X_{\sigma 1}$ = 1.185 Ω, $X_{\sigma 2}$ = 0.09 Ω, $L_{\sigma 1}$ = 3.77 mH, $L_{\sigma 2}$ = 0.28 mH.
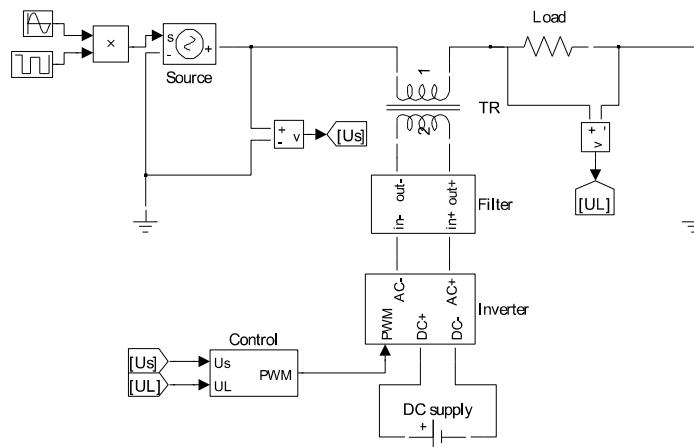

Fig. 3. Simulation model of DVR in Simulink

The parameters given by transformer tests are important mainly for implementation in simulation model. The simulation model was created in Matlab/Simulink (Fig. 3) and the complete laboratory model of DVR is depicted in Fig. 4.
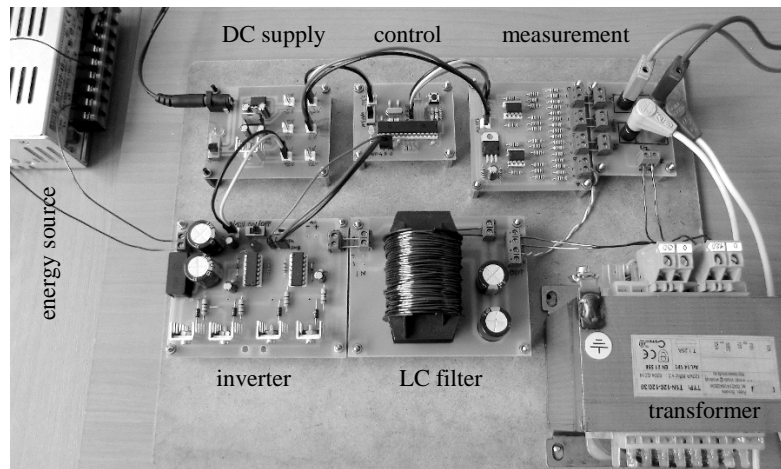

Fig. 4. Single-phase DVR laboratory model

3. Verification and Results

The complete DVR model has been constructed in laboratory environment. The inverter is connected to the secondary terminals of the transformer. The PWM switching frequency is 5 kHz. The control algorithm is based on feed-forward method. The actual RMS value of source voltage is calculated and compared with rated value (127 V). DVR losses and voltage drop are also considered. The maximum injected voltage is 98 V and an in-phase control technique is implemented, which means, that compensating voltage is in phase with the line voltage at every moment. For the control unit 16-bit DSC microcontroller dsPIC33FJ128MC802 was used.

The correct function of DVR laboratory model can be seen in Fig. 5. There are 3 voltages – the source voltage in the upper picture, the injecting voltage in the middle and the load side voltage at the bottom. They were obtained from real model measurements. Several voltage sags occurred with different depths. At every moment, DVR dynamically computes and generates remaining voltage, which is transported to the line voltage using the injecting transformer. The load voltage is securely held within allowed limits.
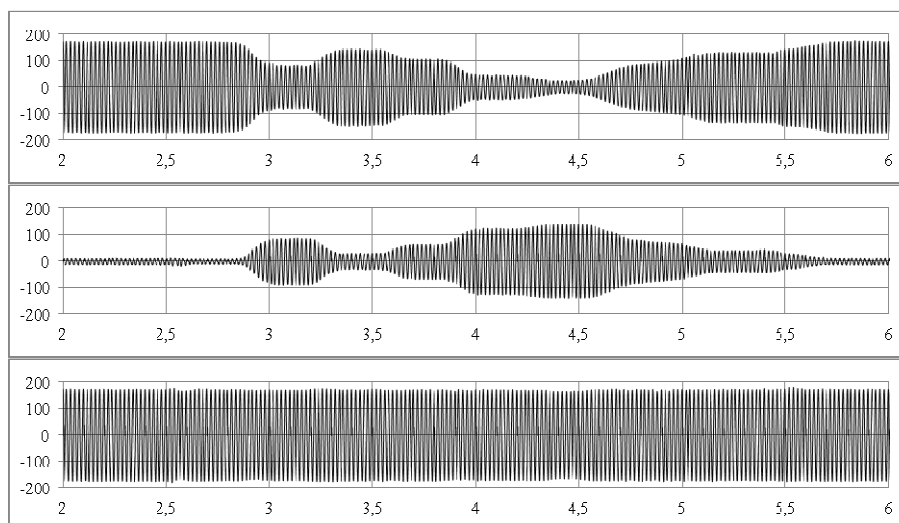

Fig. 5. DVR operation (measurement results)

Next, the simulation results are presented. Fig. 6 shows the source voltage, the injecting voltage and the load voltage during a short time period.
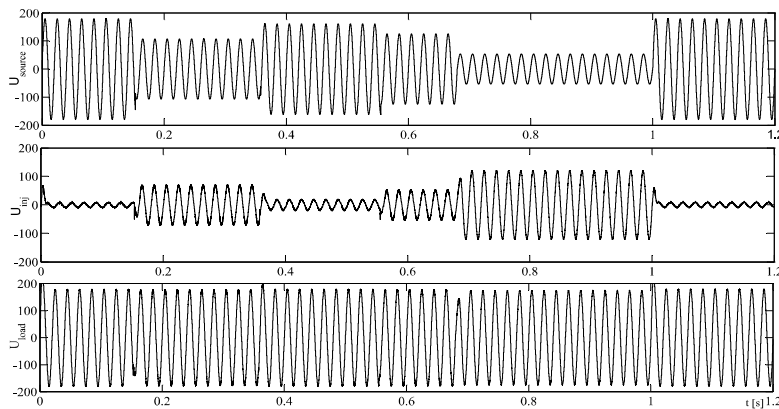

Fig. 6. DVR operation (simulation results)

As before, DVR works correctly and the compensating voltage is added to the source voltage through the injecting transformer. The load side voltage remains unaffected.

The voltage drop across the transformer in standby state and at rated load current is 24 V, which means that DVR should continuously compensate at least its own losses. Consequently, the VSC generates compensating voltage to cover voltage drop of DVR at every moment. It means that the energy for inverter must be permanently available.

4. Conclusion

Verification tests as well as simulations proved that the injection transformer for DVR model is designed properly. It is able to inject a compensating voltage to the line voltage reliably and satisfactorily. In terms of rating, the transformer is two times overrated in order to subdue the saturation effect of the magnetic core. Core cross section area is doubled as well as rated power. For the injected voltage, there is a synchronization loop implemented in the control unit which ensures phase locking with the line voltage. Many various measurements and simulation tests have been performed. The phase shift of injected voltage waveform (due to the transformer impedance) is so small that it can be easily neglected.

Acknowledgement

References

[1] CHAPMAN, D. *Introduction to power quality.* European Copper Institute publication, February 2012.

[2] HINGORANI, G. N., GYUGYI, L. *Understanding FACTS. Concepts and Technology of Flexible AC Transmission Systems.* New York: IEEE Press, 2000. p. 432. ISBN 0-7803-3455-8

[3] TANDJAOUI, M. N. et al. *Sensitive Loads Voltage Improvement Using Dynamic Voltage Restorer.* International Conference on Electrical Engineering and Informatics, 2011. Conference publication. IEEE Xplore digital library

[4] NIELSEN, J. G. *Design and control of a dynamic voltage restorer.* Dissertation thesis. Aalborg university, Denmark, 2002.

[5] KANTARIA, R. A. A *novel technique for mitigation of voltage sag/swell by Dynamic Voltage Restorer.* Electro/Information Technology (EIT), 2010 IEEE International Conference. Conference publication. p. 1-4

[6] SASITHARAN, S: *Rating and Design Issues of DVR Injection Transformer.* APEC 2008, IEEE. Austin, USA. ISBN 978-1-4244-1873-2

[7] CHANKHAMRIAN, W., BHUMKITTIPICH, K. *The Effect of Series-Connected Transformer in DVR Applications.* Energy Procedia 9th, 2011. str. 306 – 315.

Step Response of a Two-port Network Cascade

[*]Jarosław Szczepaniak

[*]Kielce University of Technology, Faculty of Electrical Engineering, Automatic Control and Computer Science, Division of Electrical Devices and Lighting Technology, al. Tysiąclecia P.P. 7, 25-314 Kielce, Poland, jszczepaniak @tu.kielce.pl

Abstract. This paper presents a method of finding the transfer function of a distributed parameter system - a transmission line - based on a two-port network cascade. A signal-flow graph theory is applied to construct said transfer function. As a result an expression was reached in the form of a rational function with 2 simple poles and 4 poles of the N-2 order per N quadripoles under resistive load. Based on this transfer function a step response and pulse wave response graphs of the load were plotted. Achieved results allowed to formulate conclusions regarding digital signals transmission capability.

Keywords: transfer function, two-port network cascade, transient state.

1. Introduction

Consideration of concepts related to pulse wave propagation in a quadripole cascade is directly linked to transient analysis of transmission lines. Obtaining the solution for a given set of equations used to describe the problem requires combining of various computation methods. One way to compute telegraph equations is to use the finite difference method and Fehlberg method [1]. Another possibility [2,4] is to employ two-dimensional Laplace transform. However, this method can only be used in lossless transmission lines. For such lines a finite difference method, in respect to time and distance as well as time and frequency, may be used [3]. A transient-state investigation of transmission line signal propagation, used to locate faults, has been performed by introducing signals of various waveforms. Changes in the signal after it passed a given amount of quadripoles were analyzed [6]. This paper employs a transfer function of a two-port network cascade, which includes longitudinal and transverse lossy elements [7,8].

2. Calculating the Two-port Network Cascade Transfer Function

Transfer function of a cascade consisting of *n* identical T-type networks can be expressed as follows:

$$T = \frac{2}{2(R_0 + sL_0)(G_0 + sC_0) + 2} \frac{(2(R_0 + sL_0)(G_0 + sC_0) + 3)}{(2(R_0 + sL_0)(G_0 + sC_0) + 2)(2(R_0 + sL_0)(G_0 + sC_0) + 3) - 1} \bullet$$

$$\bullet \left[\frac{(2(R_0 + sL_0)(G_0 + sC_0) + 2)}{(2(R_0 + sL_0)(G_0 + sC_0) + 2)^2 - 1} \right]^{n-3} \frac{1}{2(R_0 + sL_0)(G_0 + sC_0) + 1 + \dfrac{2(R_0 + sL_0)}{(R_0 + sL_0) + R_2}} \qquad (1)$$

Where: R_0, L_0, G_0, C_0 – single network parameters (singular parameters of the transmission line), G_2 – load's conductance.

Poles of the transfer function (1) are of significant importance when it comes to calculating an inverse transform. There are two simple poles for $(R_0 + sL_0)(G_2 + G_0 + sC_0) + 1 = 0$:

$$s_5 = \frac{-(G_0 + G_2)L_0 - C_0 R_0 - \sqrt{((G_0 + G_2)L_0 + C_0 R_0)^2 - 4C_0 L_0 (1 + (G_0 + G_2)R_0)}}{2C_0 L_0}$$

$$s_6 = \frac{-(G_0 + G_2)L_0 - C_0 R_0 + \sqrt{((G_0 + G_2)L_0 + C_0 R_0)^2 - 4C_0 L_0 (1 + (G_0 + G_2)R_0)}}{2C_0 L_0}$$

(2)

As well as four poles of N-2 order for $[(R_0 + sL_0)(G_0 + sC_0) + 2]^2 - 1 = 0$

$$s_1 = \frac{-G_0 L_0 - C_0 R_0 - \sqrt{(G_0 L_0 + C_0 R_0)^2 - 4C_0 L_0 (1 + G_0 R_0)}}{2C_0 L_0}$$

$$s_2 = \frac{-G_0 L_0 - C_0 R_0 + \sqrt{(G_0 L_0 + C_0 R_0)^2 - 4C_0 L_0 (1 + G_0 R_0)}}{2C_0 L_0}$$

$$s_3 = \frac{-G_0 L_0 - C_0 R_0 - \sqrt{(G_0 L_0 + C_0 R_0)^2 - 4C_0 L_0 (3 + G_0 R_0)}}{2C_0 L_0}$$

$$s_4 = \frac{-G_0 L_0 - C_0 R_0 + \sqrt{(G_0 L_0 + C_0 R_0)^2 - 4C_0 L_0 (3 + G_0 R_0)}}{2C_0 L_0}$$

(3)

After examining expressions (2) and (3) it is easy to conclude that all poles are real, which means that there will be no oscillations in the circuit as long as:

$$((G_0 + G_2)L_0 + C_0 R_0)^2 > 4C_0 L_0 (1 + (G_0 + G_2)R_0)$$

(4)

For simple poles and:

$$(G_0 L_0 + C_0 R_0)^2 > 4C_0 L_0 (1 + G_0 R_0)$$

(5)

For poles of higher orders. All the poles will be real for $R_0 > 2\sqrt{\frac{L_0}{C_0}}$ assuming miniscule leakage

($G_0 \approx 0$) and large resistance of the load ($G_2 \approx 0$).

This condition is untrue for power lines and telecommunication lines, which means that those poles would be complex conjugates with negative real part.

In order to obtain an inverse transform of (1) partial fraction decomposition was performed [5]. Despite the relative simplicity of the method, which is based on well-known algebraic decomposition of a rational function and inverse transform of individual fractions, it is possible to interpret it using Laurent's theorem, where fractions' coefficients are equivalent to residues of (1) around particular points – poles.

Transfer function (1) can be then expressed as a sum of simple fractions [5]:

$$T(s) = \frac{L(s)}{N(s)} = \frac{C_5}{s - s_5} + \frac{C_6}{s - s_6} + \sum_{i=1}^{4} \sum_{k=1}^{n-2} \frac{C_{ik}}{(s - s_i)^k}$$

(6)

where C_{jk} factors:

$$C_{ik} = \frac{1}{(n-3)!} \lim_{s \to s_i} \frac{d^{n-2-k}}{ds^{n-2-k}} \left[\frac{L(s)}{N(s)} (s - s_i)^{n-2} \right]$$

(7)

C_5 and C_6 can be determined through the use of Heaviside's equations as they concern simple poles:

$$C_j = \frac{L(s_j)}{N'(s_j)}, \qquad j = 5, 6$$

(8)

Therefore, the transfer function of (1) is equal to:

$$L^{-1}\{T(s)\} = C_5\, e^{s_5 t} + C_6\, e^{s_6 t} + \sum_{i=1}^{4}\sum_{k=1}^{n-2} \frac{C_{ik}}{(k-1)!} t^{k-1} e^{s_i t} \tag{9}$$

In order to find the response of the circuit to a signal defined by transfer function $U(s)$ it is necessary to find an inverse transform of $U(s)T(s)$, which, in practice, requires an introduction of an additional pole $s_7=0$ for DC and additional conjugated pole pair $s_{7,8} = \pm j\omega$ for a sine.

3. Pulse Wave Signal

A singular impulse of a pulse wave signal characterized by amplitude A and width $a>0$ can be expressed:

$$u(t) = A\mathbf{1}(t) - A\mathbf{1}(t-a) \tag{10}$$

While its transform:

$$U(s) = \frac{A}{s} - \frac{A}{s} e^{-as} \tag{11}$$

Therefore, the voltage transform at the n-membered cascade output equals:

$$U_2(s) = \frac{[(R_0 + sL_0)(G_0 + sC_0) + 2]^{n-3}}{\{[(R_0 + sL_0)(G_0 + sC_0) + 2]^2 - 1\}^{n-2}} \frac{A}{s(R_0 + sL_0)(G_2 + G_0 + sC_0) + 1} \left(1 - e^{-as}\right) \tag{12}$$

where: e^{-as} represents time shift by a

Voltage related to time – inverse transform of (12):

$$u_2(t) = C_5\left(e^{s_5 t} - e^{s_5(t-a)}\right) + C_6\left(e^{s_6 t} - e^{s_6(t-a)}\right) + \sum_{i=1}^{4}\sum_{k=1}^{n-2} \frac{C_{ik}}{(k-1)!}\left[t^{k-1} e^{s_i t} - (t-a)^{k-1} e^{s_i(t-a)}\right] \tag{13}$$

Equations (7) and (8) remain valid by substituting $L(s)$ with $L_1(s)=AL(s)$ and $N(s)$ with $N_1(s)=sN(s)$.

4. Numerical Calculations

Numerical simulations were performed based on author's MATLAB code.

a)   b)
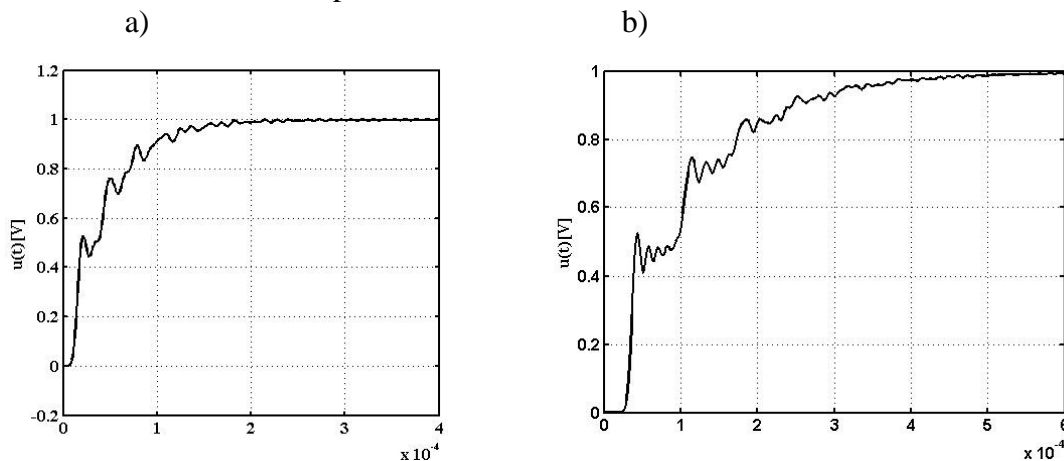
Fig.1. Course of the voltage at the end of the cascade by forcing a unit jump at:
a) N = 4 four-terminal networks, b) N = 10 four-terminal networks

The biggest challenge was to determine C_{jk} factors from (7), which required symbolic computation of $L(s)/N(s)$ derivatives. While MATLAB allows for such calculations the time required increases significantly for derivatives of higher orders (>6). Therefore only N=8

quadripole results are presented. As one can intuitively predict, it is shown in fig. 1. that by increasing the number of two-pole networks the delay at the output increases, which has a significant effect on the received pulse wave signal. It is then possible to determine the minimal impulse time which can still be correctly interpreted at the output, which allows determination of maximum transmission speed of such signals.

5. Conclusion

Transient state analysis of lossy distributed parameter systems is a difficult circuit theory task. In most cases there are no analytical solutions and the only ways to obtain information about current and voltage waveforms are approximate numerical integration methods. The presented method, which is based on an analysis of a cascade of identical quadripoles, makes it possible to obtain the transfer function of N two-pole networks and then $U_2(s)$ output voltage for known input signal transform. Inverse transform of the voltage yields its relation to time.

By analyzing obtained waveforms it is easy to notice that an increase of the number of quadripoles results in an increase of output delay, which, combined with a short pulse wave signal, may result in output signal misinterpretation. Therefore, it is possible to determine the maximum transmission speed for a given transmission line.

References

[1]   BARON B., J. KOLAŃSKA-PŁUSKA, J. KRYCH, *Transient Analysis of nonhomogenous transmission line loaded by the wto - RL network terminal*, IC-SPETO 2001

[2]   BRANCIK, L., *Simulation of Multiconductor Transmission Lines Using Two-Dimensional Laplace Transformation*, ACCTD 2001

[3]   CLAYTON R. PAUL, *Analysis of Multiconductor transmission lines*, John Wiley & Sons, Inc., 2012

[4]   HWANG, C., LU, MJ: *Numerical inversion of 2-D Laplace transforms to fast Hartley transform Computations*, Journal of the Franklin Institute, 1999

[5]   OSIOWSKI J .: *An outline of operator account*, WNT, Warsaw, 1981

[6]   W. TARCZYNSKI*, pulse methods in locating faults in lines electrical*, Opole University of Technology in 2006

[7]   WLODARCZYK M .: *The operator of the transfer function of a string of equal four- terminal networks*, XXXV International Conference on Fundamentals of Elektrotechnics and Circuit Theory -IC-SPETO, Ustroń 2012. P. 93-94

[8]   WLODARCZYK M. ZAWADZKI A .: *Application of graph theory to determine the transfer function of static and uniform chain*, XXXVI International Conference on Fundamentals of Elektrotechnics and Circuit Theory - IC-SPETO, Ustroń 2013. P. 53-54

Patrial Discharge in Air and Transformer Oil

Lukáš Varačka, Jozef Kúdelčík

University of Žilina, Faculty of Electrical Engineering, Department of physics, Univerzitna 1, 01026 Žilina, Slovakia, varacka@fyzika.uniza.sk

Abstract. The monitoring, detection and analysis of partial discharge (PD) in high voltage electrical systems allow the identification and forecast problems associated with transformers and insulators. PDs can be destructive to electrical insulation as they may degrade the material in time. Due to the complexity of PDs as well as factors that can affect PD characteristics, the research on PD measurement is still active. PD is characterized by high frequency current pulses that occur in the interior of high voltage apparatus. This paper compares PD measurements made using inhomogeneous test arrangements in laboratory air and transformer oil. The apparent charge magnitude, voltage and the time of occurrence of each PD event were recorded by LDS 6.

Keywords: Partial discharge, charge, PD patterns, transformer oil.

1. Introduction

The method of partial discharges is use to analyze of more difficult entities like electrical devices or high voltage (HV) distribution transformers. In case of transformers, the diagnostic is performed for better determination of their insulation characteristics and range of damage. It is based on the evaluation of current values from partial discharges. The combination of more measuring methods and simultaneously records of acoustical, electrical and chemical activity from partial discharges located inside insulation systems of transformers is one of the most important diagnostic methods at the test stations or at the place application of transformers [1].

Study of partial discharge mechanism in liquid dielectric was begun with simply arrangement of a needle-to-plane electrode upon to form the basis of the measuring standards. On the basis of these studies was obtained more correct information about actual breakdown process in liquid dielectrics. PDs are initiated at stress enhancement sites on the test electrodes, where the gas cavity - bubbles can create [2 - 7]. The measurement in work [8] showed that partial discharges in synthetic ester oil were started to create from 25kVrms for the hyperbolic shaped needle electrode, with a radius of 20 µm at its tip at the distance of 30 mm from the plane electrode. Their multitude and charges exceed hundreds of pC with increasing voltage. By comparison with PDs in mineral transformer oils [9, 10] they have comparable characteristics, therefore time to the creation of bubble is around 1 µs. The similar results were obtained by analysis of discharges, which were carried out at the laboratory environment by using different electrode configurations with AC voltage [11]. Overall of published papers can be suppose that continuous exposure of liquid dielectric and although the existence of low PDs levels causes progressive degradation of the dielectric in the long therm.

Measurements of PDs are very often connected with acoustic emission technique [12, 13]. Acoustic emissions are transient stress waves generated by rapid release of energy from localized sources within a material such as crack initiation and growth, and are characterized as bursts of ultrasonic energy, the measurement can be made in wide range of frequencies 100 kHz – 3 GHz. Analysis of partial discharge in transformer oil by the acoustic emission signal in work of Sarathi [13] indicated that the energy content of the acoustic emission signal was high in the frequency

range of 250–750kHz under DC voltages. The energy content had maximum for AC voltage generated acoustic emission signal in the range 20–250 kHz.

2. Galvanic connection with measured object.

Measurement of discharge activity can be carried out by different methods: non-electric (acoustic, optic, thermoelectric, etc.) and electric (loss tangent, spurious electric fields, with measuring impedance, capacitive or inductive sensors, etc.). Galvanic connection of measuring impedance with measured object at the measurement of PDs is one of the most sophisticated methods, which is designed to observe of insulation systems state in HV and VHV systems. This method belongs to global methods of PDs measurement. It is based on direct sensing current pulses of PDs which are superimposed on power supply. Measuring impedance is designed for the decoupling of the PD current pulses on the PD coupling capacitor, changing in equivalent voltage pulses and forwarding to the PD detector (bandwidth 20 MHz, max. current 5 A, optional 50 A).
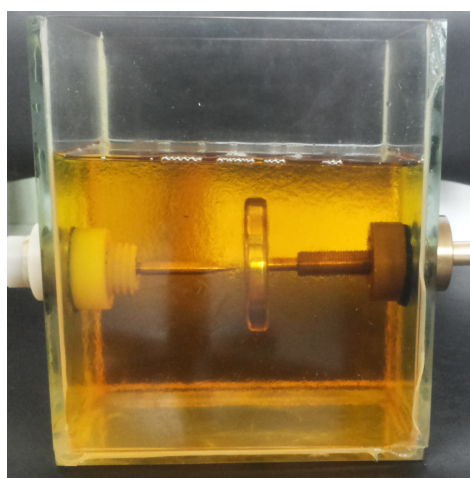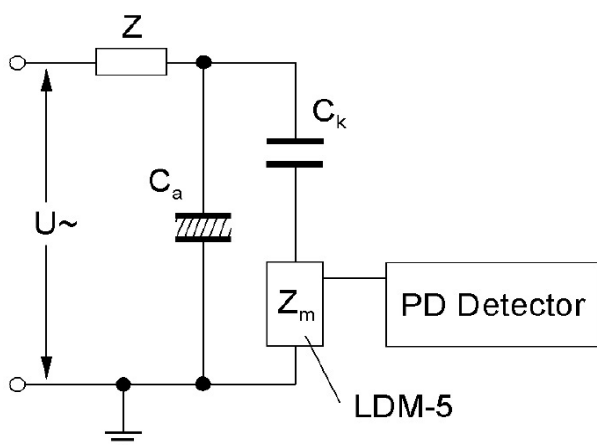
Fig. 1. (a) The electrical scheme of sep-up for measurement of partial discharge (Z – input impedance; U~ – HV AC source, C_a – measuring object represented by capacitance, C_k – coupling capacitance, Z_m or LDM-5 – measuring impedance, PD detector – LDS-6. (b) Photo of electrode arrangement in discharge vessel.

In the basic PD test circuit of Fig. 1a, the noise blocking filter is used to reduce the electromagnetic noise coming from the high voltage source. In addition, it prevents the PD signal from travelling through the high voltage transformer [14]. The coupling capacitor C_k provides a closed path for the discharge pulse current and is connected in series with the measuring impedance Z_m - LDM-5. The test object is presented as a capacitance C_a. At the measuring impedance, voltage pulses are formed which are then amplified and analyzed by a discharge analyzer - LDS-6 and finally displayed in monitor. The high voltage was from invertor. The advantage of this circuit is ability to measure grounded object, and therefore is appropriate to use it when it is not possible connect the output to the ground, or in the case of high capacities of measuring objects. In the case of PD measurements by electrical methods, the calibration process is very essential in order to obtain reliable results regarding the magnitude of the PD.

3. Experimental results and discussion

The first experiment was performed in air. The schematic diagram of the test set up is presented in Fig. 1b. The needle is placed on the high voltage connected contact, so we observed negative corona discharges. The radius of the tip was 20 μm and the distance from the tip of the needle to the grounded contact were 15, 20 and 25 mm and the inception voltages were 5 kV, 5.3 kV and 5.5 kV,

respectively. In the case of point-point electrode arrangement for distance 25 mm the inception voltage was 5.7 kV. The results for acquisition time 20 seconds of this experiment and distance 25 mm are presented in Table 1. The repetition rate of the corona discharges in air is relative high. We can also observe that the repetition rate increases with increasing applied voltage what is the characteristic of corona discharges. The magnitude charges of PD near inception voltage are about 110 pC. With increasing voltage their values decrease because the repetition rate increases. With increasing voltage the discharge activity was only for negative values of voltage, while for point-point from voltage 8.6 kV partial discharges were detected also in positive part of AC voltage. The phase resolved partial discharge (PRPD) pattern of the corona discharges in air at 9V is presented in Fig. 2a.
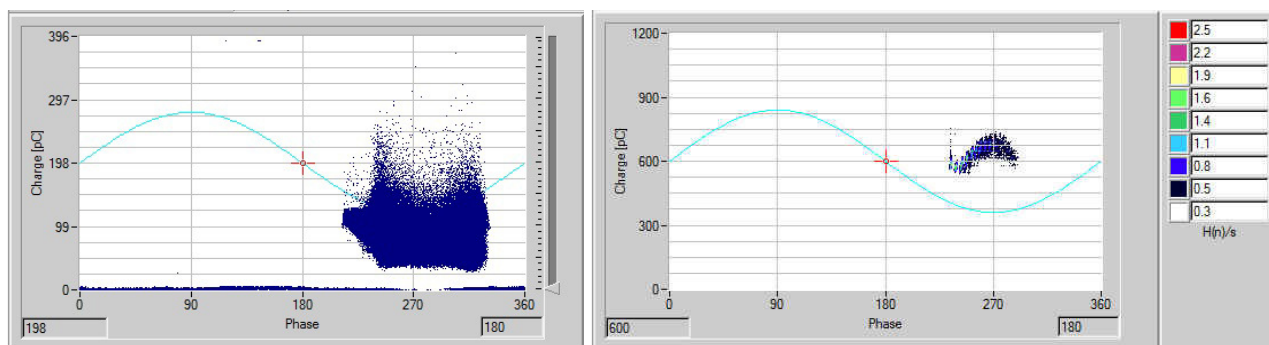

Fig. 2. The PRPD pattern for VN point – plane (25 mm) in air at 9 kV and in transformer oil at 30 kV

The second experiment has been focused on negative corona discharges in transformer oil ITO with same aparature (Fig. 1b). Sustained corona discharge in oil can reduce its dielectric strength, and over time the corona activity could increase and finally result in oil breakdown and failure of the component. The effect of parameters such as temperature, moisture and pressure on corona I oil is of importance especially for real application in power transformers. The results for acquisition time 60 seconds of this measurement are presented in Table 1. The inception voltage for electrode distance 25 mm was 26kV. It also concluded that the inception voltage for negative corona is slightly less than for positive corona. From Table 1 we can observe that the repetition rate of the corona discharges in oil is very small. We can also observe that the repetition rate increases with increasing applied voltage as were observed in air. The PRPD patterns of the corona discharges in oil at 30kV are presented in Figure 2b.

Air			Transformer Oil ITO 100		
Voltage [kV]	N/pulse Repetion rate	Qmean [pC]	Voltage [kV]	N/pulse Repetion rate	Qmean [pC]
5.5	15	109	27.5	8	590
7	107	91	30	14	633
9	338	72	32.5	28	696
11	437	49			

Tab. 1. Results of the experiment for 25 mm distance point – plane.

The PRPD patterns are positioned close to the peak of the applied voltage. The small phase shift from the peak of the applied voltage in transformer oil could be explained by the presence of charge around the tip of the needle. Their diffusion is one or two order smaller as in air. The presence of charge could alter the electric field at the tip of the needle, causing the appearance of corona discharges before the voltage peaks. The study shows that by increasing the applied voltage the number and magnitudes of PD pulses in the PD burst increases. The mean values of the PD magnitudes range from 590 pC to 700 pC. The PD pulses in Fig. 2b do not display a large scatter of PD magnitudes, the magnitudes of the majority of the PD pulses are in a range from 575 pC to 750

pC. At other voltage this difference was also no more than 10%. Moreover, the repetition rate of the PD pulses slowly increases with increasing voltage. This specific behavior of the PD pulses could be attributed to corona discharges in oil [14].

4. Conclusion

This work was paid to the research of partial discharge in air and transformer oil. Throughout the measurement of partial discharges by using basic electrode configurations under high voltages, the apparent charge magnitude and the time of occurrence of each PD event were recorded and stored together with the instantaneous value of the test voltage. From the analyzed data it can be seen the big different in values of the mean charge and numbers of PD during one period. In the case of air there were bigger numbers of PD but with smaller charges considering to transformer oil.

The obtained data in these series of tests will be useful for the classification study of PD sources on offline or online attained PD data.

Acknowledgement

References

[1] GACEK, Z., SZADKOWSKI, M., MALITOWSKI, G., WITOSB, F., OLSZEWSKA, A., *Anusual application of partial discharges to diagnose of high voltage power transformers*, Acta Physica Polonica, Vol. 120, No. 4, 609-615, 2011.

[2] FORSTER, E.O., *Progress in the understanding of electrical breakdown in condensed matter*, J. Phys. D., Appl. Phys., Vol. 23, pp.1506-1514, 1990.

[3] DEVINS, J.C., RZAD, S.J., AND SCHWABE, R.J., *Breakdown and prebreakdown phenomena in liquids*, J.Appl. Physics, Vol. 52, pp. 4531-4545, 1981.

[4] BEROUAL, A., AND TOBAZEON, R., *Prebreakdown phenomena in liquid dielectrics*, IEEE Trans. Electrical Insulation, Vol. 21, pp. 613-627, 1986.

[5] TORSHIN, Y.V., *Prediction of breakdown voltage of transformer oil from predischarge phenomena*, IEEE Transactions on Dielectrics and Electrical Insulation, vol. 10 (6), pp. 933-941, 2003.

[6] LESAINT, O., AND TOBAZEON, R., *Streamer generation and propagation in transformer oil under ac divergent field conditions*, IEEE Trans. Electr. Insul., Vol.23, pp.941-954, 1988.

[7] YAMASHITA, H., AND AMANS, H., *Prebreakdown density change, current and light emission in transformer oil under non-uniform field*, J.Electrostatics, Vol. 12, pp.253-263, 1982.

[8] POMPILI, M., MAZZETTI, C., AND BARTNIKAS, R., *PD pulse burst characteristics of transformer oils*, IEEE Trans. on Power Delivery, Vol. 21, pp. 724-728, 1995.

[9] EBERHARDT, R., MUHR, H.M., LICK, W., WIESER, B., SCHWARZ, R., PUKEL, G., *Partial discharge behaviour of an alternative insulating liquid compared to mineral oil*, In Power Modulator and High Voltage Conference (IPMHVC), 2010 IEEE International 23-27, P. 426 - 429 DOI: 10.1109/ IPMHVC.2010.5958385, May, 2010.

[10] KOLCUNOVÁ, I., MARCI, M., KURIMSKÝ, J., *Koróna v oleji,* Starnutie elektroizolačných systémov, No.9, str. 13-16, 2010.

[11] ALTAY, O., KALENDERLL, O., MEREV, A., DEDEOGLU, S., GULNIHAR, K., *Preliminary partial discharge measurements with a computer aided partial discharge detection system, International Conference on Electrical and Electronics Engineering*, ELECO, IEEE, I-345 - I-348, 5-8 Nov, 2009.

[12] BALOGH, J., DŽMURA, J., PETRÁŠ, J., *Kapacitné snímače čiastkových výbojov*, Starnutie elektroizolačných systémov, roč. 6, no.1, 2011.

[13] SARATHI, R., SINGH, P. D., DANIKAS, M. G., *Characterization of partial discharges in transformer oil insulation under AC and DC voltage using acoustic emission technique*, Journal of Electrical Engineering, vol. 58, no. 2, 91–97, 2007.

[14] KANAS, V., *Condition Assessment of the Insulation of On-Load Tap Changers by Partial Discharge Measurements,* PhD. Thesies in Inteligent electrical power grids, Delft University of Technology, 2013.

Analysis of bridge rectifier operation in AC circuit

Mirosław Wciślik, Paweł Strząbała

Kielce University of Technology, al. Tysiąclecia Państwa Polskiego 7, 25-314 Kielce, Poland

Department of Electrotechnics, Automatic Control and Computer Science, m.wcislik@tu.kielce.pl, pstrzabala@tu.kielce.pl

Abstract. A full-wave bridge rectifier is one of the most often used non-linear load. A main area of it using are single-phase power suppliers which constitute part of the most of electronic devices. These devices may be found in commercial and communal sectors of electric energy consumers. Power consumption of that devices is not large, however large number of it is working simultaneously in the power system may cause that the total effect of voltage disturbances in the power system is significant. For the purpose of investigation of the phenomena in the system, propagations of higher harmonics and the reactive power analysis, the model enabling the simulation of the circuit with the full-wave rectifier bridge supplied from AC voltage source by the additional inductance was worked out. The non-linear model of the bridge rectifier was proposed. The simulation and the preliminary analysis of instantaneous waveforms of currents and voltages were performed in the continuous mode of rectifier operation.

Keywords: nonlinear load**,** bridge rectifier, continuous operation, modeling

1. Introduction

The full-wave bridge rectifiers are one of the most frequently used types of the non-linear load of the mains. A basic mode operation of the rectifier known from [1,2] is the interrupted operation mode. The mode occurs, when the filtering capacitor is cyclically charged by the rectifier and discharged by the load resistor and in the cycle is observed time period without current flow.. In the mode the rectifier generates the absolute value of the voltage and recharges the capacitor, when the rectified supply voltage is greater than the output voltage and the doubled forward voltage of diodes of the bridge. When the single mains load with the bridge rectifier is considered the interactions of the load and the power system may be omitted. However, when dozens of loads such as LED lamps or PC computers with power supplies without the power factor correction are turned on, the interactions can cause deformation of the supply voltage in local mains nodes. This phenomenon depends on „the rigidity" of the mains, that is to say it depends on the equivalent output impedance of the power system. Therefore, for the proper interpretation of that influence, the power system should be considered as the ideal voltage source to supply the bridge rectifier by the series connected inductance and the resistance. In such circuit and the output voltages smaller than the supply voltage magnitude the continuous operation mode of the rectifier is observed. In the bibliography authors concentrate mainly on the analysis of output voltages of the rectifier. According to [3], the non-linear load lowers the power factor, makes worse the energy efficiency and causes the growth of the inductance seen from terminals of the power source.

The question arises: How will the bridge rectifier be seen together with the inductance from terminals of the power source? To answer for it the model of above presented system was worked out.

2. The bridge rectifier

The bridge rectifiers are supplied most often directly from the power system or through the additional transformer [2]. The output voltage of the rectifier should have small magnitude of ripple voltage U_t. Therefore low-pass filters are used on the output of the system. In low-power rectifier circuits, usually capacitor is connected as a filter – figure 1. The mean value of the output voltage

U_o and magnitude of ripple voltage U_t are fundamental output quantities of rectifying system – figure 2. The theoretical rectifier output voltage is denoted as u .
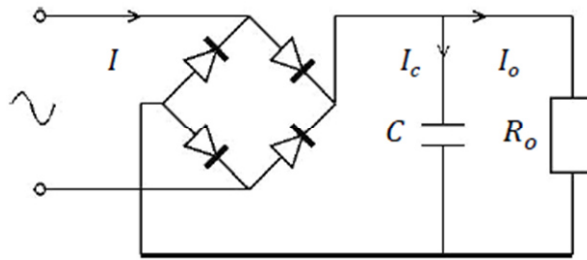

Fig. 1. The diagram of the full-wave bridge rectifier with capacitive filter [2]
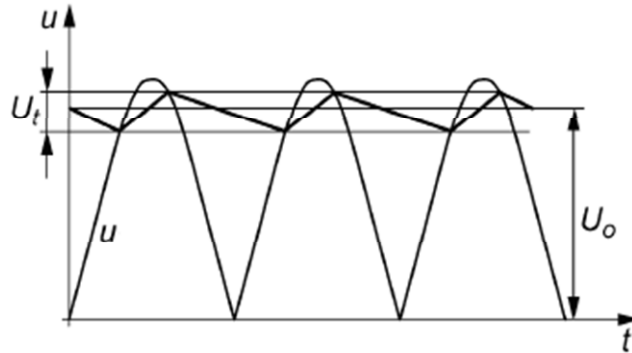
Fig. 2. Waveforms of voltages in the full-wave rectifier with capacitive filter. u - the output voltage without load, U_o – the output voltage mean value , U_t – the magnitude of ripple voltage [2]

The output voltage U_o achieves the constant value with accuracy to variable component. The ratio of the rms value of variable components of the waveform to the value of the constant component is defined as ripple factor k_t. For the resistant load the factor k_t is described as [2]:

$$k_t = \frac{I_{sk}}{I_o} = \frac{U_{sk}}{U_o} \tag{1}$$

where I_{sk}, U_{sk} are the rms values of the variable components of the current and the voltage of the load, I_o, U_o are the mean values of the current and the voltage of the load respectively.

The magnitude of the ripple voltage U_t may be calculates from the relation [4]:

$$U_t = \frac{U_o}{fCR_o} \tag{2}$$

The value of the ripple voltage in the full-wave rectifier with filter capacitor is described under the assumption that the waveform of the output voltage has approximately a triangular shape. The rms value of the voltage U_{sk} of such waveform is as follows [2]:

$$U_{sk} = \frac{U_t}{2\sqrt{3}} \tag{3}$$

3. The analysis of the circuit with the full-wave bridge rectifier

The diagram analyzed circuit is presented in fig. 3. The circuit contains the full-wave bridge rectifier loaded by the capacitor C and the resistance of the load R_o. The rectifier is supplied a sinusoidal voltage with the angular frequency ω, through the series connected inductance L and the

resistance R_s which model the series equivalent impedance other elements of the power supply system.
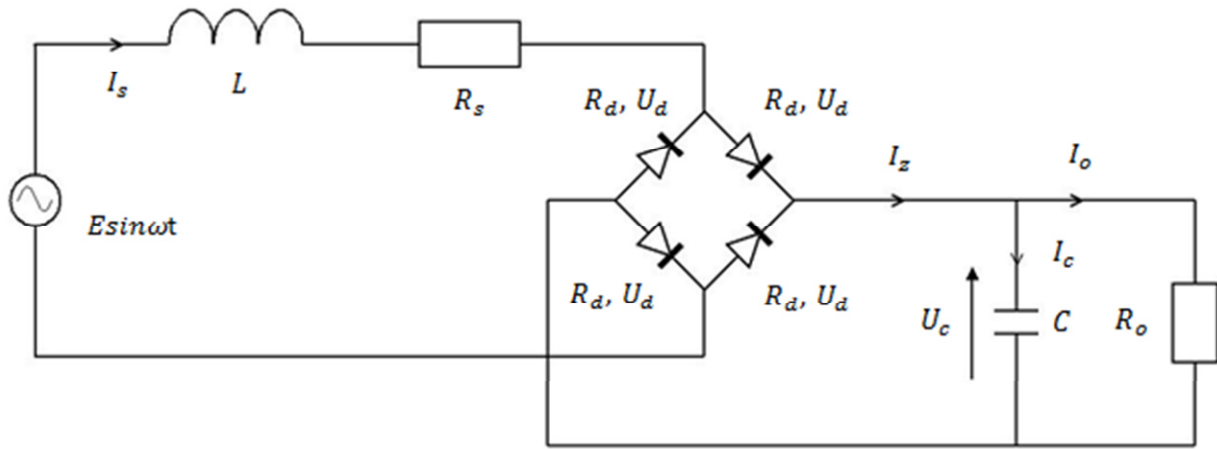
Fig. 3. The analyzed circuit diagram for the continuous operation mode of the bridge rectifier.

On the basis of currents and voltages waveforms in the circuit in figure 3 analyses, simulated with use of the program PSpice, the model of the rectifier for the alternating current, using the function signum was elaborated. For the continuous operation mode of the bridge rectifier the circuit may be described with equations:

$$L\frac{dI_s}{dt} = E \cdot \sin(\omega t) - I_s \cdot (R_s + 2R_d) - (2U_d + U_c) \cdot \text{sign}(I_s) \qquad (4)$$

$$C\frac{dU_c}{dt} = |I_s| - \frac{1}{R_o} \cdot U_c \qquad (5)$$

where I_s represents the instantaneous value of the current flowing through the rectifier circuit, the inductance L and the resistance R_s of the supply system, R_d - the series resistance of the diode in conduction state.

The bridge rectifier for the power source is seen as the non-linear load, whose voltage is proportional to the function signum of the current I_s, whereat the proportion coefficient is a voltage, which is a sum of the voltage on the capacity C and voltage drops on two conductive diodes. With the bridge rectifier out the absolute value of the input current of the rectifier, filtered on parallel connected: the capacitor C and the resistance of the load R_o.

For the purpose of the simplification of the analysis calibrating of the time and reference variables were used:

$$\tau = \omega t; \quad X = \omega L; \quad I_m = \frac{E}{X}; \quad Y = \omega C \qquad (6)$$

Using the dimensionless variables (7 and 8):

$$i_s = \frac{I_s}{I_m}; \quad u_d = \frac{U_d}{E}; \quad u_c = \frac{U_c}{E} \qquad (7)$$

$$r_z = \frac{R_s + 2R_d}{\omega L}; \quad r_o = \frac{R_o}{\omega L}; \quad y = XY = \omega^2 LC; \qquad (8)$$

equations (4 and 5) can be written as:

$$\frac{di_s}{d\tau} = sin\tau - i_s \cdot r_z - sign(i_s) \cdot (2u_d + u_c) \tag{9}$$

$$\frac{du_c}{d\tau} = \frac{1}{y \cdot r_o}(|i_s| \cdot r_o - u_c) \tag{10}$$

The simulation of such circuit performed in the system MATLAB for the amplitude of the supply voltage $E = 24V$ about the frequency $\omega = 314\,rad/s$, the inductance $L = 64mH$, the resistance $R_s = 1m\Omega$, the forward voltage of the diode $U_d = 0.7\,V$, the forward resistance of the diode $R_d = 0.04\,\Omega$, the resistance of the load $R_o = 10\,\Omega$ and the capacity $C = 1mF$. On the basis equations (7 and 8), for such data determined values of dimensionless parameters of the simulated circuit: $r_o = 0.5$, $r_z=0.004$, $y=6.33$, $u_d=0.03$. Obtained waveforms are identical for the simulation in the program PSpice and MATLAB.

The waveforms of currents and voltages in the circuit present figures 4 and 5. These waveforms are characteristic for the continuous operation of the rectifier. The output voltage U_c is substantially lower than the amplitude of the supply voltage. In this case the current I_s contains the countable number of zero crossings.
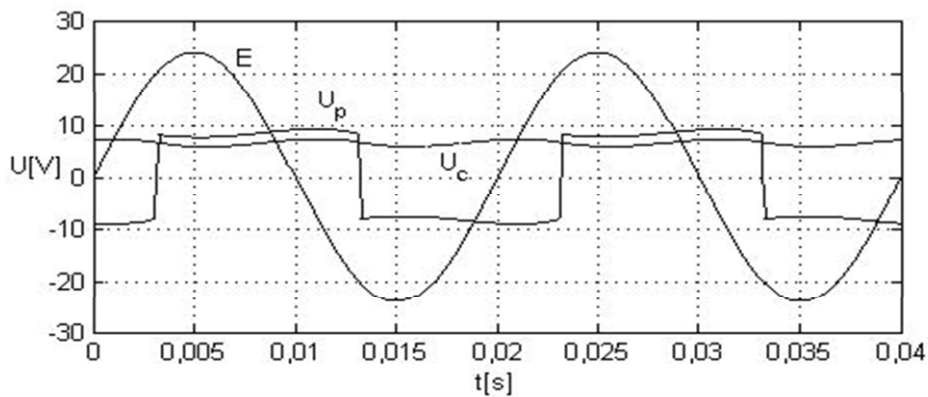

Fig. 4. The waveforms of voltages: E – the voltage amplitude of the power source, U_p- the voltage on the rectifier seen from terminals of the power source, U_c - the output voltage.
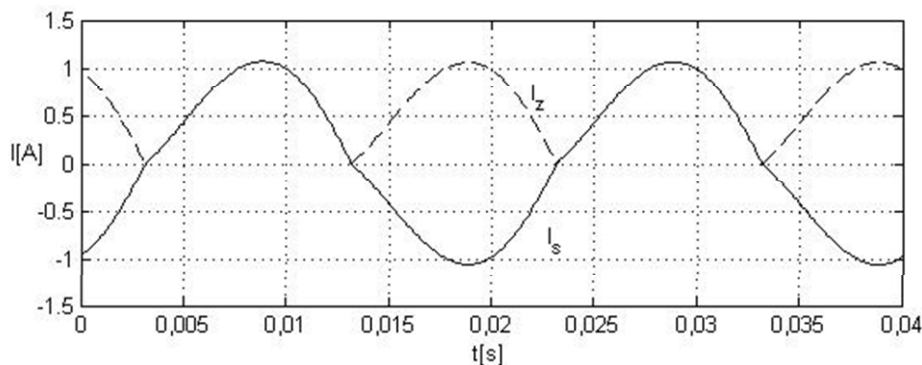

Fig. 5. The line currents I_s and I_z in circuit.

The mean value of the output voltage is equal $6{,}57\,V$, whereas fluctuations of this voltage about the frequency 100 Hz amounts to approx. $1.5\,V$. These quantities are an important out parameter of the system of the rectifier. Limiting conditions of this operation that is such at which the rectifier passes to mode of interrupted operation get out of loads of the rectifier. On figures 6 and 7 presented waveforms of the voltage on the rectifying bridge and the input current I_s and the output current I_z for the interrupted operation. These waveforms were obtained for the resistance of the load $R_o =$

35 Ω, where $r_o = 1.74$, whereas remaining parameters were assumed like for mode of continuous operation of the rectifier. The current for determined time intervals is equal the zero. For these intervals the current I_s contains uncountable number of zero crossings. The amplitude of ripple U_t of output voltage U_c is equal $1\ V$, whereas the mean value of this voltage is equal $12.37\ V$. This means that after the change of the parameter r_o the mean value of the output voltage increases, whereas amplitude of ripple decrease.
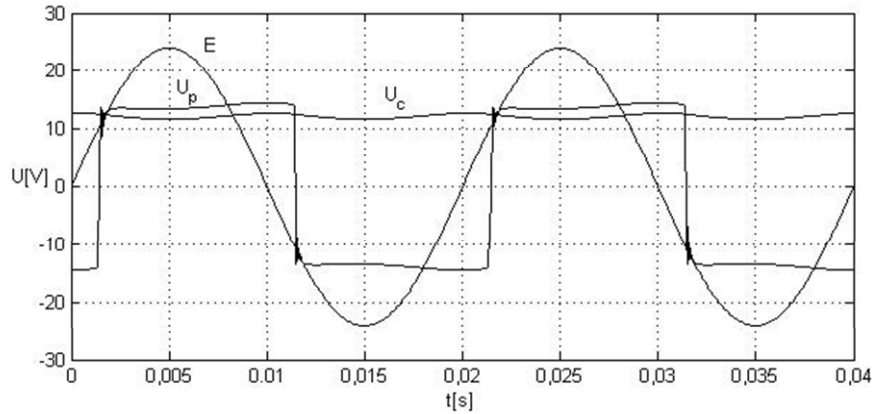

Fig. 6. The waveforms of voltages: E – the voltage amplitude of the power source, U_p - the voltage on the rectifier seen from terminals of the power source, U_c - the output voltage.
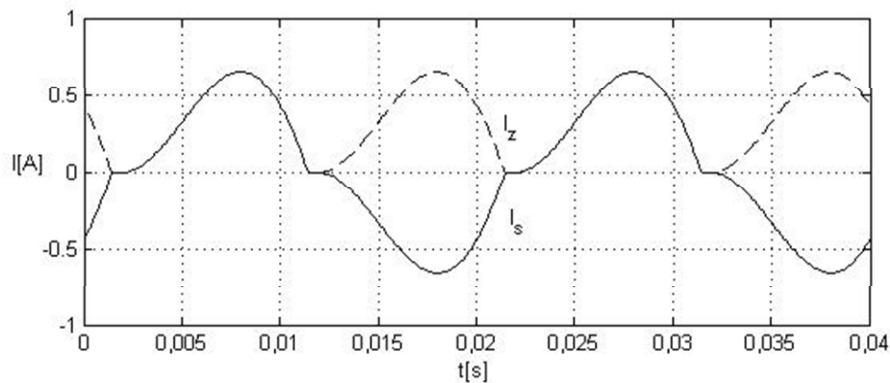

Fig. 7. The line currents I_s and I_z in circuit.

To check changes of the voltage and fluctuations of this voltage in some range of changes of parameters r_o and y performed the simulation experiment. The results of simulation present figures 8, 9 and 10.
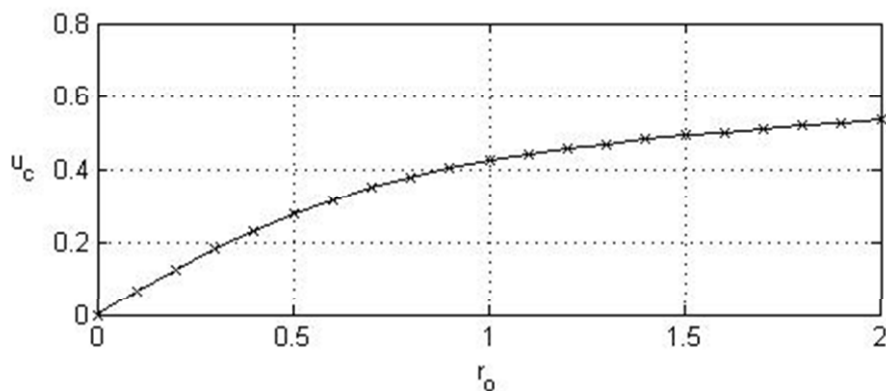

Fig. 8. The mean value of the dimensionless output voltage u_c in the function of the parameter r_o, for $y = 6.32$.

Figure 8 presents the dimensionless mean voltage u_c in the function of the parameter r_o for the constant value $y = 6.32$. With the characteristics results that for the increasing value of the parameter r_o the voltage u_c achieves more and more greater values. For the values of the parameter $r_o < 1$ the change u_c are characteristic for the continuous operation of the rectifier. For greater values of the parameter r_o ($r_o > 1$) the changes of the voltage u_c are somewhat slower, however the operation of the bridge rectifier adopts the interrupted mode. The figures 9 and 10 present the mean voltage u_c and amplitude of ripple u_t of this voltage in the function of the parameter y for the constant value $r_o = 0.5$. For the values of the parameter $y > 1$, the mean value of the voltage u_c and the amplitude of ripple u_t decrease. The amplitude of ripple u_t for $y = 1$ have value 30 % , however for greater values of the parameter y value u_t significantly decreases, for $y = 10$, the amplitude of these fluctuations amounts only approx. 4 %.
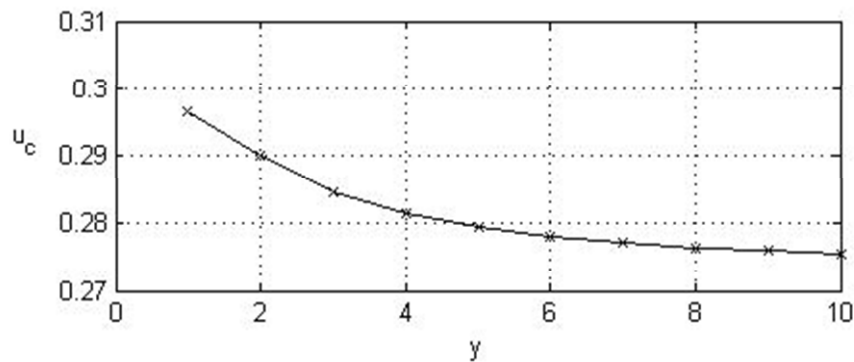

Fig. 9. The mean value of the dimensionless output voltage u_c in the function of the parameter y, for $r_o = 0.5$.
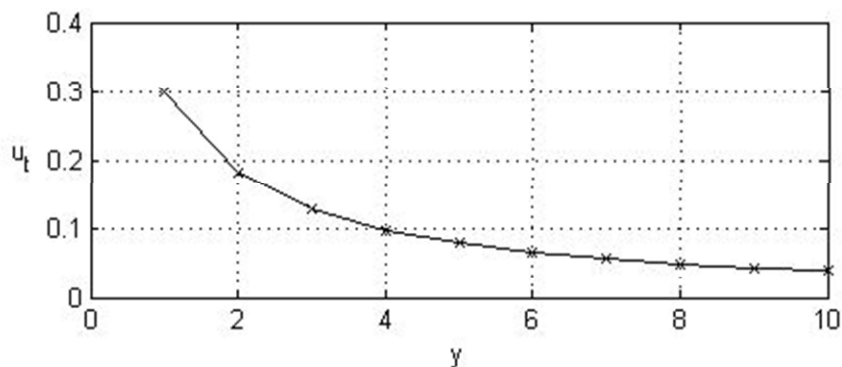

Fig. 10. The dimensionless amplitude of ripple u_t in the function of the parameter y, for $r_o = 0.5$.

Presented dependences were performed for example values of parameters r_o and y.

4. Conclusion

Presented model of the supply system has a small number of elements. It can constitute the good example of the non-linear load to research of influences of the non-linear load on mains and other loads attached to this mains. Proposed mathematical description of the circuit enables the analysis of continuous operation of the bridge rectifier and the definition of limiting conditions of such operation. For practical applications necessary are more exact analysis of the influence of individual parameters with to take into account of the dependence of output characteristics of the system from all dimensionless parameters.

References

[1] MOHAN, N., UNDELAND, T. M., ROBBINS, W. P.: *Power Electronics: Converters, Applications, and Design*, John Wiley & Sons, 2003

[2] KAŹMIERKOWSKI, M.P., MATYSIK, J. T.: *The introduction to the electronics and the power electronics, (in Polish), Wprowadzenie do elektroniki i energoelektroniki*, Oficyna Wydawnicza Politechniki Warszawskiej, Warszawa 2005

[3] WCIŚLIK, M.: *Powers Balances in AC Electric Circuit with Nonlinear Load, (in Polish), Bilanse mocy w obwodzie prądu przemiennego z odbiornikiem nieliniowym*, Przegląd Elektrotechniczny, 90(2014), nr 2,p. 5-8

[4] CARR, J. J.: *DC Power Supplies: A Technician's Guide, (in Polish), Zasilacze urządzeń elektronicznych: Przewodnik dla początkujących,* Wydawnictwo BTC, Warszawa 2004

Investigation of Peltier module based temperature difference sensor

*Grzegorz Witkowski, **Jakub Kulpa

*Kielce University of Technology, Faculty of Mechatronics and Machine Engineering , Department of Automatics and Robotics, Tysiąclecia Państwa Polskiego 7, 25-314 Kielce, Poland
** Kielce University of Technology, Faculty of Mechatronics and Machines Engineering , Department of Manufacturing Engineering and Metrology, Tysiąclecia Państwa Polskiego 7, 25-314 Kielce, Poland

Abstract. The paper discusses a possibility of applying the Peltier module as a temperature difference sensor. The assumption of investigation was thermoelectric effect especially Seebeck effect. Article explains the test method and shows the construction of research stand. Some of experimental results were shown.

1. Introduction

The thermoelectric effect is the straight transformation of temperature differences to electric voltage [1]. Thermoelectric devices create voltage at the terminals when there is a different temperature on each side. This effect can by successfully used to generate electricity or measure temperature. Because the direction of heating and cooling is determined by the polarity of applied voltage, thermoelectric devices can be used as temperatures controllers.

The Seebeck effect is a phenomenon in with a temperature difference between two dissimilar electrical conductors or semiconductors produces a voltage difference between the two substances[2]. If the two conductors or semiconductors are connected together through an electrical circuit, direct current flows through that circuit when the temperature difference is present. When heat is applied to one of the two conductors or semiconductors, heated electrons flow toward the cooler one.

The voltages produced by Seebeck effect are small, usually only a few microvolt per Kelvin of temperature difference at the junction. If the temperature difference is large enough, some Seebeck-effect devices can produce a few volts. Numerous such devices can be connected in series to increase the output voltage or in parallel to increase the maximum deliverable current [3]. Large arrays of Seebeck-effect devices can provide useful, small-scale electrical power if a large temperature difference is maintained across the junctions. The Seebeck effect is responsible for the behavior of thermocouples, which are used to approximately measure temperature differences or to actuate electronic switches that can turn large systems on and off. This capability is employed in thermoelectric cooling technology [4].

The aim of this study was to develop a Peltier module based temperature sensor and the identity of its Seebeck coefficient also known as thermopower or thermoelectric sensitivity.

2. Research stand

The test stand consist of the following elements:
- aluminum radiator,
- two thermocouples type K NiCr-NiAl,
- electrical equivalent load 40 W as a heat source unit,
- thermal insulation
- power supply KB-60-01
- Peltier module TEC1-12706

- National Instruments cDAQ 9172
- industrial PC host

The Peltier module is located between aluminum radiator and heat source to generate temperature difference on opposite sides. Heat source is insulated and powered by power supply.

On opposite sides of module are placed thermocouples to measure the temperature cycles on hot and cold sides during experiment. Thermocouples are connected to thermocouples module on cDAQ 9172. Terminals of Peltier module are connected to analog input of this device. Data acquisition device is connected to PC host with running LabView software. Research stand is illustrated on Fig. 1. Fig. 2 presents Peltier module situated on aluminum radiator.

Fig. 1. Research stand view

Fig. 2. Radiator with Peltier module

LabView software was used for data acquisition. The temperature measurements on both sides of the Peltier module were observed during the experiment. Simultaneously the voltage on the terminals of module was measured. All data have been stored on pc host with sampling frequency f=100 Hz. The code of developed application is presented on Fig. 3.
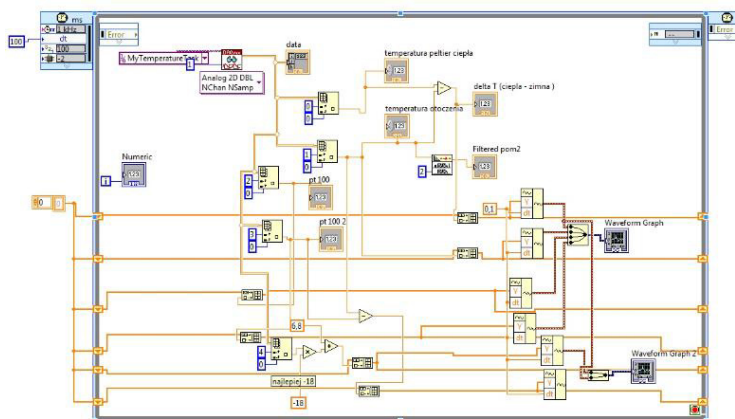
Fig. 3. Application code diagram

3. Results of experimental test

To obtain experimental data hot side of module was heated by the applied heat source. On opposite side heat was dissipated by the aluminum radiator. By subtracting measurements from thermocouples located on both sides of module the temperature difference has been determined. Simultaneously voltage on terminals of module was measured. Next stage of the investigation was to determine the relationship between designated temperature difference and measured voltage. Selected experimental results of the first experiment are shown on Tab. 1.

Time	thermocouples difference ΔT_t [°C]	Module voltage U [V]
0	3.6072	0.170784
1	3.51241	0.166851
2	3.43406	0.162262
3	3.34456	0.158328
4	3.26927	0.155378
5	3.20903	0.1521
6	3.14267	0.148822

Tab. 1. Measurements results of first experiment

After successful data acquisition the relation between variables has been estimated. The authors observed a close to linear relationship according to the formula described with equations:

$$U = \Delta T_t \cdot 0{,}0473 \tag{1}$$

$$\Delta T_p = \frac{U}{0{,}0473} \tag{2}$$

where:
- U [V] - Peltier module measured voltage
- ΔT_t [°C] - temperature difference based on thermocouples measurements
- ΔT_p [°C] - temperature difference determined using module voltage measurements
- $S = 0.0473$ [V/°C] - thermoelectric sensitivity

The graphical interpretation of variable relationship is shown on Fig. 4.
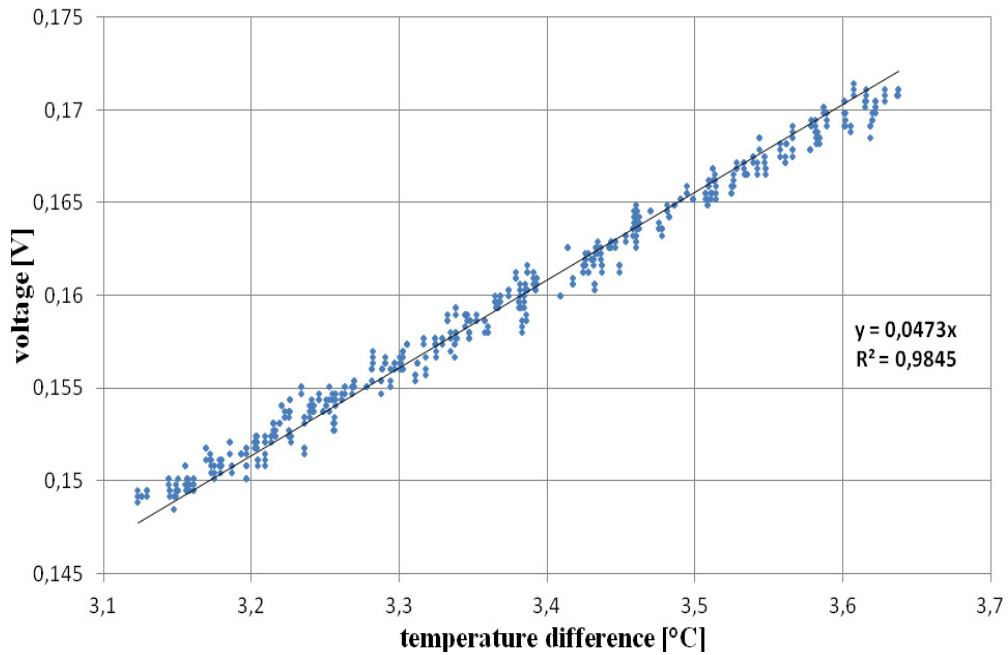
Fig. 4. Graphical interpretation of variables relationship

After determining the proportionality factor the course of the temperature difference basis of the indication of Peltier module has been determined. The course of temperature difference measured basis of thermocouples and Peltier module is shown on Fig. 5.
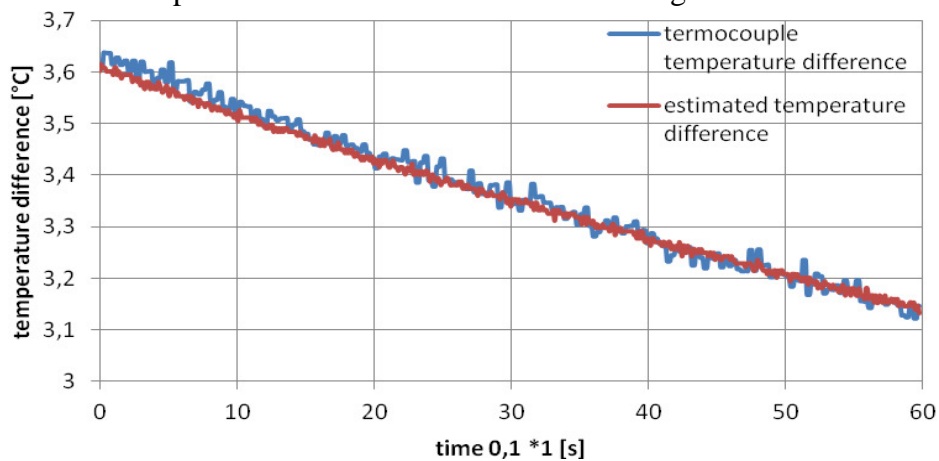

Fig. 5. Thermocouples and Peltier module measurements of temperature difference

The average difference between temperature measurements has been estimated using equation:

$$\bar{\delta} = \sum_{i-1}^{n} \frac{\Delta T_{pi} - \Delta T_{ti}}{n} = 0,00769 \qquad (3)$$

The changes of the difference between measurements versus time are illustrated on Fig. 6.
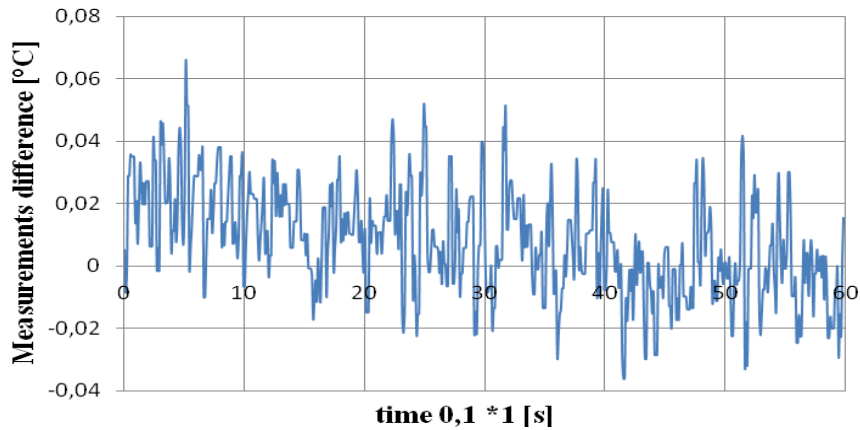
Fig. 6. The changes of the difference between measurements

Second experiment was conducted to verify determined relationship between module voltage and temperature difference. Experiment involves the formation of a temperature difference of 19.5 [℃] and increase its value to 22 [℃] and subsequently reduced to a value of 19.5 [℃]. Selected experimental results of the second experiment are shown on Tab. 2.

Time	thermocouples difference ΔT_t [℃]	Module voltage U [V]
0	19.5329	0.923906
1	20.5058	0.969924
2	21.4733	1.015687
3	21.7245	1.027569
4	20.9081	0.988953
5	20.387	0.964305
6	19.8511	0.938957
7	19.3913	0.917208

Tab. 2. Measurements results of second experiment

Based on the previously defined equation the temperature difference basis of the indication of Peltier module has been determined and compared with thermocouples measurements. The course of temperature difference measured basis of thermocouples and Peltier module is shown on Fig. 7.
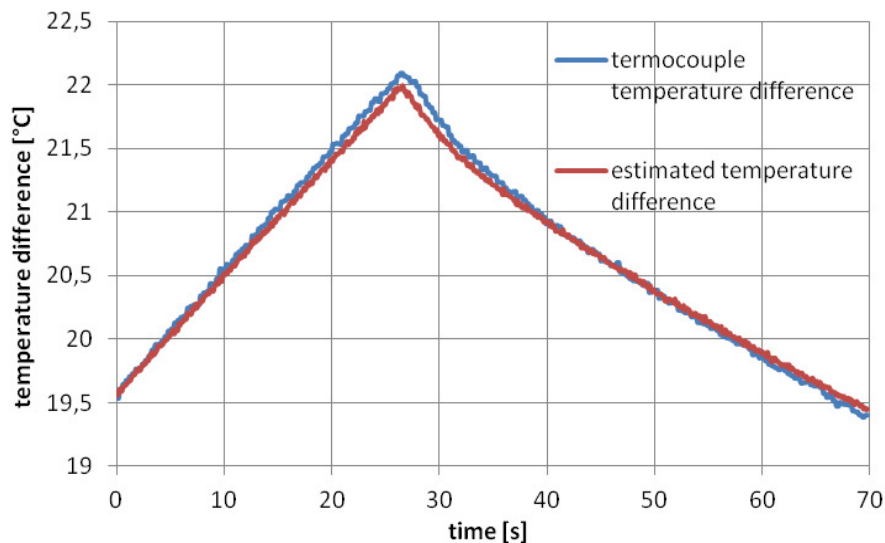
Fig. 7. Thermocouples and Peltier module measurements of temperature difference

The average difference between temperature measurements has been estimated using equation:

$$\overline{\delta} = \sum_{i-1}^{n} \frac{\Delta T_{pi} - \Delta T_{ti}}{n} = 0{,}02724 \qquad (4)$$

The changes of the difference between measurements versus time are illustrated on Fig. 8.
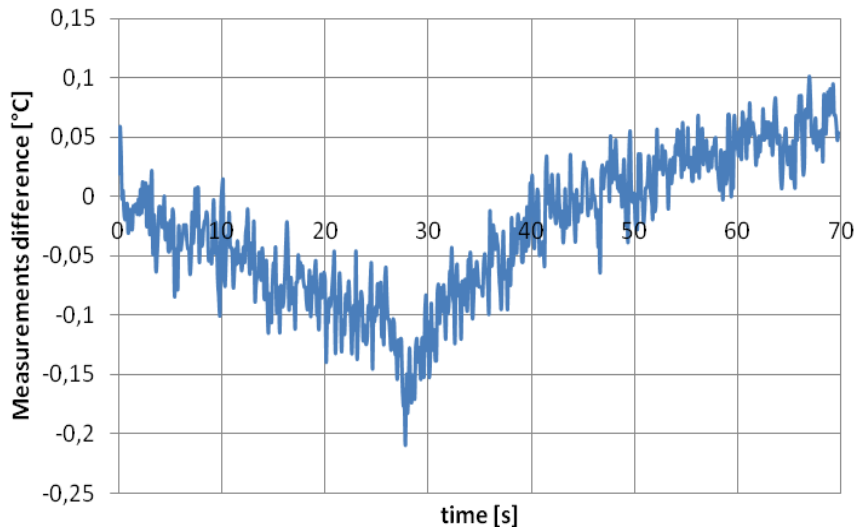

Fig. 8. The changes of the difference between measurements

4. Conclusion

The aim of study was to check usefulness Peltier module as a temperature difference sensor. During investigation two fundamental experiments were conducted. In the first one the relationship between module voltage and measured temperature difference has been determined. Also the thermoelectric sensitivity of module has been specified. Second experiment was conducted to confirm the determined relationship and specified coefficient. During experiments the changes of the difference between measurements and its average were calculated. The obtained results suggest the possibility of using Peltier module as a precise temperature difference sensor. Any errors that occurred may by the results of thermocouples inertia. To get precise data it is necessary to conduct series of measurements in thermal steady state to eliminate thermocouples inertia error.

References

[1] JOFFE A.. Termoelementy półprzewodnikowe. Warszawa 1957. Abram Fedorovich Ioffe. Semiconductor Thermoelements and Thermoelectric Cooling.

[2] Abram Fedorovich Ioffe. Semiconductor Thermoelements and Thermoelectric Cooling.

[3] CHIEN-Yi Du. CHANG-Da Wen. Experimental investigation and numerical analysis for one-stage thermoelectric cooler considering Thomson effect. International Journal of Heat and Mass Transfer. March 2011

[4] HUANNG M.. R. Yen. WANG A. The influence of the Thomson effect on the performance of a thermoelectric cooler. International Journal of Heat and Mass Transfer. 48 (2005)